

Mehmet Emre Börü

VIV Fatigue of Dynamic Power Cables Applied in Offshore Wind Turbines

Master's thesis in Marine Technology

Supervisor: Prof. Svein Sævik

Co-supervisor: Assoc. Prof. Yanlin Shao

June 2021



Norwegian University of
Science and Technology

Mehmet Emre Börü

VIV Fatigue of Dynamic Power Cables Applied in Offshore Wind Turbines

Master's thesis in Marine Technology
Supervisor: Prof. Svein Sævik
Co-supervisor: Assoc. Prof. Yanlin Shao
June 2021

Norwegian University of Science and Technology
Faculty of Engineering
Department of Marine Technology





MASTER THESIS SPRING 2021

for

Stud. Tech. Mehmet Emre Börü

VIV Fatigue of Dynamic Power Cables applied in Offshore Wind Turbines

Virvelindusert utmatting av dynamiske kraftkabler for Havvindturbiner

Dynamic power cables applied in Offshore Wind Turbines exposed to current and waves will experience high frequent lift forces from vortices shed at the wake of the cylinder which might cause Vortex Induced Vibration (VIV) leading to fatigue. For steel pipes this phenomenon is known to limit the fatigue life. However, for complex cross-sections such as power cables, the damping is much larger due to the friction between layers. Up to now, the engineering tools available to evaluate VIV fatigue require a linear structural model to be applied which causes difficulties with respect to documenting the fatigue life with respect to VIV for complex cross-sections. However, a newly developed VIV model enables time domain analysis to be carried out, thus allowing a non-linear structural model to be applied. In the present thesis, time domain analysis is to be carried out to investigate the effect of the real damping behaviour with respect to VIV. The thesis work is to be carried out as a continuation of the project conducted during Fall 2020 as follows:

1. A literature review into empirical VIV models, cable technology, local and global analysis of dynamic risers, relevant standards.
2. Define a case scenario of a marine riser power cable including global configuration, environmental conditions, cross-section properties and SN curves for tensile armour and copper conductor.
3. Establish material laws for axisymmetric and bending loads, including both hysteresis and elastic material models. This can be based on both analytical and numerical (Bflex cross-section modelling) procedures.
4. Establish the analytical and/or numerical transformation between load effect (tension & curvature) and stress in both the tensile armour and the copper conductor
5. Establish global riser models in Simla including both linear elastic and hysteresis based models.
6. Perform global analysis for the selected case scenario.
7. Perform stress and fatigue analysis to compare between global hysteresis and line elastic global models, also the significance of VIV versus 1st order wave effects.
8. Conclusions and recommendations for further work

The work scope may prove to be larger than initially anticipated. Subject to approval from the supervisors, topics may be deleted from the list above or reduced in extent.



In the thesis report, the candidate shall present her personal contribution to the resolution of problems within the scope of the thesis work

Theories and conclusions should be based on mathematical derivations and/or logic reasoning identifying the various steps in the deduction.

The candidate should utilise the existing possibilities for obtaining relevant literature.

Thesis report format

The thesis report should be organised in a rational manner to give a clear exposition of results, assessments, and conclusions. The text should be brief and to the point, with a clear language. Telegraphic language should be avoided.

The report shall contain the following elements: A text defining the scope, preface, list of contents, summary, main body of thesis, conclusions with recommendations for further work, list of symbols and acronyms, references and (optional) appendices. All figures, tables and equations shall be numerated.

The supervisors may require that the candidate, in an early stage of the work, presents a written plan for the completion of the work.

The original contribution of the candidate and material taken from other sources shall be clearly defined. Work from other sources shall be properly referenced using an acknowledged referencing system.

The report shall be submitted in electronic format (.pdf):

- Signed by the candidate
- The text defining the scope shall be included (this document)
- Drawings and/or computer models that are not suited to be part of the report in terms of appendices shall be provided on separate (.zip) files.

Ownership

NTNU has according to the present rules the ownership of the thesis reports. Any use of the report has to be approved by NTNU (or external partner when this applies). The department has the right to use the report as if the work was carried out by a NTNU employee, if nothing else has been agreed in advance.

Thesis supervisors:

Prof. Svein Sævik, NTNU

Ass. Prof. Yanlin Shao, DTU

Deadline: 25th June, 2021

Trondheim, January 18th, 2021

Svein Sævik

Abstract

In this work, the effect of vortex-induced vibrations (VIV) on the fatigue strength of subsea power cables were investigated by the implementation of a non-linear time domain analysis methodology. To have a better understanding of VIV, experiments and empirical models for VIV were explained. Besides, several examples for frequency and time domain VIV models were given. Furthermore, relevant standards for the fatigue design of subsea dynamic power cables were addressed.

A linear global finite element model of the power cable in SIMLA software to establish tension and curvature time histories and the local model of the cable cross-section in BFLEX software to obtain axial stress signals for various points in the cable were created. Case scenario was analysed by considering both the hogging and the sagging sections for 4 different conditions and 7 different loading cases for each conditions. First condition considers VIV and all environmental loads. Second exclude VIV but keeping other parameters the same. For the third condition, wave loads are not taken into account by a filtering process of tension and curvature time histories obtained by the global analysis. For the last condition, frictions between cable layers in the axial direction are deactivated in the local model.

Time series by global analyses are post-processed to be used in local analyses as input. Local analyses gave axial stress signals for the internal steel armor layer in three different points. Two of these points are selected to give the fatigue damage for maximum cross-flow and in-line responses. The other one is neutral for both in-line and cross-flow vibrations. In-plane and out-of-plane bending moments and the axial force for centre body of the cable cross-section which includes copper conductors were computed. By using these time series axial stresses in the centre body were calculated analytically for 3 different points based on the same concept applied for the steel armor layer. Having evaluated stress signals, Rainflow algorithm was used to separate them into stress ranges and corresponding cycles. Then, Miner's Sum was introduced to calculate accumulated fatigue damage for each location in each condition.

Analyses have shown that the internal steel armor is the governing layer for the fatigue life.

Especially, the fatigue damage in the CF direction appeared to be the maximum due to large out-of-plane curvatures. The fatigue life is the lowest also in the CF direction for the centre body. However, fatigue lives for the centre body are much larger compared to ones for the internal steel armor. That is because external loads are taken by the internal armor layer.

In addition, environmental loads, especially wave loads, appeared to be an important aspect for the fatigue design of such structures, especially with respect to the increased drag forces. Thus, environmental conditions of the operational area should be taken into account during the design process.

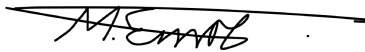
Lastly, frictions between the contact surfaces take an important part of the fatigue damage. Special anti-corrosive actions might be taken to reduce the fatigue damage accumulation due to the friction.

Preface

This report is written during spring semester 2021 as a Master's thesis for Nordic Master in Maritime Engineering study program with Ocean Structures study track. This work is the extension of my project report which I have prepared for Marine Structures Specialization Project (TMR 4500).

I would like to thank to my supervisors Professor Svein Sævik from NTNU and Associate Professor Yanlin Shao from DTU for the time they have spent to help and support me. I am really grateful for their guidance during the preparation of this thesis.

Trondheim, June 2021



Mehmet Emre BÖRÜ

Nomenclature

List of Symbols

B	Buoyancy
C_e	Excitation force coefficient
C_a	Added mass coefficient
C_D	Drag coefficient
E	Elastic modulus
EA	Axial stiffness
EI	Bending stiffness
f_0	Eigenfrequency
f_{osc}	Oscillation frequency
f_v	Vortex shedding frequency
\hat{f}	Dimensionless response frequency
\hat{f}_e	Dimensionless excitation frequency
GI_t	Torsion stiffness
H_s	Significant wave height
k	Weibull shape parameter
M_t	Torsion moment
M_y	In-plane bending moment
M_z	Out-of-plane bending moment
T	Tension
T_p	Wave peak period
α	Lay angle for steel armour wires

ϵ	Strain
σ	Stress
λ	Weibull scale parameter
κ_y	In-plane curvature
κ_y	Out-of-plane curvature
ϕ_e	Instantaneous phase of the excitation force
ϕ_r	Instantaneous phase of the cylinder velocity
γ_f	Load factor
γ_m	Material factor
γ	Safety factor

List of Abbreviations

<i>API</i>	American Petroleum Institute
<i>ASD</i>	Allowable Stress Design
<i>CF</i>	Cross-flow
<i>DNV</i>	Det Norske Veritas
<i>FEM</i>	Finite Element Method
<i>IL</i>	In-line
<i>LRFD</i>	Load and Resistance Factor Design
<i>OWT</i>	Offshore Wind Turbine
<i>PSD</i>	Power Spectral Density
<i>Re</i>	Reynolds Number
<i>St</i>	Strouhal Number
<i>VIV</i>	Vortex-Induced Vibrations

Contents

1	INTRODUCTION	1
1.1	Background	1
2	INTRODUCTION TO VIV	3
2.1	Experiments and Empirical Models	3
2.1.1	Fixed Cylinder Test	3
2.1.2	Free Oscillation Test	6
2.1.3	Forced Harmonic Oscillations	9
3	Frequency Domain VIV Models	12
3.1	VIVANA Model	12
3.1.1	Model For Added Mass Coefficient	13
3.1.2	Model For Excitation Force	14
3.1.3	Excitation zones	15
3.1.4	Computing the response	17
3.2	SHEAR 7 Model	18
3.2.1	Solution by Mode Superposition	19
4	Time Domain VIV Model	24
4.1	Hydrodynamic Force Models in CF and IL Directions	24
4.2	Synchronization in IL and CF Directions	25
4.3	Solving Dynamic Equilibrium Equation in Time Domain	29
5	CABLE TECHNOLOGY	30

5.1	General Design Concepts of Subsea Dynamic Power Cables	30
5.1.1	Relevant Loads for design	31
5.1.2	Failure Modes	34
5.2	Fatigue of Dynamic Power Cables	35
5.2.1	Mean Stress Correction	37
5.2.2	Analytical Model to calculate stresses	39
5.3	Rainflow Counting For Cumulative Damage Analysis	40
5.4	Response Analysis of Dynamic Power Cables	42
6	CASE SCENARIO	44
6.1	Mechanical Properties	45
6.1.1	Power Cable Cross Section	45
6.1.2	Buoyancy Elements	47
6.2	Environmental Data	48
6.2.1	Wind Climate	48
6.2.2	Wave Climate	50
6.2.3	Current	51
6.3	Floater Motions	54
6.4	Fatigue Data	54
7	MODELLING PROCEDURE	56
7.1	Local Model	56
7.1.1	Cable Cross Section	56
7.1.2	Element Properties for FE Model in BFLEX	56
7.1.3	Applying Periodicity Conditions for FE Model in BFLEX	62
7.1.4	Extracting Material Properties From The Local Model	63
7.2	Global Model	66
7.2.1	Cable Configuration	66
7.2.2	Boundary Conditions	68
7.2.3	Validation of The Global Model	68
7.2.4	Pipe Elements	69

7.2.5	Global Load Model in SIMLA	70
8	ANALYSIS METHODOLOGY	72
8.1	Global Analysis	73
8.1.1	Post-Processing	73
8.2	Local Analysis	74
8.3	Fatigue Analysis	76
9	RESULTS & DISCUSSION	78
9.1	Global Analysis Results	78
9.2	Local Analysis Results	86
9.3	Fatigue Analysis Results	90
10	CONCLUSION & FURTHER WORK	93
10.1	Conclusion and Summary	93
10.2	Recommendations for Further Work	94
	References	95
A	Floater Motions	98
B	Global Analysis Results in Frequency Domain	102

List of Tables

6.1.1 Material Properties of Cable Components (Leroy et al., 2017)	46
6.1.2 Buoyancy Elements' Characteristics	47
6.2.1 Wind Speed Profile for Operational Conditions (Lifes50+, 2015)	49
6.2.2 Wind Speed Profile for Extreme Conditions (Lifes50+, 2015)	49
6.2.3 Sea State (Lifes50+, 2015)	50
6.2.4 Current profile for 1 year of return period (Lifes50+, 2015)	52
6.2.5 Parameters for Weibull's Distribution	53
6.2.6 Current Profiles for each cases	54
7.1.1 Force, moment and strain values for local analysis	64
7.1.2 Material Properties to be used in the Global Analysis	66
7.2.1 Power Cable Parameters for global model	67
7.2.2 Comparison of maximum curvature and tension values with the limit values . . .	68
8.2.1 Material properties of the center body	76
9.3.1 Fatigue life results in years for the centre body	91
9.3.2 Fatigue life results in years for the internal steel armor layer	91

List of Figures

2.1.1 Flow variation around the cylinder for different Re (Mathisen, 1992)	4
2.1.2 Effect of surface roughnes on Strouhal Number (Achenbach & Heinecke, 1981)	6
2.1.3 Free Oscillation Test Configuration (Larsen, 2020)	7
2.1.4 Added Mass Variation as a function of Reduced Velocity (Vikestad et al., 2000)	8
2.1.5 Frequency Ratio as a function of Reduced Velocity (Vikestad et al., 2000)	9
2.1.6 Added Mass Coefficient as a function of non-dimensional amplitude and frequency (Gopalkrishnan, 1993)	10
2.1.7 Excitation Force Coefficient as a function of non-dimensional amplitude and frequency (Gopalkrishnan, 1993)	11
3.1.1 Added mass variation as a function of non-dimensional frequency (Passano et al., 2014)	13
3.1.2 IL Excitation force coefficient as a function of A/D (Larsen et al., 2008)	14
3.1.3 CF Excitation force coefficient as a function of A/D (Larsen et al., 2008)	15
3.1.4 Excitation zones by time sharing method (Passano et al., 2014)	16
3.1.5 Excitation zones by space sharing method (Passano et al., 2014)	17
3.2.1 Evaluation of excited modes (Vandiver & Li, 2005)	19
3.2.2 Modes of interest by power-in ratio (Vandiver & Li, 2005)	20
3.2.3 Division of power-in regions (Vandiver & Li, 2005)	21
4.1.1 Local coordinate system and velocity components for a slender marine structure proposed by (Ulveseter et al., 2018)	25
4.2.1 Excitation force coefficients in IL direction (Aronsen, 2007)	26
4.2.2 Phase of portrait method for CF direction (Thorsen et al., 2014)	27

4.2.3 Time crossings for equation 4.2.4 (Ulveseter et al., 2017)	28
5.1.1 A typical subsea power cable cross section (DNV, 2016)	30
5.1.2 Single and three phase AC voltages (Patrick et al., 1999)	31
5.1.3 Probability Density Functions for Characteristic Load and Structural Resistance (Sævik, 2019a)	33
5.2.1 Dynamic power cable connected to the floating OWT, (Nasution et al., 2014) . .	36
5.2.2 Cross section of dynamic power cable with dynamic torque moment ΔM_x , dy- namic bending moments ΔM_z and ΔM_y , mean axial force \bar{F}_x , dynamic axial force ΔF_x and friction coefficient μ , (Nasution et al., 2014)	37
5.2.3 Haigh Diagram with Goodman and Gerber assumptions (Sævik, 2019a)	38
5.3.1 (a) Strain History and (b) corresponding stress-strain response (As & Berge, 2017)	40
5.3.2 Illustration of Pagoda Roof Rainflow Analogy (As & Berge, 2017)	41
5.4.1 Relation between moment and curvature for a dynamic power cable (Sævik, 2019a)	42
6.0.1 Lazy-wave configuration of the power cable	45
6.1.1 Power Cable Cross Section	46
6.2.1 West of Barra Site Location (Lifes50+, 2015)	48
6.2.2 JONSWAP Spectrum of the sea state	51
6.2.3 Probability densities and occurrence probabilities for current speeds	53
6.4.1 S-N curves to be used in the fatigue calculations (Nasution et al., 2014)	55
7.1.1 Organisation of Local Model in Bflex	57
7.1.2 Representation of Hshear353 Dofs (Sævik, 2019b)	58
7.1.3 Representation of Hshear353 dofs (Sævik, 2019b)	60
7.1.4 Representation of 13 Dofs HCONT463 Contact Element (Sævik, 2019b)	61
7.1.5 Nodes for periodicity conditions (Leroy et al., 2017)	62
7.1.6 Local Model in Bflex	64
7.1.7 Variations of tension and torsion moment in the armour layer as a function of strain	65
7.1.8 Variation of bending moment in the armour layer as a function of strain	65
7.2.1 Parts of the Global Model	67

7.2.2 Ghost reference formulation by Mathisen(1990) for motion of the nodes (Sævik, 2017) 70

8.0.1 Analysis methodology to estimate the fatigue life 72

8.2.1 Integration points to extract stress signals in the steel internal armour layer . . . 75

8.3.1 Turning points of copper conductor’s stress signal for Case 7 in Hogging Section ($\theta = 0$) 76

9.1.1 Global Analysis Results for Case 1 Sagging Section 78

9.1.2 Global Analysis Results for Case 2 Sagging Section 79

9.1.3 Global Analysis Results for Case 3 Sagging Section 79

9.1.4 Global Analysis Results for Case 4 Sagging Section 80

9.1.5 Global Analysis Results for Case 5 Sagging Section 80

9.1.6 Global Analysis Results for Case 6 Sagging Section 81

9.1.7 Global Analysis Results for Case 7 Sagging Section 81

9.1.8 Global Analysis Results for Case 1 Hogging Section 82

9.1.9 Global Analysis Results for Case 2 Hogging Section 82

9.1.10 Global Analysis Results for Case 3 Hogging Section 83

9.1.11 Global Analysis Results for Case 4 Hogging Section 83

9.1.12 Global Analysis Results for Case 5 Hogging Section 84

9.1.13 Global Analysis Results for Case 6 Hogging Section 84

9.1.14 Global Analysis Results for Case 7 Hogging Section 85

9.2.1 Stress signals for the hogging section for the most extreme loading case in the presence of both wave loads and VIV 86

9.2.2 Stress signals for the hogging section for the most extreme loading case without VIV 87

9.2.3 Stress signals for the hogging section for the most extreme loading case without wave kinematics 87

9.2.4 Stress signals for the hogging section for the most extreme loading case without the friction between the contact surfaces 88

9.2.5 Stress signals for the sagging section for the most extreme loading case in the presence of both wave loads and VIV 88

9.2.6 Stress signals for the sagging section for the most extreme loading case without VIV	89
9.2.7 Stress signals for the sagging section for the most extreme loading case without wave kinematics	89
9.2.8 Stress signals for the sagging section for the most extreme loading case without the friction between the contact surfaces	90

Chapter 1

INTRODUCTION

1.1 Background

Renewables seem to be the most promising option for the world's energy needs in the near future. Offshore wind is one of them that stands out. With the increasing demand on offshore wind, shallow-water locations are preferred to build offshore wind farms. However, expanding volume of the OW industry will require floating offshore wind turbines which could operate in the deep waters. That is why design of the dynamic power cables is a crucial issue for these structures due to severe environmental conditions.

Furthermore, one of the most important design problem that these dynamic power cables face is fatigue due to Vortex Induced Vibration(VIV). As water depth increases, larger wave loads take place and lead to massive current loads. Flow separations prior to vortex shedding occur because of the interaction between these loads and cylinder structures such as the power cables. In addition, vortex shedding creates the VIV and may cause significant lift forces and further cyclic bending stresses on the structure.

Moreover, VIV are one of the most important problem in the design process because it may lead the fatigue of the structure. Unfortunately, there are lots of ambiguities about how to predict dynamic response of the structure under the effect of VIV. The reason for that is marine risers, cables and pipelines are highly non-linear structures. On the contrary, most of the softwares used in the industry (VIVANA, SHEAR7) are based on linear analysis. In other words frequency domain is assumed in the design process. Subsequently, structural models need to be linearized for this kind of analysis and this is not a reliable method to estimate dynamic behavior of such non-linear structures.

In the light of the information above, a time domain analysis is required to include all the

non-linearities of the structure. For instance, escalating drag forces due to vibrations generate tensile forces along the cable. Besides, with the continuously varying vibration frequency, tensile forces also change quickly. Meanwhile, location where the cable connects to seabed is of interest to impose time-varying boundary conditions for taking into account non-linear soil parameters. Another advantage of the time domain analysis is that unlike frequency domain analysis, response by each different frequency does not have to be analyzed one by one. The effect of these frequencies on each other can be estimated in a time domain analysis.

Objectives

The main goal of this thesis work is to give general understanding of VIVs and to explain their effect on fatigue accumulation on the dynamic power cables. A time domain analysis will be implemented in order to establish the contribution of non-linearities to the dynamic behavior of the structure. Further details about the objectives of this thesis is listed as follows:

- Introducing some example models for both frequency and time domain VIV. In addition to this, general information about the hydrodynamics of cylinder structures will be given.
- Evaluating general design concepts of subsea dynamic power cables by taking into account the fatigue damages due to large environmental loads
- A case scenario will be defined based on mechanical properties of the cable structure and the environmental data
- The SIMLA software will be used to create global non-linear structural model. Local model will be practiced by Bflex.
- Both global and local analysis will be performed for investigating the dynamic behavior of the structure.
- Conclusions and recommendations will be given for further work.

Chapter 2

INTRODUCTION TO VIV

One of the most important parameter in the design process of marine dynamic power cables is VIV. When the structure encounters a current as a result of this vortices are formed. Forces developed by these vortices produce VIV. This phenomenon may lead to fatigue and amplified drag forces in in-line(IL) direction which is parallel to the flow direction. In addition, if oscillations occur orthogonal to the current, that means this is a cross-flow situation.

2.1 Experiments and Empirical Models

Empirical models are based on a variety of different tests and experiments. The aim is to obtain information about the added mass and the force coefficients for building an empirical model.

2.1.1 Fixed Cylinder Test

The fixed cylinder test is a convenient way to investigate hydrodynamic properties of the structures with circular cross sections. This experiment is highly dependent on the Reynolds number(Re). Also, it is essential to mention about Strouhal number(St) which varies with the Reynolds number. Following equations are used for calculating these hydrodynamic terms:

$$Re = \frac{UD}{\nu} \quad (2.1.1)$$

$$St = \frac{f_v D}{U} \quad (2.1.2)$$

Where, U , D , ν and f_v are the flow velocity, cylinder diameter, kinematic viscosity of the fluid

and the vortex shedding frequency, respectively. Different Reynolds numbers are applied to visualize their effect on the vortex pattern. Below Figure 2.1.1 illustrates those patterns.

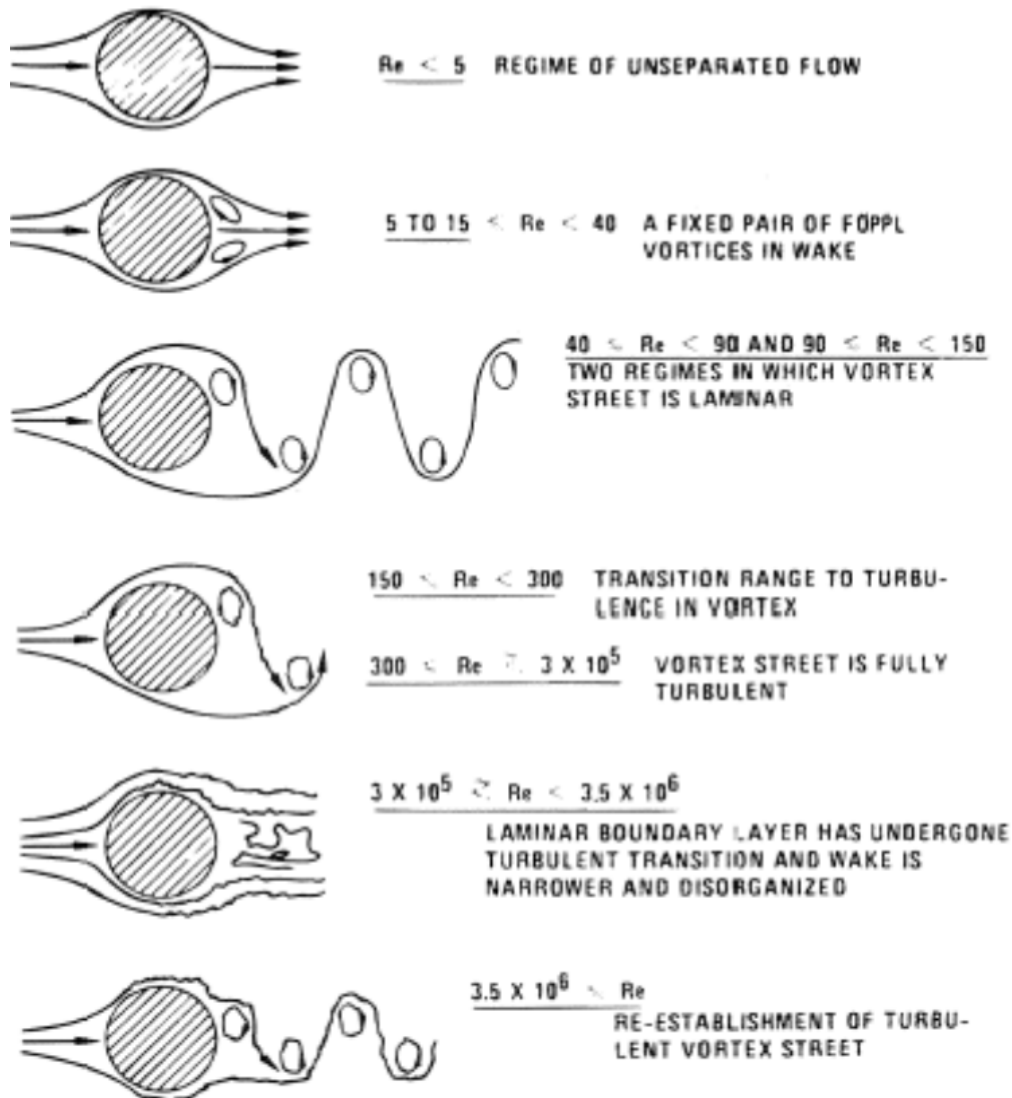


Figure 2.1.1: Flow variation around the cylinder for different Re (Mathisen, 1992)

Above stages can be described step by step as follows:

- $Re < 5$: Viscous effects dominate. Flow follows the cylinder surface, in other words there is no flow separation
- $5 \leq Re < 40$: The flow starts to separate. Formation of vortices is seen behind the cylinder.

- $40 < \mathbf{Re} < 150$: When $\text{Re} \simeq 40$ a larger vortex is produced due to an instability. This larger vortex splits from the boundary layer and is drifted by the flow. In this case flow is laminar.
- $150 < \mathbf{Re} < 300$: By the increasing Re flow transition from laminar to turbulence regime occurs.
- $300 < \mathbf{Re} < 3 \times 10^5$: By $\text{Re}=300$ wake behind the cylinder become three dimensional and fully turbulent.
- $3 \times 10^5 < \mathbf{Re} < 3 \times 10^6$: This interval of Re number is known as "*subcritical regime*" where a laminar boundary layer around the cylinder is observed. However, as Re continues to increase, a turbulent boundary layer should be expected.
- $3 \times 10^6 < \mathbf{Re}$: Regime corresponding to this range of Re is called "*critical regime*". Boundary layer is turbulent at one side of the cylinder. Existence of a laminar flow at the other side leads to an anti-symmetry and a lift force.

For most of the cases listed above, the Strouhal number is constant. Usually, $\text{St} \simeq 0.2$ for most of the cases of interest. On the other hand, Achenbach and Heinecke (1981) state that surface roughness of the cylinder has a significant impact on St . For instance, turbulence regime appears at lower Reynolds numbers when surface is not smooth. Surface roughness is defined as the ratio of the average surface roughness height to the cylinder diameter (k/D). As it can be seen in below Figure 2.1.2, $\text{St} \simeq 0.2$ is valid for subcritical regime. However, St goes up during the transition to critical regime. It decreases around the same level as before when passing from critical regime to super-critical regime. It should be noticed that for large roughness this feature of St is not the case.

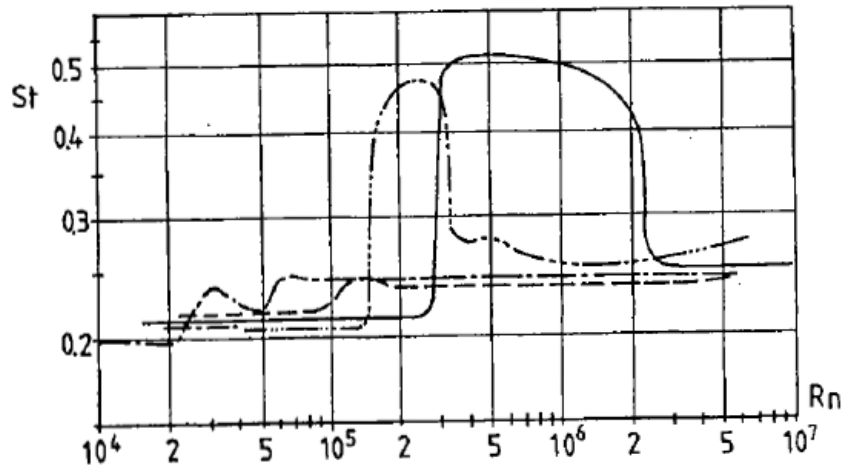


Fig. 6.26. Strouhal number St of rough circular cylinders in steady incident flow for different surface roughness values k/D (k = average height of surface roughness, D = cylinder diameter, $St = f_v D / U_\infty$, f_v = vortex shedding frequency, U_∞ incident flow velocity, $Rn = U_\infty D / \nu$.) —, smooth; — · · · —, $k/D = 7.5 \cdot 10^{-4}$; — — —, $k/D = 3 \cdot 10^{-3}$; — · —, $k/D = 9 \cdot 10^{-3}$; — — — —, $k/D = 3 \cdot 10^{-2}$. (Achenbach & Heinecke, 1981.)

Figure 2.1.2: Effect of surface roughness on Strouhal Number (Achenbach & Heinecke, 1981)

Furthermore, when cylinder encounters the current, pressure differences and shear forces develop on the surface. These result in fluid force which has two components; drag(in-line) force, lift(cross-flow) force. Non-dimensional drag and lift coefficients are used to express these forces:

$$C_{D,L} = \frac{F_{D,L}}{\frac{1}{2}\rho DU^2} \quad (2.1.3)$$

Where, ρ is the fluid density and $F_{D,L}$ is the fluid force component in cross-flow direction for lift force and in-line direction for drag force. Low fluid pressure in the wake region causes a non-zero mean drag. Meanwhile, lift forces has no mean value except when $Re > 3 \times 10^6$.

2.1.2 Free Oscillation Test

The free oscillation test is realised by implementing a 2-D model with a spring-cylinder system in steady flow, see Figure 2.1.3. To get familiarize with this problem is essential to understand more complex ones.

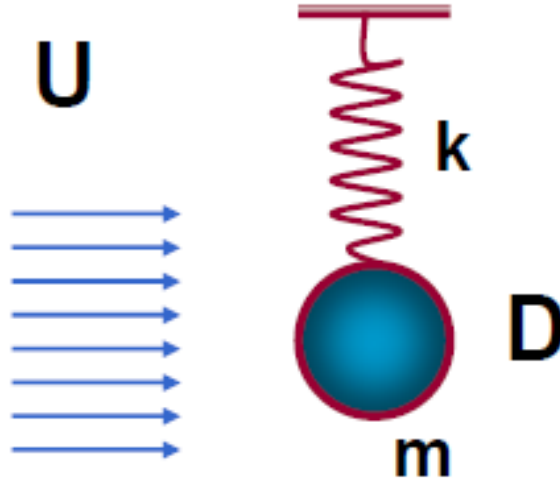


Figure 2.1.3: Free Oscillation Test Configuration (Larsen, 2020)

Where, k is the spring constant, while m stands for cylinder mass. The other two parameters are described in Section 2.1.1. There are three different frequency present in this case which are vortex shedding frequency f_v , eigenfrequency f_0 and lastly oscillation frequency f_{osc} . Also, three other key parameters related to these frequencies need to be defined. Since, the relation between St and the vortex shedding frequency is already elaborated, it is only required to introduce parameters linked to f_0 and f_{osc} .

$$U_R = \frac{U}{Df_0} \quad (2.1.4)$$

$$\hat{f} = \frac{f_{osc}D}{U} \quad (2.1.5)$$

U_R and \bar{f} are the reduced velocity and dimensionless response frequency. Speaking of reduced velocity, an important phenomenon called lock-in should be explained. That is a condition where f_v converges f_0 by variations in added mass under a constant value of St . Fluid forces acting on the cylinder increase dramatically during lock-in. On the other hand, the response frequency becomes a compromise value between f_0 (still water) and f_v (fixed cylinder) (Larsen et al., 2002).

The lock-in range for a cylinder depends on the capability of it adjusting its natural frequency according to varying added mass (Larsen et al., 2002). The dry mass is also an important

parameter for the lock-in range. As the weight of the cylinder increases, the lock-in range becomes narrower due to the insignificance of added mass change on the eigenfrequency f_0 . Larsen et al. (2002) conducted a cross-flow free oscillation experiment with three different support amplitudes. A cylinder with low mass ratio ($m/\rho D^2$) is used causing a wide lock-in range as it can be seen in Figure 2.1.4 and 2.1.5. The horizontal line in Figure 2.1.5 can be observed in order to evaluate lock-in range. It is obtained by the ratio of the mean oscillation frequency to the true natural frequency which is calculated by inserting added mass coefficients from Figure 2.1.4 into following equation:

$$f_n(U_r) = \frac{1}{2\pi} \sqrt{\frac{k_{tot}}{m + \rho V_{cyl} C_a(U_r)}} \quad (2.1.6)$$

Where, k_{tot} , V_{cyl} and m are total stiffness, volume of the cylinder and dry mass, respectively. Frequency ratio becomes equal to 1 at $U_r \simeq 3$ and it starts to deviate from 1 when $U_r \simeq 12$. Hence, the lock-in range is obtained as from $3 \geq U_r \geq 12$. Moreover, sloped curve represents the frequency ratio by using still water natural frequency f_0 . Meanwhile ratio of $\frac{f_{osc}}{f_0}$ rises, added mass follows a decreasing pattern over the lock-in range.

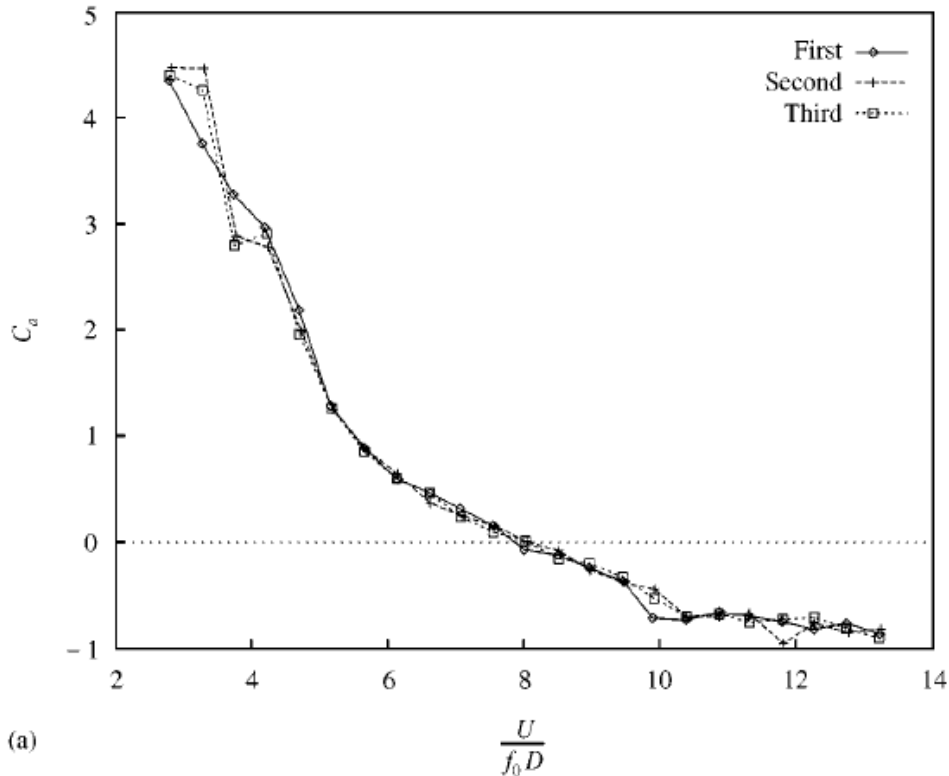


Figure 2.1.4: Added Mass Variation as a function of Reduced Velocity (Vikestad et al., 2000)

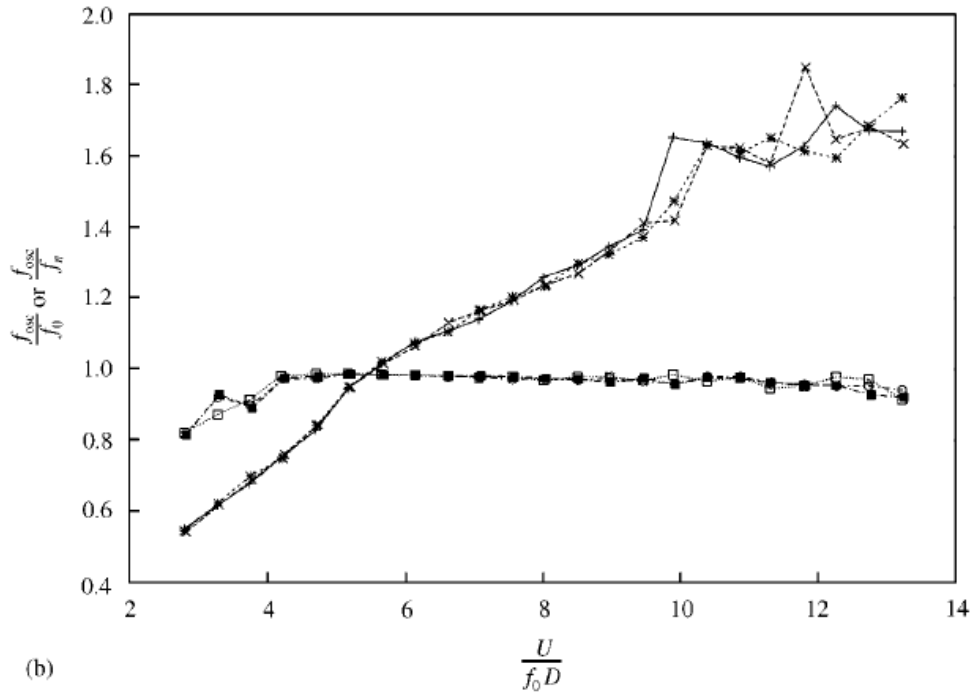


Figure 2.1.5: Frequency Ratio as a function of Reduced Velocity (Vikestad et al., 2000)

2.1.3 Forced Harmonic Oscillations

Unlike in the free oscillation case, cylinder oscillates with a given frequency and amplitude. In other words, motion is predefined. The combination of two parameters defines the motion; non-dimensional frequency (Equation.2.1.5) and amplitude (A/D). The aim for conducting such test is to evaluate excitation force coefficient (C_e) and added mass coefficients (C_a). While C_a will represent the force components which are out of phase with the cylinder velocity, in phase forces with the cylinder velocity will define C_e . In order to explain phase differences, dynamic equilibrium should be emphasized:

$$M(-\omega^2 A \sin \omega t) + C(\omega A \cos \omega t) + K(A \sin \omega t) = F_h \sin(\omega t + \epsilon) \quad (2.1.7)$$

In the above equation, M is dry mass of the cylinder, A is the motion amplitude, meanwhile C and K stand for damping and stiffness coefficients. However, C and K must be zero in the forced oscillation case. Moreover, it can be seen that hydrodynamic force F_h is out of the phase with acceleration of the cylinder. Below a more convenient way to represent this phase shift for measuring the driving force F_d is introduced:

$$(M + M_A)[- \omega^2 A \sin \omega t] + F_e \cos \omega t = F_d \tag{2.1.8}$$

That way hydrodynamic force F_h is separated into two component. These components are basically added mass (M_A) and excitation or damping force F_e depending on the sign of the cos function. Since term with F_e describes energy transfer between the fluid and the cylinder, plus sign indicates energy input to cylinder from the fluid. Otherwise in case of a minus sign, it means cylinder loses energy in other words damping occurs. On the other hand, added mass term is in phase with the acceleration and excitation force or damping is in phase with the velocity. Below contour plots by Gopalkrishnan (1993) are illustrating the variation of C_a and C_e as a function of non-dimensional frequency and response amplitude.

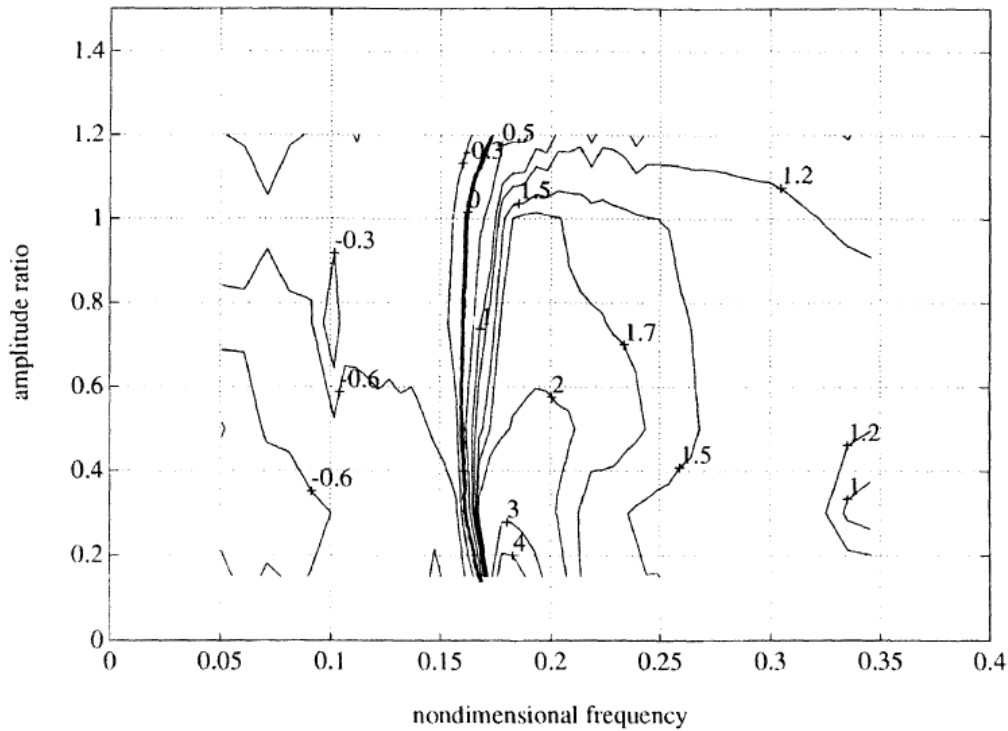


Figure 2.1.6: Added Mass Coefficient as a function of non-dimensional amplitude and frequency (Gopalkrishnan, 1993)

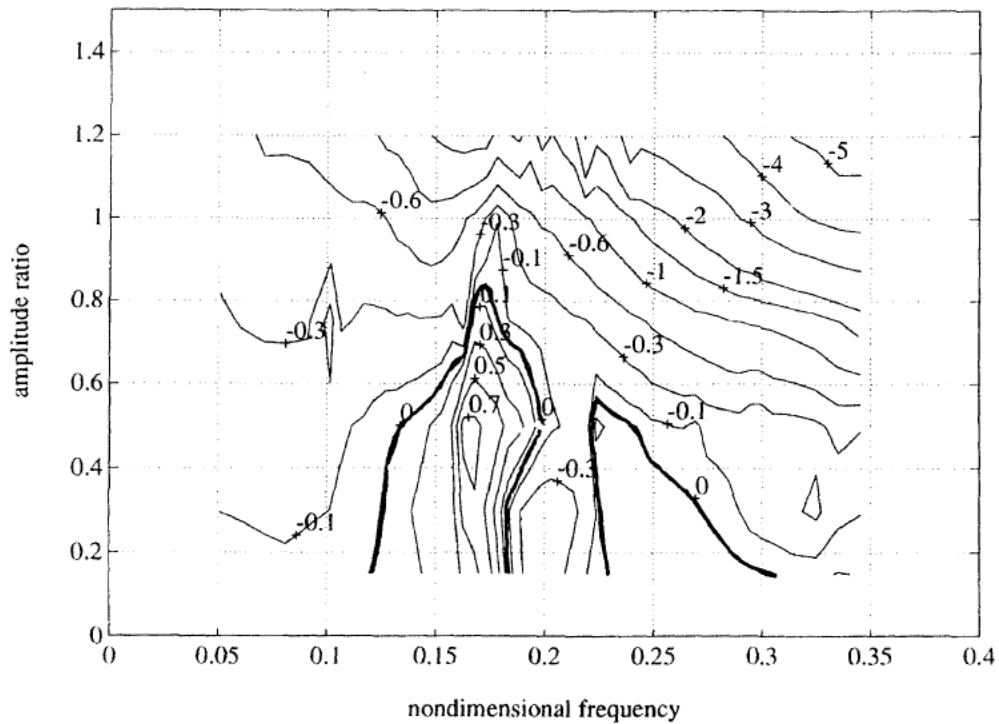


Figure 2.1.7: Excitation Force Coefficient as a function of non-dimensional amplitude and frequency (Gopalkrishnan, 1993)

These plots are very useful for the prediction of VIV along a length of a marine riser if the information of response frequency and amplitude is given. Also ideal lock-in situation can be observed by the help of this contours. It is the case when excitation coefficient is zero, in other words there is no energy exchange between the cylinder and the fluid.

Chapter 3

Frequency Domain VIV Models

3.1 VIVANA Model

VIVANA is a software which is widely used in the industry to investigate dynamic response of the slender structures under the effect of VIV. It operates in frequency domain and solves dynamic equilibrium equations by iterations. Since analysis is performed in frequency domain, a linear finite element model of the structure has to be implemented. Moreover, VIVANA gives three options of analysis namely; CF response, pure IL response or combined CF-IL response. The general procedure followed by VIVANA is listed below :

1. *Static Analysis*: First, static configuration of the structure is to be implemented according to FEM which is created via RIFLEX.
2. *Eigenvalue Analysis*: Eigenfrequencies and modeshapes of the structure are determined under still water conditions.
3. *Identification of possible excitation frequencies*: It is known that eigenfrequencies depend on added mass. When VIV occurs along the structure variations in added mass will appear. Thus, iteration for each eigenfrequency is required to find response frequencies.
4. *Evaluation of excitation zones for corresponding frequencies*: In order to assign each response frequency to an excitation zone an energy criterion is applied. Excitation zones are described by two methods based on the presence of overlapping between zones; time sharing method and space sharing method.
5. *Response Calculation*: Dynamic equilibrium equation is solved iteratively with findings

from 3rd and 4th steps. Iteration lasts until non-linear excitation and damping models are consistent with the structures' response.

6. *Post-Processing*: Fatigue accumulation of the structure is investigated during this step.

3.1.1 Model For Added Mass Coefficient

In VIVANA, added mass coefficients are determined by using contour plots of Gopalkrishnan (1993), see Figure 2.1.6. As mentioned before the change in oscillation amplitude is neglected while defining added mass. In order this assumption to be valid the non-dimensional amplitude is taken to be equal to 0.5. This results the pattern of added mass coefficient as a function of non-dimensional frequency in Figure 3.1.1.

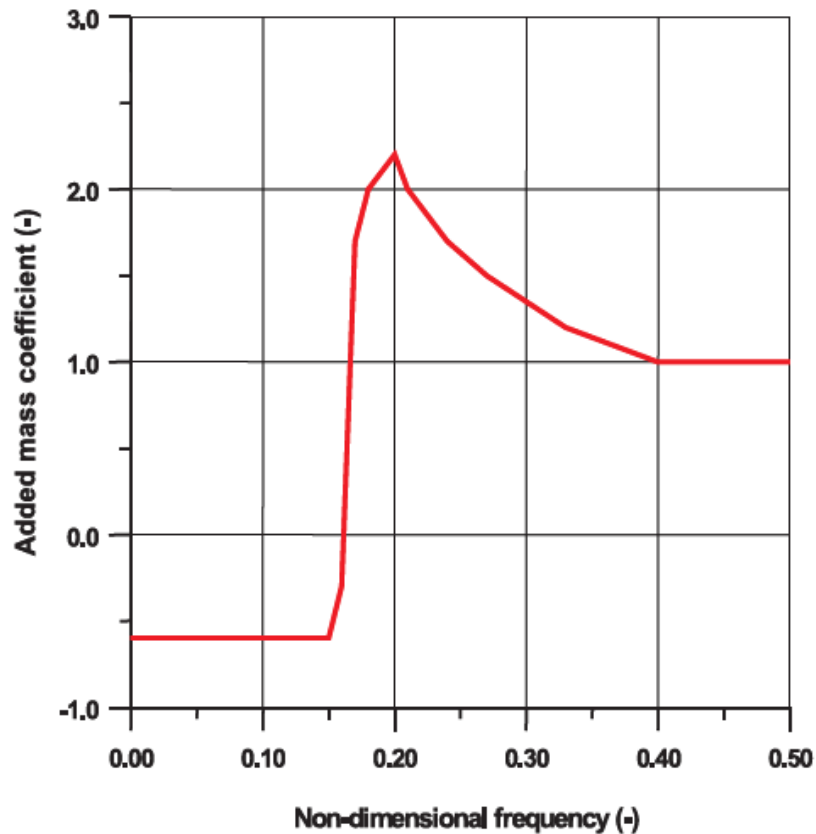


Figure 3.1.1: Added mass variation as a function of non-dimensional frequency (Passano et al., 2014)

3.1.2 Model For Excitation Force

The excitation force is a component of the hydrodynamic force which is caused by VIV along the structure. It is in phase with the response velocity and can be defined for unit length as:

$$F_e = \frac{1}{2}\rho C_e D U^2 \quad (3.1.1)$$

The process of evaluating the excitation force coefficient C_e is similar to the one followed for the added mass coefficient C_a . Based on the contour plots of Gopalkrishnan in order to determine which frequencies are dominant in the dynamic response of the structure, non-dimensional frequency range with largest C_e values should be chosen. Which turns out to be in the range of $0.125 \leq \bar{f} \leq 0.3$ (Figure 2.1.7).

Furthermore, the relation of non-dimensional amplitude A/D versus C_e is crucial to mention about since VIVANA considers C_e as a function of A/D . Figures 3.1.2 and 3.1.3 illustrate how these two parameters are related.

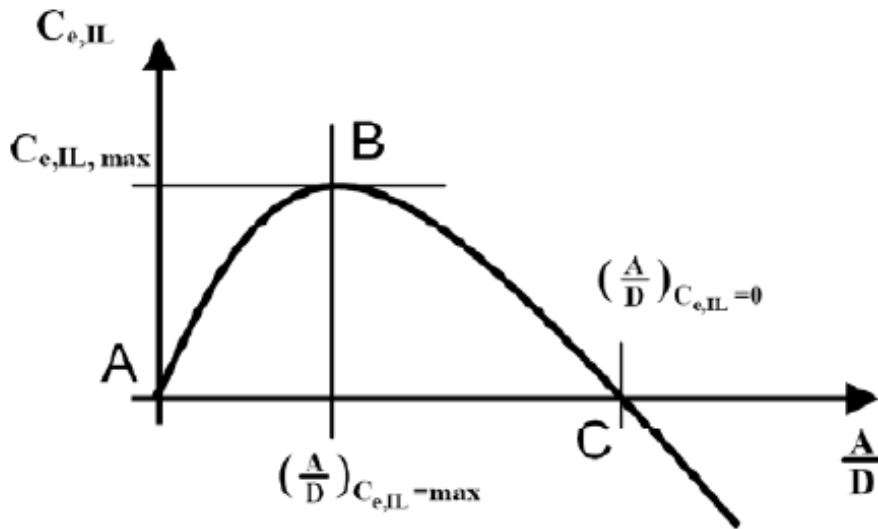


Figure 3.1.2: IL Excitation force coefficient as a function of A/D (Larsen et al., 2008)

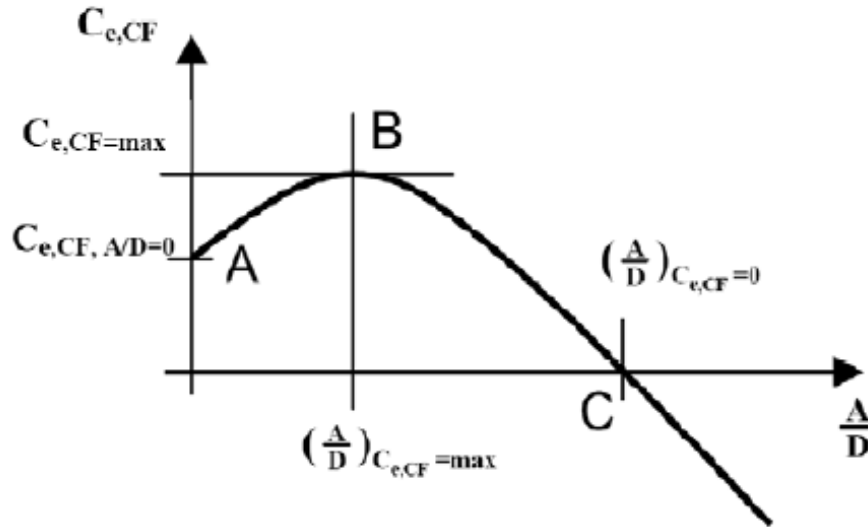


Figure 3.1.3: CF Excitation force coefficient as a function of A/D (Larsen et al., 2008)

Both in CF and in IL direction, when the response amplitude increases C_e increases also. However, at certain point B both curves reach a peak and start to decrease as response amplitude becomes larger. At point C , C_e plummeted to zero and further that point becomes negative. Being C_e negative means that it acts as a damping force and there is an energy transfer from structure to the fluid. That is why VIV is called a self-limiting process.

3.1.3 Excitation zones

One method of identifying excitation zones is the time sharing method. In this method the purpose is to associate each point of the structure with only one response frequency for a given time. That means there will be one active frequency during this period. The duration which indicates for how long this frequency will act can be calculated as below:

$$T_i = T \frac{E_i}{\sum_{n=1}^k E_i} \quad (3.1.2)$$

Where

$$E_i = \int_{L_{e,i}} U^3(s) D^2(s) (A/D)_{C_e=0} \partial s \quad (3.1.3)$$

E is the energy criterion for evaluating which frequency is more likely to lead in an excitation

zone with a length of $L_{e,i}$. Frequency values with larger E dominates their excitation zone. This means that since the time sharing method allows overlapping a higher E will excite the structure in that specific part. An illustration of overlapped excitation zones by time sharing method is shown below.

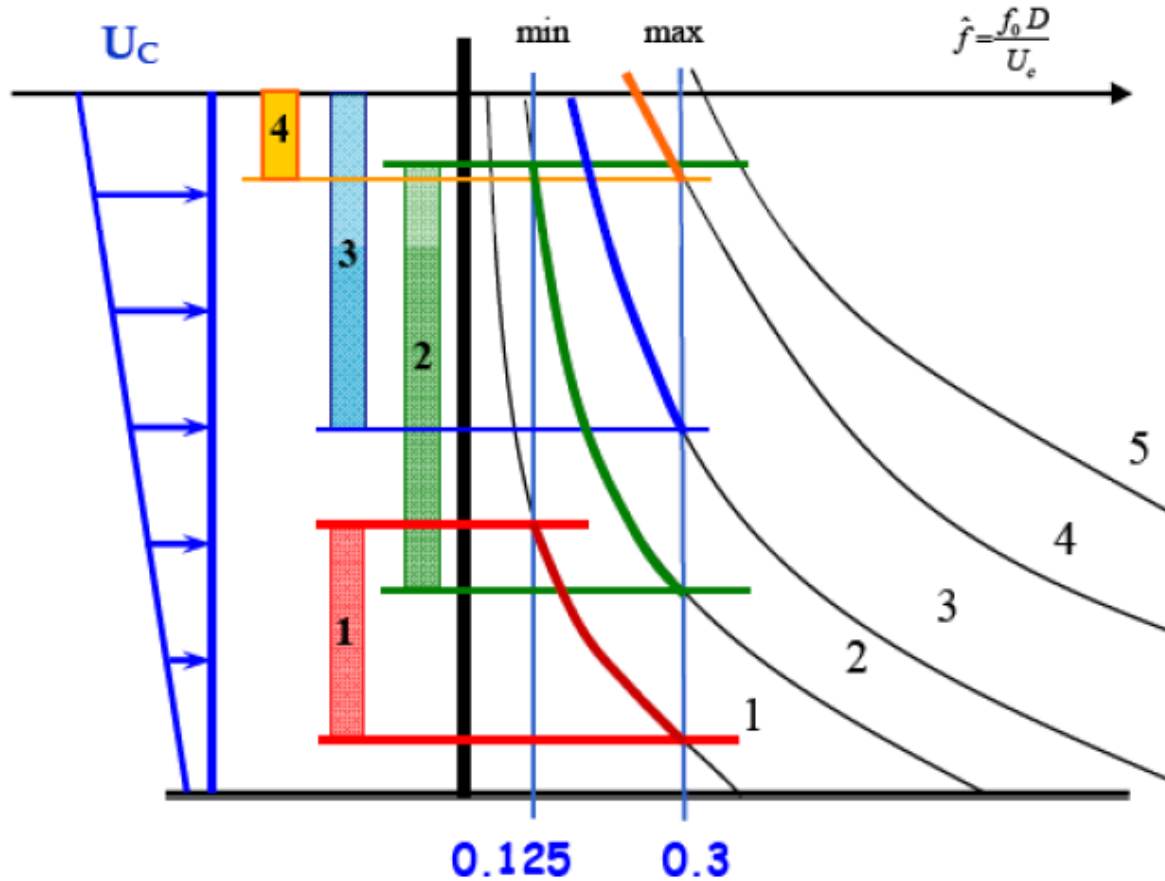


Figure 3.1.4: Excitation zones by time sharing method (Passano et al., 2014)

On the other hand, unlike the time sharing method, the space sharing method is based on allowing different frequencies to act simultaneously. Besides, excitation zones do not vary with time. Furthermore, the same energy principle is valid in this case also. As it can be seen in below figure, excitation zones are assigned according to ranking of frequencies by Equation 3.1.3.

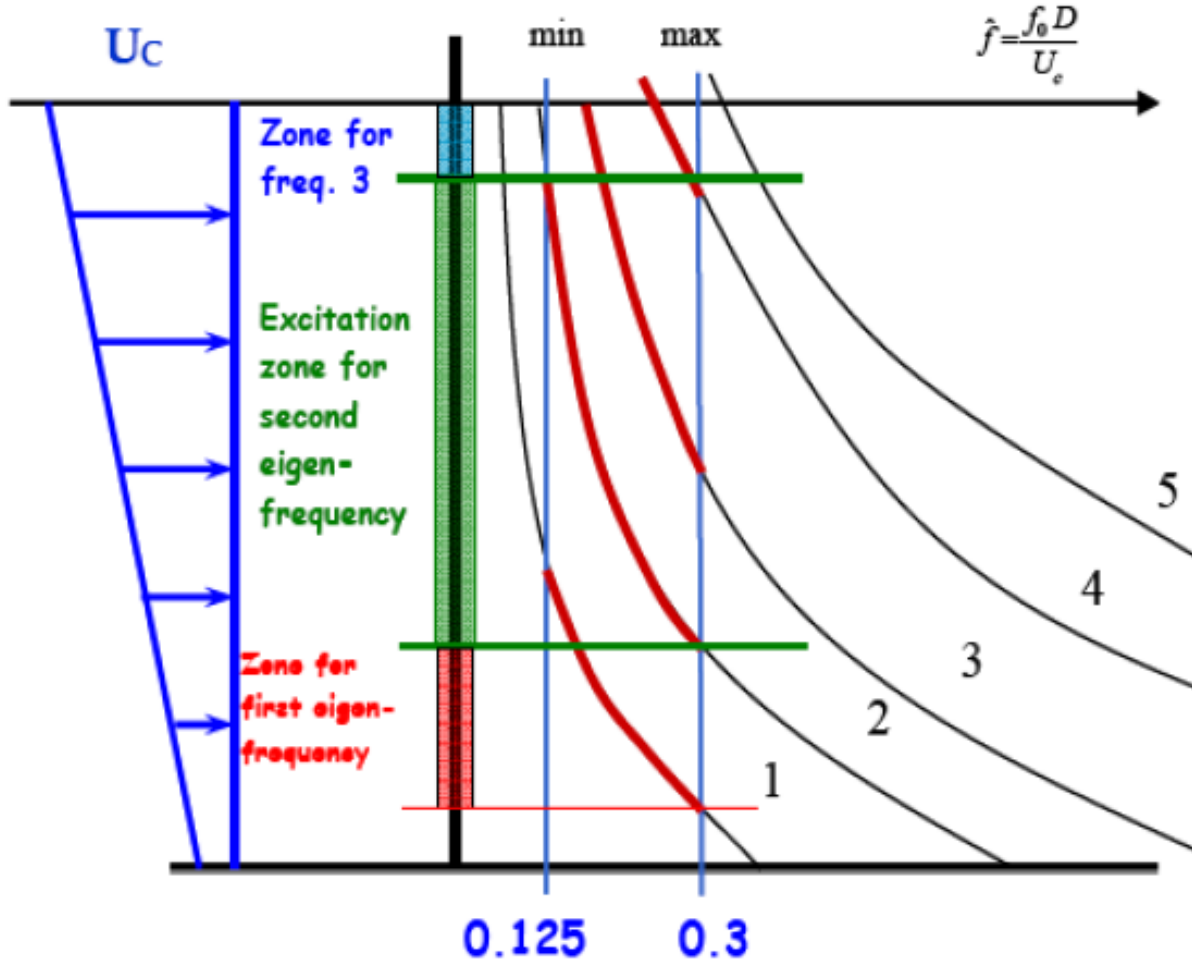


Figure 3.1.5: Excitation zones by space sharing method (Passano et al., 2014)

3.1.4 Computing the response

Having calculated all necessary hydrodynamic coefficients, dynamic equilibrium equation is solved in order to obtain structure's response.

$$M\ddot{r}(t) + C\dot{r}(t) + Kr(t) = F_e(t) \quad (3.1.4)$$

Since this analysis is performed in frequency domain, excitation force F_e and response r need to be defined as time-harmonic functions:

$$F_e(t) = X e^{i\omega t} \quad (3.1.5)$$

$$r(t) = xe^{i\omega t} \quad (3.1.6)$$

Before substituting these terms into dynamic equilibrium equation, it should be noted that damping matrix C is proportional to stiffness matrix K . Besides, VIVANA applies Venugopal(2004) damping model to construct damping matrix.

Furthermore, by replacing 3.1.5 and 3.1.6 into 3.1.4 and also by separating hydrodynamic and structural mass and damping, frequency domain formulation of dynamic equilibrium is finally reached:

$$-\omega^2(M_s + M_H)x + i\omega(C_s + C_H)x + Kx = X_L \quad (3.1.7)$$

Here X_L is the excitation force vector having non-zero values inside the excitation zone. Thus, consecutive iterations are required until solutions will converge to reasonable quantities for the response and the excitation force.

3.2 SHEAR 7 Model

Shear 7 is an other software that operates in the frequency domain to predict the response of slender marine structures due to VIV. This program has some significant differences from VIVANA. To begin with, it uses mode superposition to calculate the response in the presence of linearly varying tension along the structure. However, the difference between maximum and minimum tension values should not be excessive in order to obtain accurate results for the structural response. Furthermore, instead of identifying which frequencies excite the structure as VIVANA does, SHEAR 7 identifies the modes having potential to be excited. According to identified number of excited modes, the program can estimate locking or non-locking responses. It may be either a single mode locking or multi-mode non-locking response .

The program computes natural frequency, mode shape and the curvature for each mode in the first place (Vandiver & Li, 2005). Then, modes which are most likely to be excited are evaluated by comparing highest and lowest excitation frequencies to the natural frequency. An illustration of this process can be seen in Figure 3.2.1.

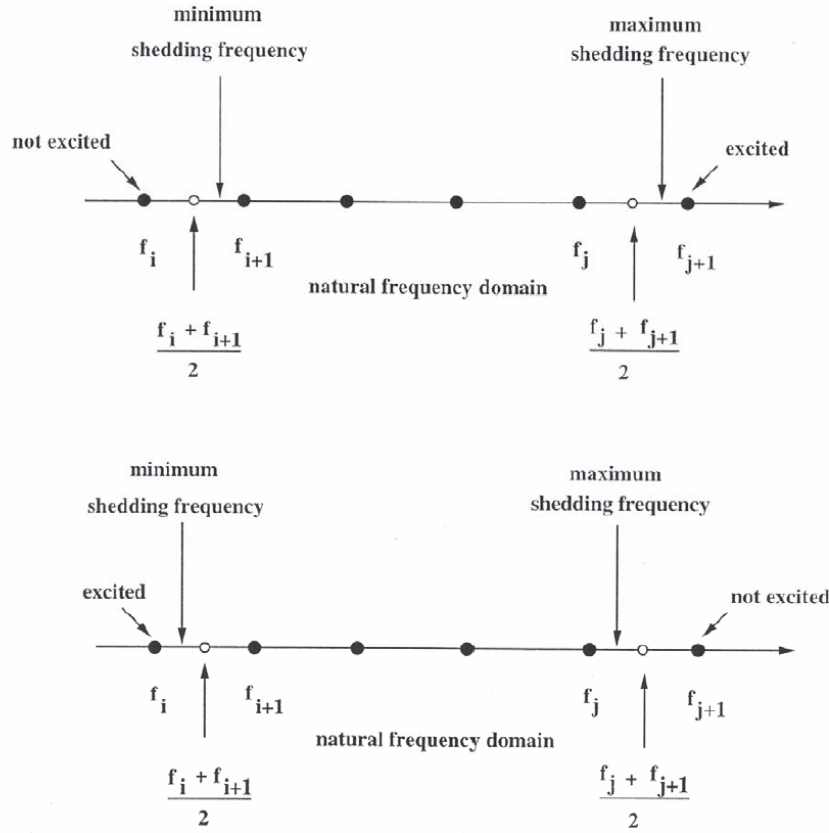


Figure 3.2.1: Evaluation of excited modes (Vandiver & Li, 2005)

3.2.1 Solution by Mode Superposition

To compute the structure's response superposition of vibration modes are calculated. First, the total power generated by mode r needs to be described (Vandiver & Li, 2005):

$$\Pi^r = \frac{|Q_r|^2}{2R_r} \quad (3.2.1)$$

Where modal force Q_r and modal damping R_r are calculated by below equations:

$$Q_r = \int_{L^r} \frac{1}{2} \rho C_e D(x) U^2(x) Y_r(x) \partial x \quad (3.2.2)$$

$$R_r = \int_{L-L^r} R_h(x) Y_r^2 \omega_r \partial x + \int_0^L R_s(x) Y_r(x)^2 \omega_r \partial x \quad (3.2.3)$$

When calculating modal force, no iteration performed for excitation force coefficient C_e . It is

chosen based on the maximum expected reduced velocity U_R . Y_r stands for mode shape of mode r . In addition, modal damping consists of hydrodynamic R_h and structural damping R_s . While R_s affects on the whole structural length, R_h affects on the region of the specific mode r .

Furthermore, it should also be noted that the power for each mode should be normalized to unity. A user input as a limit value for the power ratio is required to identify which modes that will be excited. Every mode above the limit is assumed to be excited. In this stage Eqn. 2.1.4 is to be recalled to explain length of the power-in region L^r . A reduced velocity range for the power-in region of each mode should be defined to see the length of the structural part which contributes to the response of each mode. If a certain reduced velocity of a mode at any location is into the limits of the U_R range for this mode, excitation of the structure by fluid will take place.

When the structure is divided into power-in regions, the number of them is equal to the number of modes that are above the pre-defined power ratio limit, see Figure 3.2.2. The same range of reduced velocity applies for each region however U_R varies with location due to different natural frequency in each region. Each mode has power-in (excitation) and power-out (damping) region. On the other hand, in case of overlapped modes, program handles it by reducing overlapped length of each mode equally until they do not overlap anymore. An illustration of how power-in regions are divided can be seen in Figure 3.2.3.

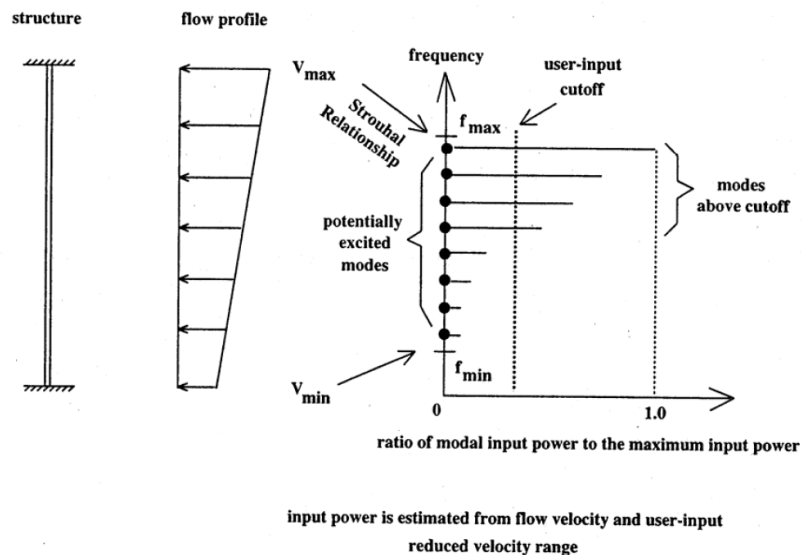


Figure 3.2.2: Modes of interest by power-in ratio (Vandiver & Li, 2005)

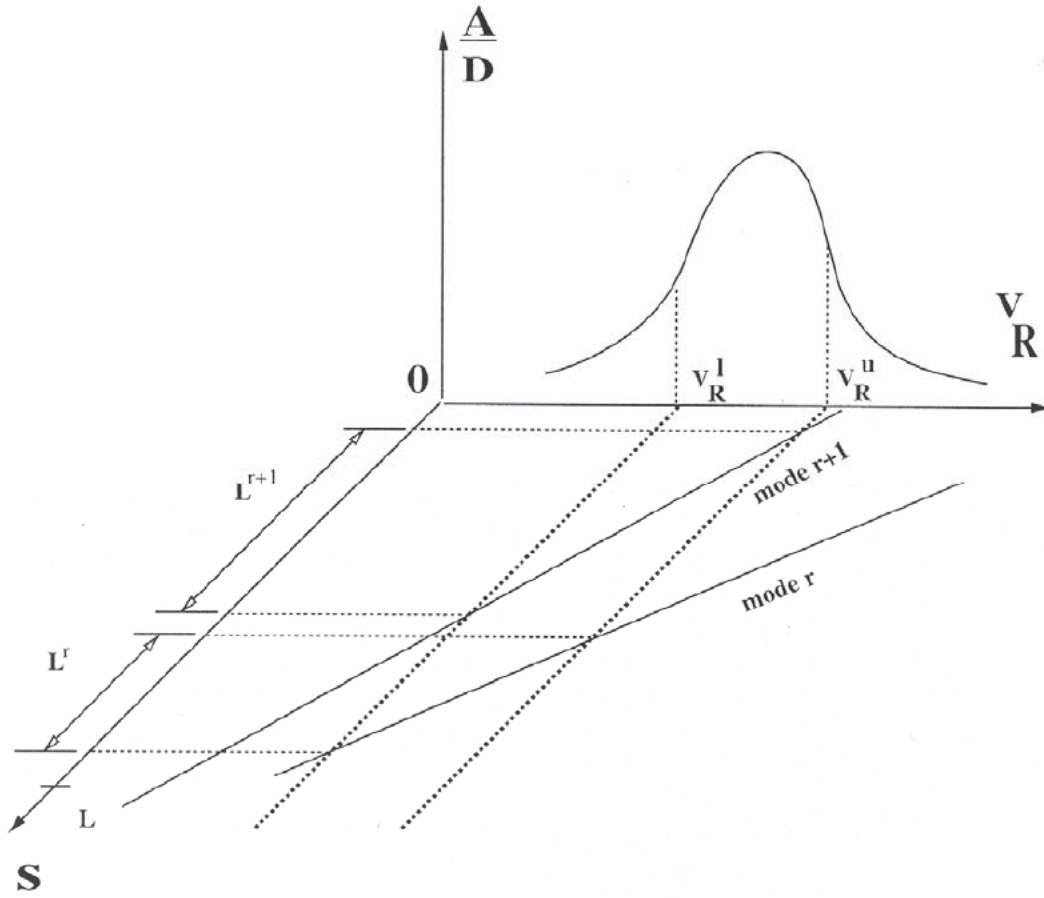


Figure 3.2.3: Division of power-in regions (Vandiver & Li, 2005)

Moreover, since there is going to be an equilibrium between power in and out the system, input and output power values for each mode should be evaluated. To do so, dynamic equilibrium equation for a taut cable is implemented:

$$(M_S + M_A)\ddot{y} + (R_S + R_H)\dot{y} - Ty'' = F_e(x, t) \quad (3.2.4)$$

As it can be seen, mass includes both structural and added mass as in VIVANA model. Another common thing with VIVANA model is that damping is split into two as structural and hydrodynamic damping. Besides, response and excitation force depend on both time and space. Response can be represented by a combination of mode shapes and modal displacement (Vandiver & Li, 2005).

$$y(x, t) = \sum_r Y_r(x) q_r(t) \quad (3.2.5)$$

Replacing 3.2.5 into 3.2.4, equilibrium equation for modal analyses is obtained.

$$M_r \ddot{q}_r(t) + R_r \dot{q}_r(t) + K_r q_r(t) = F_r(t) \quad (3.2.6)$$

Modal force F_r for mode r can be calculated by:

$$F_r(t) = \int_0^L |Y_r(x)| F_e(x, t) \partial x \quad (3.2.7)$$

Where, excitation force F_e is given as:

$$F_e(x, t) = \frac{1}{2} \rho D U^2(x) C_e \sin(\omega_r t) \quad (3.2.8)$$

Then, multiplication of modal velocity with excitation force yields input power for r th mode:

$$\Pi_r^{in} = \int_{L^r} \frac{1}{2} \rho D U^2(x) C_e \sin(\omega_r t) |Y_r(x)| \dot{q}_r(t) \partial x \quad (3.2.9)$$

Where, A_r and ω_r being displacement amplitude and frequency for the specific mode, respectively, modal velocity is equal to:

$$\dot{q}_r(t) = A_r \omega_r \sin(\omega_r t) \quad (3.2.10)$$

Furthermore, output power is calculated based on damping force F_d :

$$F_d = \int_L R(x) Y_r^2(x) \dot{q}_r(t) \partial x \quad (3.2.11)$$

$$\Pi_r^{out} = \int_L R(x) Y_r^2(x) \dot{q}_r^2(t) \partial x = \int_L R(x) Y_r^2(x) A_r^2 \omega_r^2 \sin^2(\omega_r t) \partial x \quad (3.2.12)$$

Then, input and output power are balanced by their time average values:

$$\frac{A_r}{D} = \frac{\frac{1}{2} \int_{L^r} \rho U^2(x) C_e |Y_r(x)| \partial x}{\int_{L-L^r} R_h(x) Y_r^2(x) \omega_r \partial x + \int_0^L R_s(x) Y_r^2(x) \omega_r \partial x} \quad (3.2.13)$$

Here the excitation force coefficient is given as an input by user. Iterations are performed in

order to obtain an agreement between damping and the excitation force coefficient. When the difference between two successive values of obtained for 3.2.13 is sufficiently small, convergence is assumed to be reached. The total response of the structure can then be computed by the final modal responses .

Chapter 4

Time Domain VIV Model

As mentioned before, a time domain VIV model has to be implemented for taking into account all non-linearities that can occur during the structural analysis. In this thesis, a step by step time integration will be performed to calculate structural response and further fatigue damage accumulated by the riser. During the analysis process, CF and IL effects on the structure will be evaluated separately. The proposed models by Thorsen et al. (2014), Ulveseter et al. (2017) and Ulveseter et al. (2018) are followed to perform time domain analysis.

4.1 Hydrodynamic Force Models in CF and IL Directions

The hydrodynamic force for both CF and IL directions are a combination of excitation, drag and inertia forces as a function of relative accelerations and velocities. Drag and inertia forces are defined by Morison's equation. Then the total force is expressed as

$$\begin{aligned} \mathbf{F}_n = & C_a \rho \frac{\pi D^2}{4} \dot{\mathbf{u}}_n - (C_M - 1) \rho \frac{\pi D^2}{4} \ddot{\mathbf{x}}_n + \frac{1}{2} \rho D C_D |\mathbf{v}_n| \mathbf{v}_n + \\ & \frac{1}{2} \rho D C_{e,y} |\mathbf{v}_n| (\mathbf{j}_3 \times \mathbf{v}_n) \cos \phi_{e,y} + \frac{1}{2} \rho D C_{e,x} |\mathbf{v}_n| \mathbf{v}_n \cos \phi_{e,x} \end{aligned} \quad (4.1.1)$$

Where, the equation for calculating excitation force coefficients for both direction is given by Thorsen et al. (2014) and Ulveseter et al. (2017) by assuming harmonic velocity

$$C_{e,x,y} = \lim_{T \rightarrow \infty} \frac{2}{T} \int_0^T C_{x,y}(t) \cos \omega t dt \quad (4.1.2)$$

In all the above equations, x and y refer to IL and CF directions, respectively, see figure 4.1.1. C_a is the added mass coefficient, C_D is the drag coefficient of Morison's equation. There is a

factor of 2 between IL and CF excitation force. That is due to the relation between their time derivatives of the instantaneous phases $\partial\phi_{e,x}/\partial t = 2\partial\phi_{e,y}/\partial t$ (Thorsen et al., 2014).

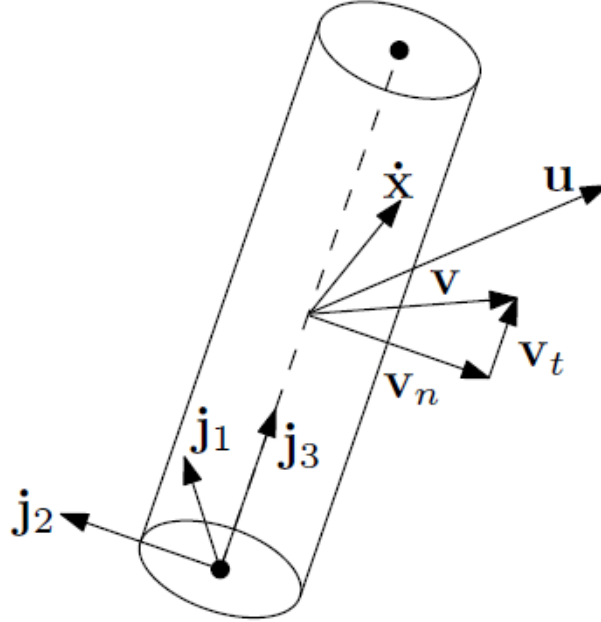


Figure 4.1.1: Local coordinate system and velocity components for a slender marine structure proposed by (Ulveseter et al., 2018)

Where, u and x are the current velocity and the displacement response of the cylinder, respectively. Thus, relative velocity vector is found by $\mathbf{v}_n = \mathbf{u}_n - \dot{\mathbf{x}}_n$ (Ulveseter et al., 2018). Excitation force has the same nature as given before in equation 3.1.1. The only difference is the additional cosine term to include excitation force's instantaneous phase ϕ_e .

4.2 Synchronization in IL and CF Directions

When the vortex shedding frequency, which is generally defined by the Strouhal number, see Equation 2.1.5, becomes equal to an eigenfrequency, synchronization phenomena takes place. That is the situation where energy input to the cylinder from the surrounding fluid occurs. It means that the structure is being excited by the fluid and response amplitude will keep increasing as long as lock-in continues. At a certain point, the magnified drag force expressed by Morison's equation will behave as a damping force and response amplitude will decrease. This is an indication of the VIV's self-limiting feature.

In order to have a better understanding on the synchronization model, the instantaneous phase of the relative cylinder velocity ϕ_r should be given. Thorsen et al. (2014) defined a function for CF vibration based on the relationship between ϕ_e and ϕ_r . Later, Ulveseter et al. (2017) applied the same equation in case of a pure IL vibration and obtained good results. The function can be written for both directions as

$$\frac{\partial \phi_e}{\partial t} = h(\phi_r - \phi_e) \quad (4.2.1)$$

Also, alternative form of the Equation 4.2.1 is given by Ulveseter et al. (2018)

$$h(\phi_r - \phi_e) = \frac{2\pi|v_n|}{D} \hat{f}_e \quad (4.2.2)$$

The relationship in Equation 4.2.2 was modified to approximate the non-dimensional excitation frequency at each time step during the time domain analysis. To do so, a frequency interval $\Delta \hat{f}$ need to be selected so that within the range excitation force will be always positive. Besides, the peak value \hat{f}_0 of the non-dimensional frequency in this range should be identified at which maximum response amplitude is observed. Above choices could be done based on Gopalkrishnan's contours from Figure 2.1.7 for CF direction and Aronsen's contours from Figure 4.2.1 for IL direction.

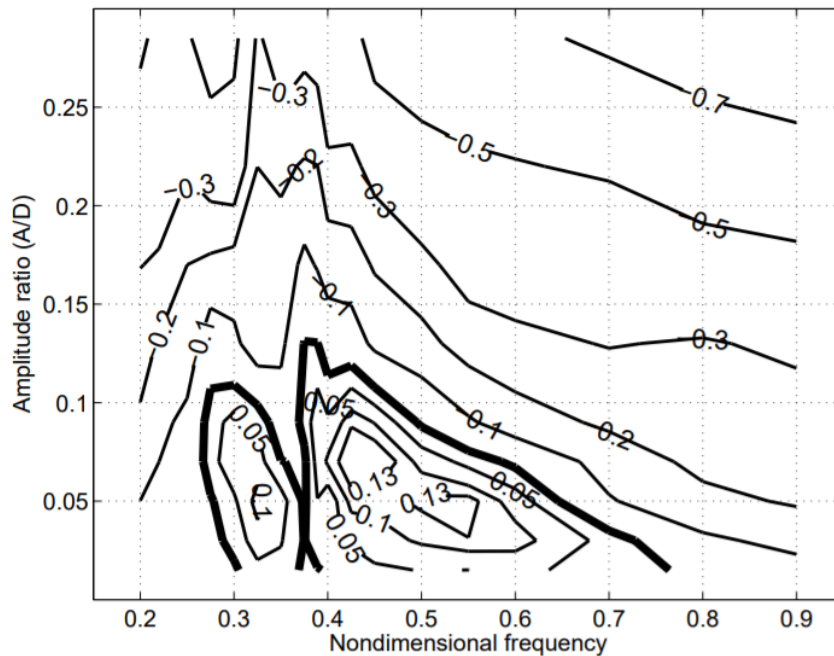


Figure 4.2.1: Excitation force coefficients in IL direction (Aronsen, 2007)

Furthermore, Ulveseter et al. (2018) formulated the non-dimensional frequency for CF and IL directions of oscillations as follows

$$\hat{f}_e = \hat{f}_0 + \Delta\hat{f} \sin(\phi_r - \phi_e) \quad (4.2.3)$$

While the frequency range and peak frequency remains the same for each time step, since phase difference between the excitation force and the response velocity vary, excitation frequency must be updated each step. The phase of portrait was introduced in (Thorsen et al., 2014) to calculate phase of the relative velocities. This is done by normalizing the velocity and acceleration vectors of the response to unity between small time intervals specified by a characteristic time increment. Then, the normalized acceleration vector is multiplied with -1 and located in the y-axis. The normalized velocity vector is located at x-axis. That way the phase of the relative velocity is calculated, see Figure 4.2.2.

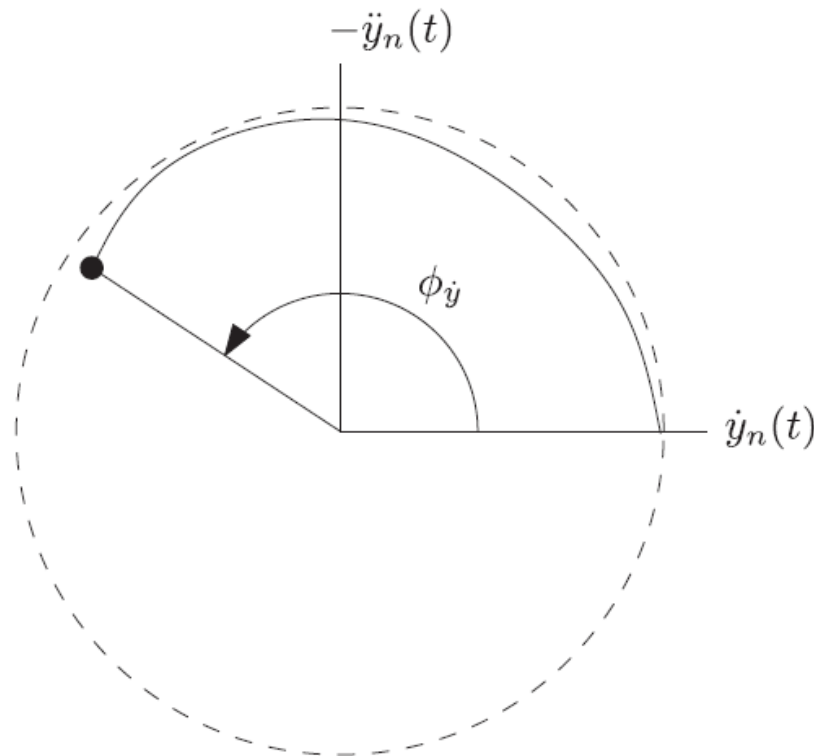


Figure 4.2.2: Phase of portrait method for CF direction (Thorsen et al., 2014)

On the other hand, the initial value of the phase excitation force can be given randomly. Variation of it in time need to be calculated based on lift and drag phase models for CF and IL

directions, respectively. Moreover, the response amplitude in each time step has to be known since the excitation force changes based on the variation in motion amplitude. The following integral can be applied between to successive time step. In addition figure 4.2.3 shows what equation 4.2.4 means.

$$A_x = \frac{1}{2} \int_{t_1}^{t_2} |\dot{x}| dt \quad (4.2.4)$$

Although it seems an equation for IL direction, it is applicable also for calculating CF direction response amplitude.

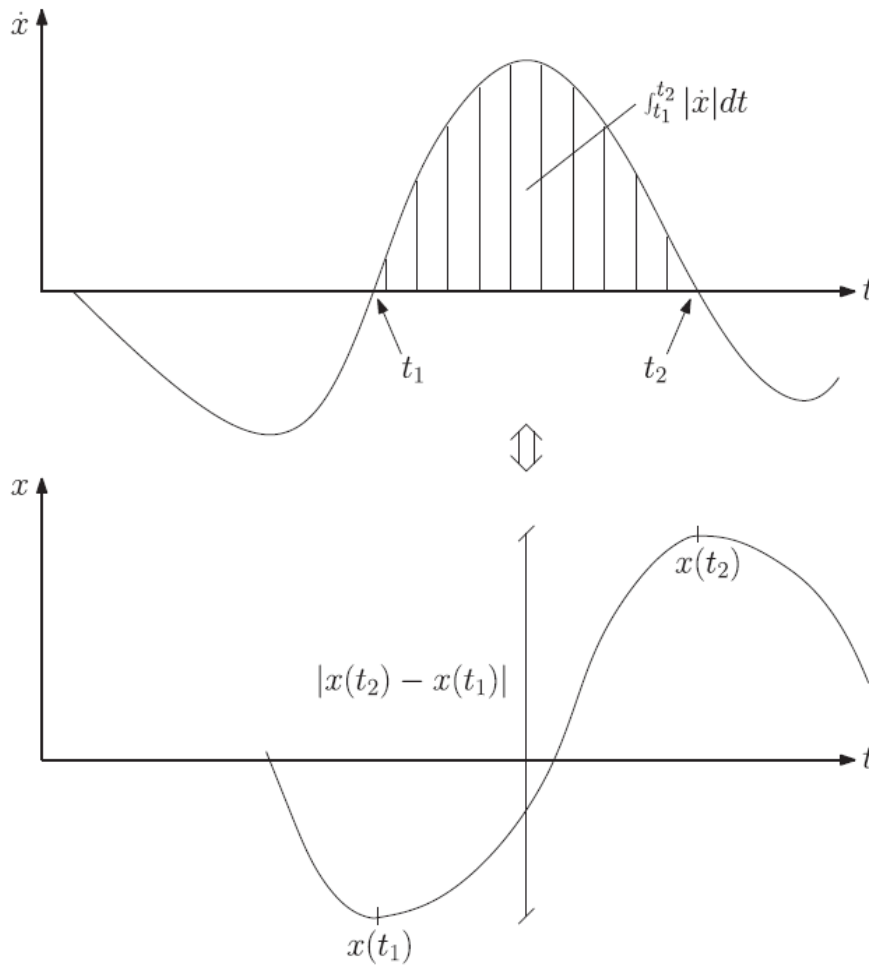


Figure 4.2.3: Time crossings for equation 4.2.4 (Ulveseter et al., 2017)

4.3 Solving Dynamic Equilibrium Equation in Time Domain

The dynamic equilibrium in time domain is written as

$$\mathbf{M}\ddot{\mathbf{r}}(t) + \mathbf{C}\dot{\mathbf{r}}(t) + \mathbf{K}\mathbf{r}(t) = \mathbf{F}(t) \quad (4.3.1)$$

The global mass matrix M includes both dry mass and added mass. The damping matrix C is built by using Rayleigh damping method. K is the global stiffness matrix consisting of bending and geometric stiffness. The external load vector is to be chosen between IL and CF force component decomposed from the compact form of Equation 4.1.1 depending on the direction of interest. Having given all the input a step by step Newmark- β time integration is performed.

Chapter 5

CABLE TECHNOLOGY

5.1 General Design Concepts of Subsea Dynamic Power Cables

Subsea dynamic power cables are widely applied in renewable energy industry. They are essential for transporting electrical power. Failure of such structures may have detrimental consequences on structural integrity and can cause loss of production. Hence, special care should be given to design process. The design requirements will be explained with reference to DNVGL-ST-0359 (DNV, 2016) and DNV-RP-F401 (DNV, 2012). Below Figure 5.1.1 shows how a typical cross-section for a subsea power cable looks like.

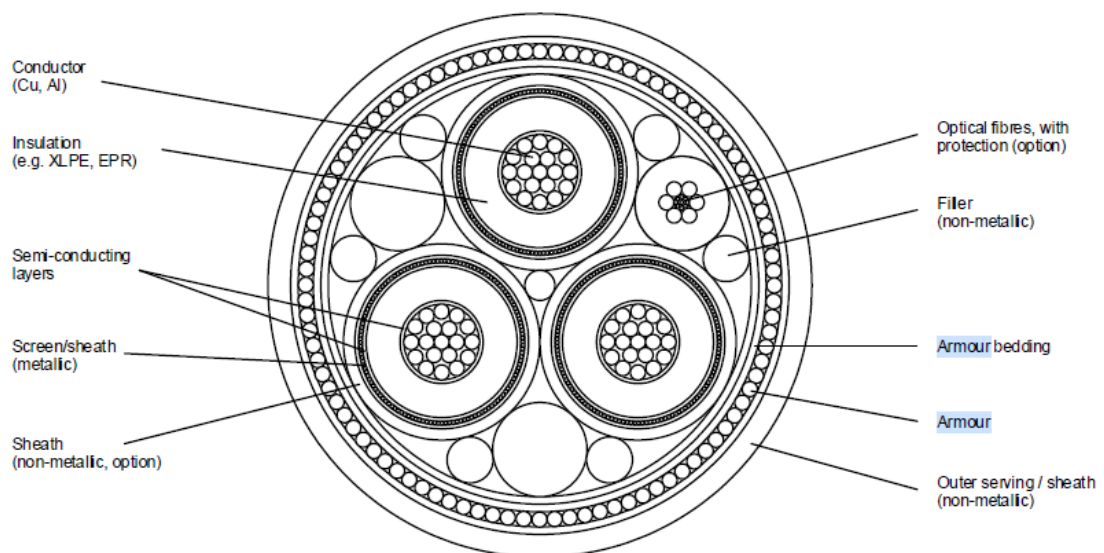


Figure 5.1.1: A typical subsea power cable cross section (DNV, 2016)

As it can be seen from figure 5.1.1, conductor is made of copper or aluminium. However, copper is more favourable since it can be used for smaller cross-sections. Thus, the amount of steel that surrounds copper conductors are much less than the required amount for aluminium conductor. Conductor can be insulated by cross-linked poly-ethylene (XLPE) or ethylene propylene rubber (DNV, 2016).

Armour layer consists of armour wires which are generally made of carbon steel. Armour carries huge importance regarding to resistance against external forces acting on the cross section. In addition, sheath prevents water to penetrate inside the conductor. Besides, outer sheath is the layer covering whole cable system made of a non-metallic material such as polypropylene.

Furthermore, DNV (2016) proposes some functional requirements for the design of subsea power cables. First of all, the design must fulfill the safety criterion while operating under the influence of expected design loads, see section 5.1.1 . Structure should also be available to be installed, repaired and inspected.

One of the most critical subjects regarding the design process of dynamic power cables is the electrical systems. There are two options for a subsea power cable's electrical system namely; direct current(DC) and alternating current(AC). AC systems are preferred for subsea power cables because, it is simple to change voltage when necessary. Generally, three conductors covered with insulators are placed in a three-core cable. This system is called three-phase system and requires larger cross section than DC systems. However, the required transformer size for AC systems are much smaller than ones for DC systems. Below Figure 5.1.2 illustrates the difference between single phase and three phase AC systems.

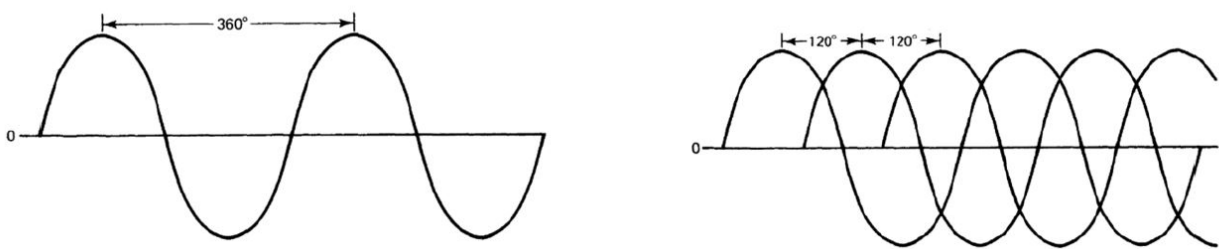


Figure 5.1.2: Single and three phase AC voltages (Patrick et al., 1999)

5.1.1 Relevant Loads for design

A variety of load effects are considered in DNV (DNV, 2012) for the design process of flexible pipes. These load effects are also valid for dynamic power cables.

- *Functional Loads*

These are the loads resulted by the interaction between riser itself and the surrounding environment during various stages of design life such as construction, installation and operation. Structure weight, soil interaction, hydrostatic forces etc.

- *Interference Loads*

Trawl interference is the most common of the interference loads. Pipeline hooked by an anchor may be an example for this type of loading.

- *Accidental Loads*

Accidental loads are defined by annual exceedance probability. If certain load case has a probability less than the specified annual exceedance probability, then that load case is classified as an accidental load.

- *Environmental Loads*

For offshore structures such as flexible risers, cables and pipelines wind and wave loads are primary environmental effects.

Environmental loads are stochastic loads which results in stochastic response of the structure. Therefore, probability distributions should be used to represent environmental loads, especially hydrodynamic forces due to waves and currents. Then the characteristic loading can be obtained by further analysis as basis for capacity checks of failure modes(Sævik, 2019a). Moreover, different phases are included to capacity check calculations based on the limit state concept. Serviceability Limit State (SLS), Ultimate Limit State (ULS), Fatigue Limit State (FLS) and Accidental Limit State (ALS) are the limit states taken into account, see (DNV, 2012) for further details about these terms.

In a statistical representation, a safety factor for each limit state is applied by a design format to get a failure probability within a reasonable range. Characteristic load and the resistance are defined by probability density functions, see Figure 5.1.3. By reducing the resistance or by increasing the load, a more conservative design can be reached with the identification of uncertainties.

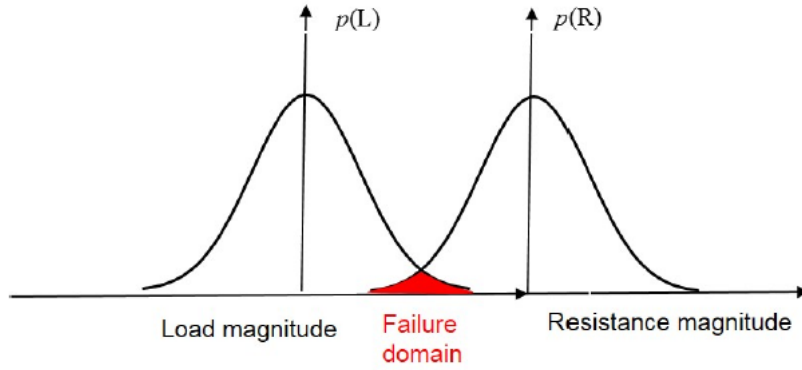


Figure 5.1.3: Probability Density Functions for Characteristic Load and Structural Resistance (Sævik, 2019a)

As mentioned before, design formats are used for setting the safety factor to each limit state. These formats are Load and Resistance Factor Design (LRFD) and Allowable Stress Design (ASD). Formulation for LRFD is suggested by DNV (DNV, 2016)

$$S_d \leq R_d \quad (5.1.1)$$

Where, S_d and R_d are design load effect and design resistance, respectively. In addition, characteristic load effect F_k is to be used with load factor γ_f to calculate the design load. It should be noted that characteristic load effect for each loads defined in Section 5.1.1 with the corresponding load factors, have to be included in the calculation of design load.

$$F_d = \gamma_f F_k \quad (5.1.2)$$

The design load effect can be then calculated by a combination of predefined load effects in Eqn. 5.1.2. On the other hand, the expression for evaluating design resistance can be written as

$$R_d = \frac{R_k}{\gamma_M} \quad (5.1.3)$$

Where R_k is the characteristic resistance which can be obtained by testing and γ_M is the material factor. LRFD method is very suitable if response varies non-linearly with respect to loading. Because, in LRFD loads are increased by load factor and the resistance is decreased by material factor. Hence, LRFD format is a good practise for plastic design. Whereas, ASD

format is based on a linear relation between loading and the response. The reason is that, safety factor is used in the right hand side to limit loading within the elastic limit. Following expression describes ASD format based on stresses (Sævik, 2019a)

$$\sigma \leq \eta\sigma_y \quad (5.1.4)$$

σ_y and η refer to the yield stress and the utilization factor. Lastly, ASD format is the desired format for the designing of subsea power cables.

5.1.2 Failure Modes

Subsea power cables are subjected to a variety of different failure modes. One of these failure modes is overloading of cross-section. The use of helix steel layers are very common to deal with excessive yielding due to overloading. In order to do that, the required amount of steel suggested by API (American Petroleum Institute, 2008) should be calculated by practising ASD format.

Moreover, layers of non-bonded structures such as dynamic power cables are free to slide onto each other. This sliding effect lowers the bending stiffness. This low bending stiffness makes free-spans on the sea bed to be seen less likely, however it lowers global buckling resistance. Furthermore, coupling between bending stress and pressure is not significant. Since the holes on the surface of the outer sheath lead to no pressure difference between the cross section and the water at any point of the cable. Thus, external pressure is not an issue for sub sea power cables as opposed to steel tube umbilicals.

Local buckling is also an important failure mode to consider which affects on armour wire through excessive compressive stress in the armour. The result is the displacement of armour wire in lateral or radial directions. Displacement in radial direction is known as bird-caging phenomenon (Sævik, 2019a). Local buckling generally occurs during the installation phase in the deep water. In shallow waters, this failure mode is not that significant. Anti-buckling tape is one of the most effective remedies for this problem which constraints radial displacement of armour wire.

Fatigue failure is controlled by armour layer. Fatigue failure is generally caused by the friction between the layers as they slide onto each other. Critical spots for this failure mode are the locations with the highest curvature and consecutively highest bending moment. In the past, anti-wear tapes were not used as fatigue protection method. Instead, the reduction in the armour's cross-section with respect to time were estimated by applying a variety of wear

models. It should be noted that dry air environment and an outer sheath without leakage were assumed. When the stress range resulted by cross section reduction exceeds the fatigue limit which is generally the stress range corresponding to 10^6 cycles in constant amplitude loading, fatigue failure occurs. This approach is called fatigue limit approach (Sævik, 2019a).

Nowadays, due to the additional failure modes causing water and corrosive substance to penetrate from outer sheath into the cross-section, Miner sum approach is widely used instead fatigue limit approach.

5.2 Fatigue of Dynamic Power Cables

As mentioned in previous section, the Miner sum is the preferred method for calculating accumulated damage on the marine structures. This approach can be expressed as follows

$$D = \sum_i \frac{n_i}{N_i} \quad (5.2.1)$$

Where total accumulated damage is indicated by D , n_i is the number of cycles for corresponding stress range $\Delta\sigma_i$ and N_i is the number of cycles until failure (As & Berge, 2017). Then the relation between N_i and $\Delta\sigma_i$ can be given by SN curve with the material parameters m and $\log A$

$$\log N_i = \log A - m \log \Delta\sigma_i \quad (5.2.2)$$

Nasution et al. (2014) stated that most critical location for fatigue accumulation in a subsea power cable is the point where cable connects the floater, see Figure 5.2.1 . At this location, the effects of gravity force and the forces caused by floater motions are significant. Gravity force creates a mean global tension \bar{T} followed by a mean global torque \bar{M}_T . Moreover, floater motions lead to dynamic effects. Heave and surge motions build dynamic tensile load ΔT which causes dynamic torque ΔM_T whereas dynamic curvature $\Delta\beta$ occurs due to pitch and roll motions. This dynamic curvature should be taken into account since it gives large bending moments and bending stresses.

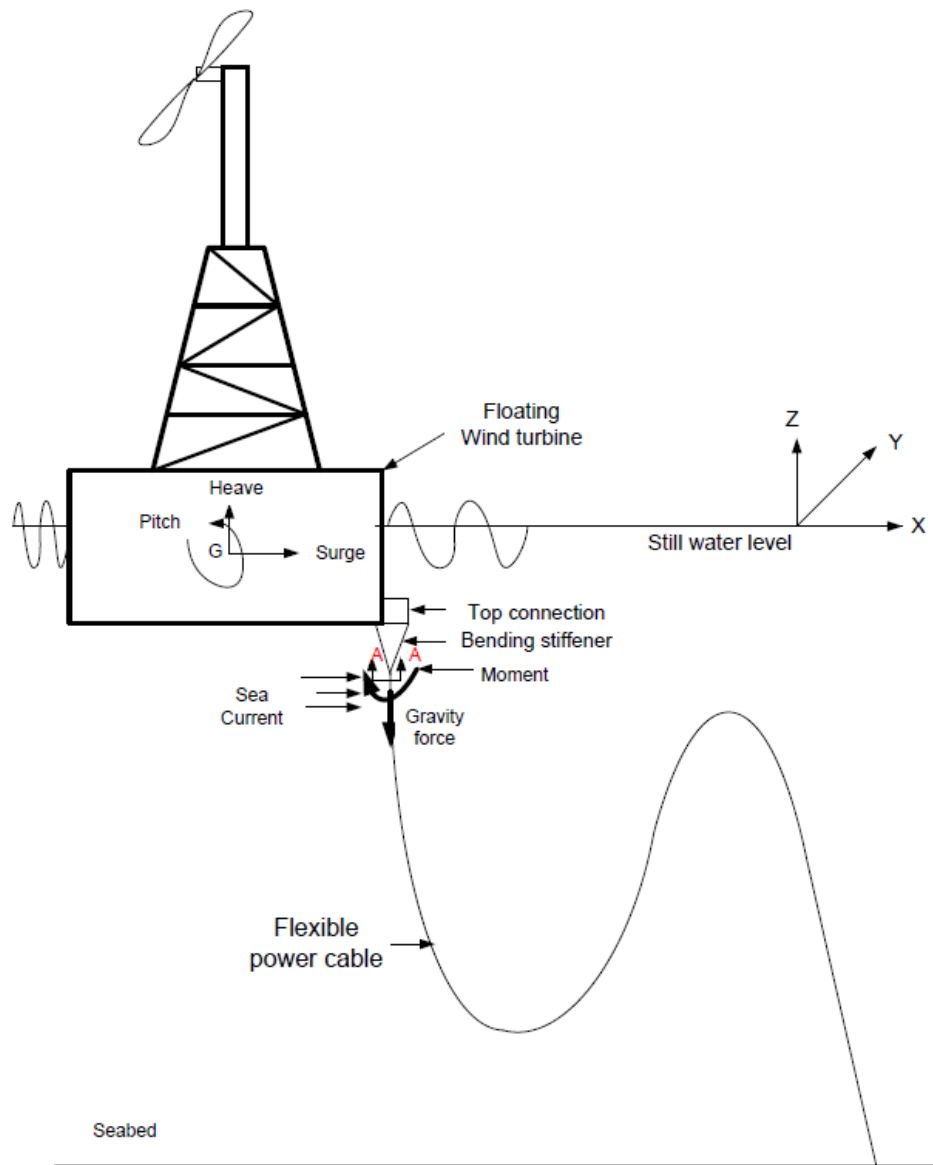


Figure 5.2.1: Dynamic power cable connected to the floating OWT, (Nasution et al., 2014)

According to Nasution et al. (2014), all these effects are transferred into the wires. For instance, mean and dynamic tension act on each wire in the form of tension and shear forces, respectively. In addition, local bending moments and axial friction forces caused by dynamic bending moment take place in each wire. Figure 5.2.2 illustrates these forces and moments in the power cable's cross section.

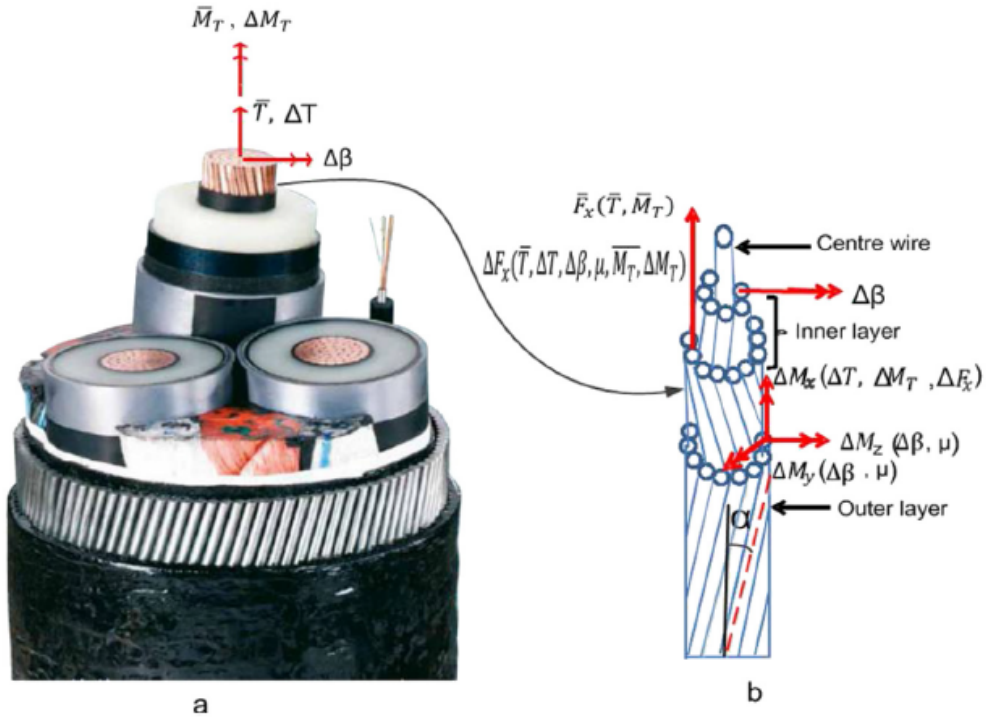


Figure 5.2.2: Cross section of dynamic power cable with dynamic torque moment ΔM_x , dynamic bending moments ΔM_z and ΔM_y , mean axial force \bar{F}_x , dynamic axial force ΔF_x and friction coefficient μ , (Nasution et al., 2014)

When the wires are exposed to this combined loading, a common fatigue type for contacting metals called "fretting" may occur. With the increased lay angle α due to large curvature makes friction force higher. The friction coefficient μ has the same influence on the friction force also. Larger friction force could have detrimental consequences on the structure regarding to fretting type fatigue.

5.2.1 Mean Stress Correction

Sævik (2019a) stated that fatigue of the copper wires are multi-axial and can be defined as

$$\Delta\sigma = A - \alpha(\bar{\sigma})^\beta \quad (5.2.3)$$

Where $\bar{\sigma}$ is the mean stress and the other terms are constants to be found by fatigue testing. Most of the time uni-axial testing method is preferred with use of constant mean stress or constant load ratio which can be written as

$$R = \frac{\sigma_{min}}{\sigma_{max}} \quad (5.2.4)$$

The R value has normally a range between 0.1-0.5 to not include compression in the testing process. Since generally testing data are only available for only one R ratio, different stress ranges can be taken into account by using Goodman or Gerber methods, see Figure 5.2.3.

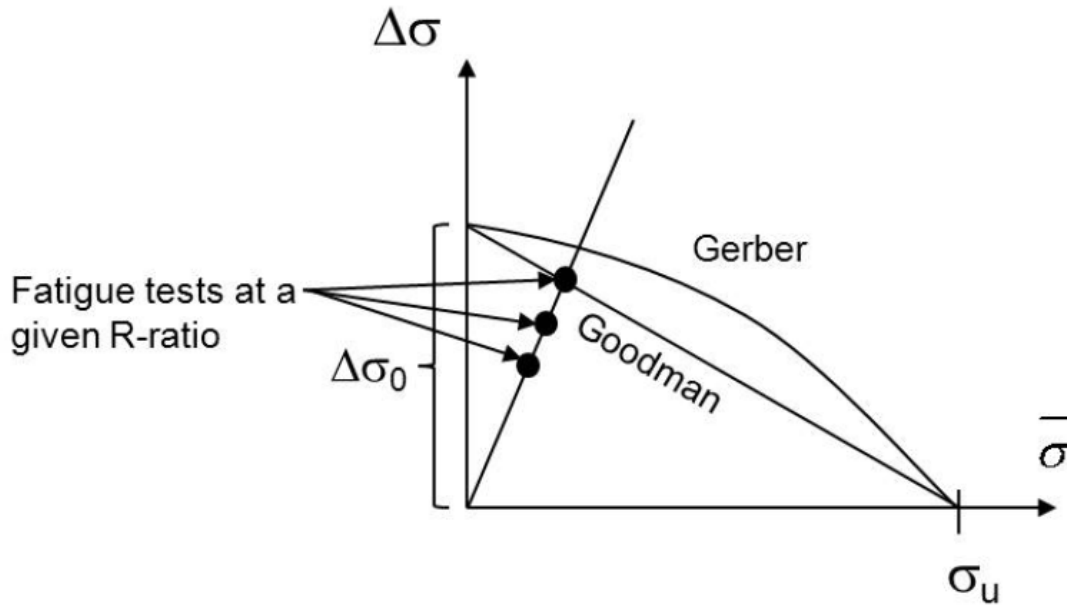


Figure 5.2.3: Haigh Diagram with Goodman and Gerber assumptions (Sævik, 2019a)

In Figure 5.2.3 $\Delta\sigma_0$ stands for the stress range for a load ratio $R=-1$. By using Goodman and Gerber assumptions, the stress range $\Delta\sigma$ is converted into $\Delta\sigma_0$ to obtain different mean stresses. Equations proposed by Goodman and Gerber are given respectively

$$\Delta\sigma_0 = \frac{\Delta\sigma}{1 - (\bar{\sigma}/\sigma_u)} \quad (5.2.5)$$

$$\Delta\sigma_0 = \frac{\Delta\sigma}{1 - (\bar{\sigma}/\sigma_u)^2} \quad (5.2.6)$$

Here, σ_u is the ultimate stress.

5.2.2 Analytical Model to calculate stresses

Nasution et al. (2014) proposed an analytical mode to calculate stresses in the longitudinal direction of the cable because, stresses in the longitudinal direction are the most critical ones with respect to fatigue (Passano et al., 2014). The longitudinal stress range was defined as follows

$$\Delta\sigma = \Delta\sigma_T + \Delta\sigma_{tc} + \Delta\sigma_{nc} + \Delta\sigma_f \quad (5.2.7)$$

Where;

- $\Delta\sigma_T$ \longrightarrow stress range due to dynamic tension
- $\Delta\sigma_{tc}$ \longrightarrow stress range due to transverse curvature of the wire
- $\Delta\sigma_T$ \longrightarrow stress range due to normal curvature of the wire
- $\Delta\sigma_{tc}$ \longrightarrow stress range due to friction

$\Delta\sigma_T$ can be calculated for each wire as follows

$$\Delta\sigma_T^i = E \cos^2 \alpha_i \frac{\Delta T}{EA_{full}} \quad (5.2.8)$$

Where, the axial stiffness EA_{full} for the whole cross section can be calculated by summing axial stiffness of each individual layer with n number of wires.

$$EA_{full} = EA \left(1 + \sum_{i+1}^m n_i \cos^3 \alpha_i \right) \quad (5.2.9)$$

Furthermore, $\Delta\sigma_{nc}$ for small lay angles α with curvature range $\Delta\kappa$ and polar coordinate angle ψ for expressing the helix position can be written as

$$\Delta\sigma_{nc} = R_{nominal} E \cos^2 \alpha_i \cos 2\alpha_i \Delta\kappa \cos \psi \sim R_{nominal} E \Delta\kappa \cos \psi \quad (5.2.10)$$

Where, $R_{nominal}$ is the nominal helix radius. Moreover, stress range caused by friction is given by

$$\Delta\sigma_f^i = \min \left(E \cos^2 \alpha_i R_i \Delta\kappa, \frac{\pi R_i \tau_i}{\sin \alpha_i A_i} \right) \quad (5.2.11)$$

Here the friction force per unit length can be derived by

$$\tau_i \simeq E\epsilon_c\mu \left(\sum_{j=i+1}^m \frac{n_j A_j \cos^2 \alpha_j \sin^2 \alpha_j}{n_i R_i} + \sum_{j=i}^m \frac{n_j A_j \cos^2 \alpha_j \sin^2 \alpha_j}{n_i R_i} \right) \quad (5.2.12)$$

with

$$\epsilon_c = \frac{T}{EA_{full}} \quad (5.2.13)$$

Where μ and T are friction coefficient and the tension, respectively.

5.3 Rainflow Counting For Cumulative Damage Analysis

In this thesis, the cumulative fatigue damage of the power cable due to VIV will be calculated by applying Rainflow counting. The name of the method is inspired by rain drops falling down from a pagoda roof. In this method, stress-strain response of the material is taken as a reference to count reversals. The procedure of counting is depicted in Figure 5.3.1; the individual cycle 2-3-2' forms a hysteresis loop and it is counted as one cycle. This procedure is repeated each time a hysteresis loop is closed. Closed hysteresis loops show how much energy is dissipated because of dislocation movements in the material.

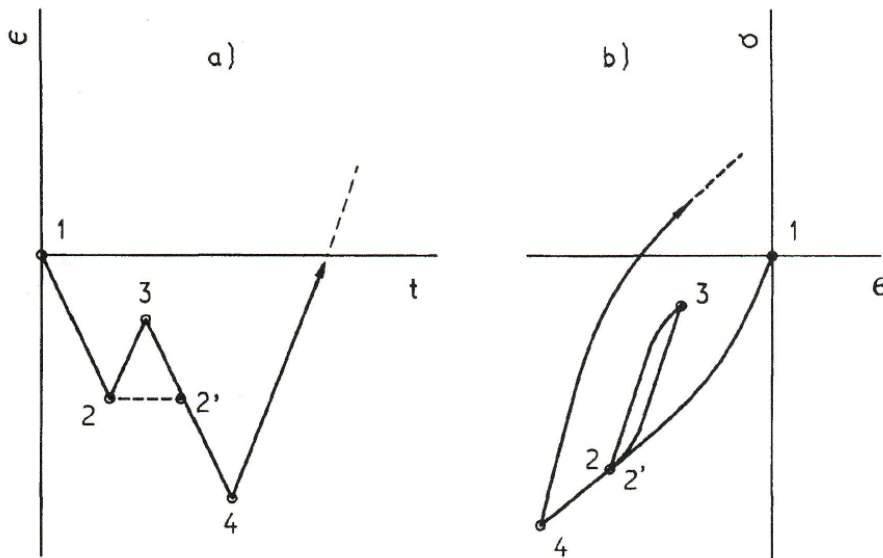


Figure 5.3.1: (a) Strain History and (b) corresponding stress-strain response (As & Berge, 2017)

As and Berge (2017) explain how rainflow counting works with reference to Figure 5.3.2 as follows:

1. Rain will flow down the roof initiating at the inside of each peak or valley. When it reaches the edge it will drip down.
2. The rain is considered to stop, and a cycle is completed, when it meets another flow from above.
3. Starting from a peak, the flow also stops when it comes opposite a more positive peak than that from which it started. Starting from a valley, the flow stops when it comes opposite a more negative valley than that from which it started.

It should be noted that having performed this procedure there could be half-cycles without any pair, see Figure 5.3.2. These cycles are called residual half-cycles and they can not be included in the calculation of the fatigue damage by rainflow counting. Fortunately, their effect on the results is not significant and therefore may be neglected (As & Berge, 2017).

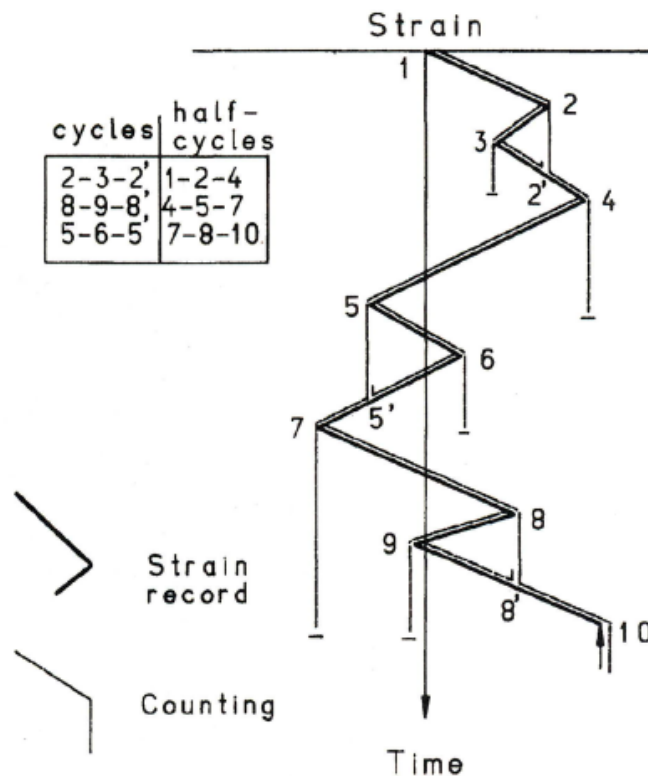


Figure 5.3.2: Illustration of Pagoda Roof Rainflow Analogy (As & Berge, 2017)

5.4 Response Analysis of Dynamic Power Cables

Dynamic power cables exhibit dynamic behavior under the effect of various loading such as wave, current and loading due to the motion of the support structure. Being the topic of this project, VIV must be taken into consideration in the global dynamic response of the structure. Although, linear modelling of above mentioned loading cases are common in the industry, a time domain model is more convenient in order to include non-linearities, especially with respect to VIV. A non-linear model is necessary to investigate non-linear effects such as varying tension along the cable, changing boundary conditions due to soil-cable interaction and large response amplitudes because of drag amplification.

Damping created by bending hysteresis regarding to VIV should also be included in the dynamic response analysis. Common practice is to implement an equivalent viscous damping model with the use of linear beam elements. This type of damping varies with respect to response amplitude, hence a proper damping coefficient for each loading case should be specified. Since the time domain analysis is of interest, a phenomenon called stick-slip condition is to be explained to have a better understanding of the damping coefficient calculation. Stick-slip condition is derived from the relation between friction moment which occurs between layers, and the curvature, see Figure 5.4.1.

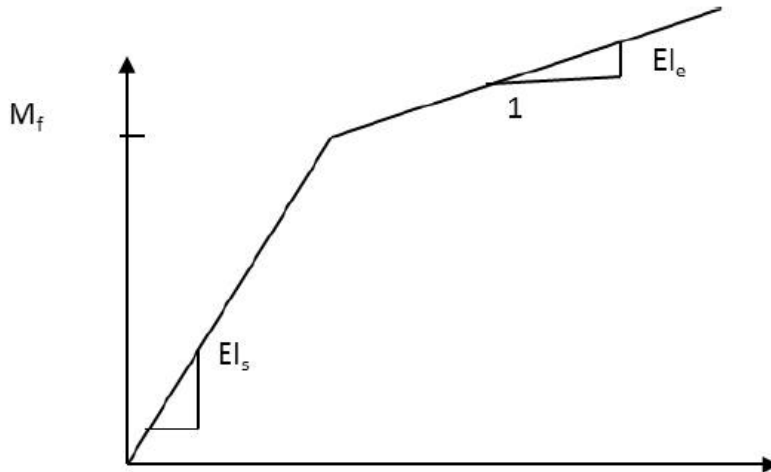


Figure 5.4.1: Relation between moment and curvature for a dynamic power cable (Sævik, 2019a)

Until M_f is reached, stick condition dominates with a small curvature and high bending stiffness EI_s . When contact pressure between layers increase and at a certain level M_f is exceeded, a linear relation between moment and curvature is obtained. As it can be seen the bending stiffness EI_e is much lower than the EI_s . It means when going above M_f limit, layers are free to slip. Therefore, by using one linear model for each of these two regions, equivalent damping coefficient can be found.

Moreover, contribution of wave forces to fatigue damage is evaluated first by extracting tension and curvature values from global analysis. These results are to be transformed into stress time series for local analysis. Local stresses are used to compute total fatigue damage accumulation by Miner sum.

Chapter 6

CASE SCENARIO

A case scenario should be presented to identify possible problems that structure may face during the design life because of the presence of VIV. Especially, special attention must be given to the fatigue damage due to VIV. In the present case scenario, both in line and cross-flow VIV are applied to the system. A global model of the structure with proper mechanical properties needs to be constructed to monitor the effect of VIV. In addition, environmental condition at the location where the wind turbine will be operating, must be taken into consideration. Then the non-linear time domain analyses of the structure could be performed by the software SIMLA.

In the current case scenario, a water depth of 100 m is defined with the hang off point at the spar bottom which is located 10 meter below mean water level. A lazy wave configuration of the power cable which has a total length of 200 m is assumed. Following Figure 6.0.1 illustrates the case scenario.

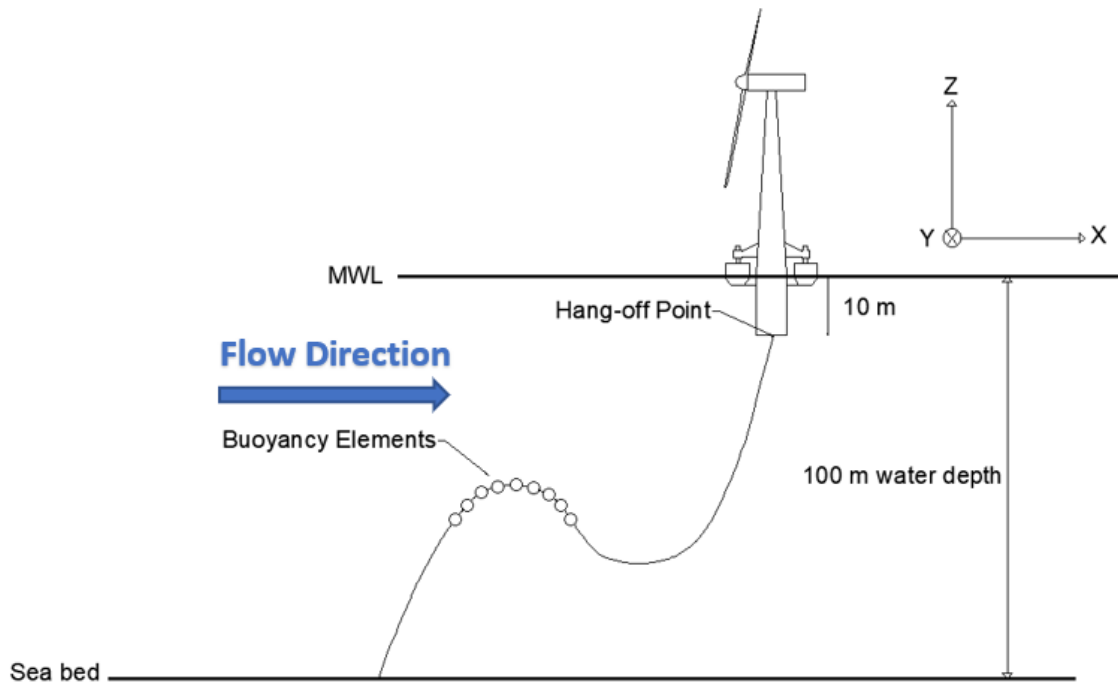


Figure 6.0.1: Lazy-wave configuration of the power cable

6.1 Mechanical Properties

Mechanical properties may be grouped in two different category namely the mechanical properties of power cable components and the mechanical properties of buoyancy elements.

6.1.1 Power Cable Cross Section

For this thesis, cross-section that is suggested by Leroy et al. (2017) is implemented. Cable's cross section is formed by 3 copper conductor which are surrounded by XLPE for the insulation. Around the XLPE, polyethylene (PE) core sheaths are attached. Moreover, PVC fillers are used to support copper conductors with the binder tapes made of PE. The region which covers components mentioned so far, will be called 'centre body' for further analysis. In order to carry the axial loads, the perimeter of the centre body is covered with two layers of steel armour wires with a polyamide (PA) separator tape between them. Whole cross section is enclosed with a PE external sheath (Leroy et al., 2017). In the Figure 6.1.1 the illustration of the cable

cross section is shown.

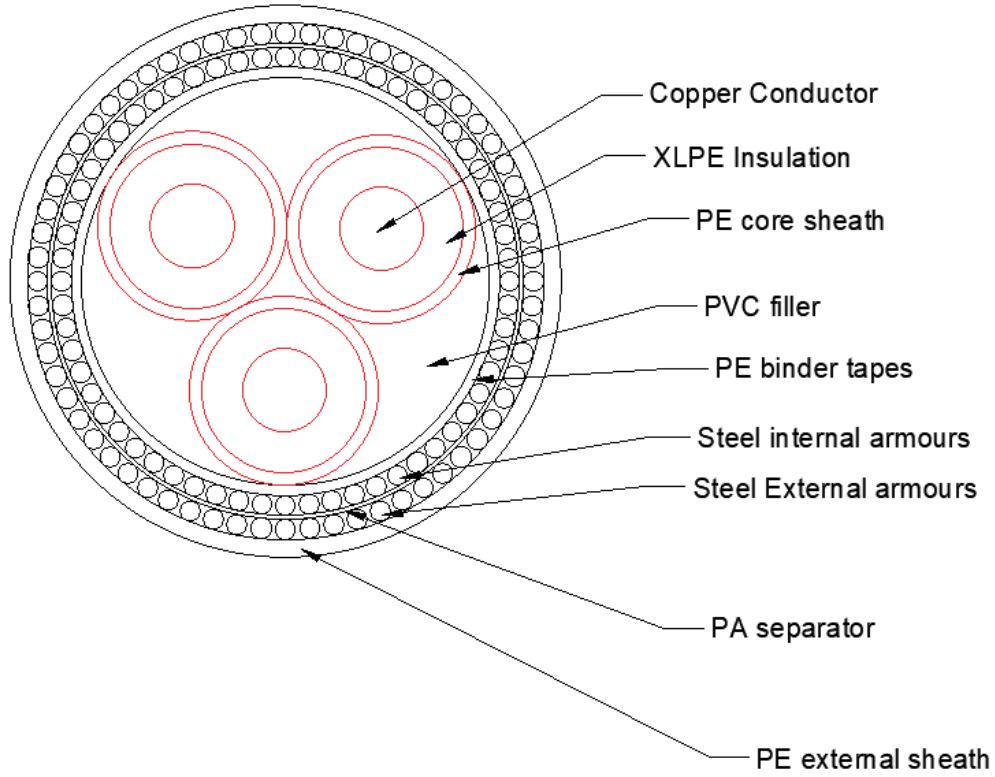


Figure 6.1.1: Power Cable Cross Section

Furthermore, material properties of the cable components can be seen in the Table 6.1.1.

Material	#	$\alpha(^{\circ})$	$R_i(mm)$	$t(mm)$	$R_o(mm)$	$\rho(kg/m^3)$	$E(MPa)$	ν
Copper	3	-	15.25	0.25	15.5	8920	12000	0.33
XLPE	3	-	7.25	8	15.25	923	100	0.2
PE_c	3	-	15.5	2.5	18	930	750	0.4
PVC	3	-	-	8.76	8.76	1350	3000	0.4
PE_{bt}	1	-	40.78	2	42.78	930	750	0.4
$Armour_i$	61	10	-	4	2	7800	210000	0.3
PA	1	-	46.78	0.8	47.58	1120	350	0.4
$Armour_o$	68	9.9	-	4	2	7800	210000	0.3
PE_o	1	-	51.58	3.5	55.08	930	750	0.4

Table 6.1.1: Material Properties of Cable Components (Leroy et al., 2017)

Where α , R_i , t , R_o and ν are the laying angle, the inner radius, the thickness, the outer radius and the Poisson's ratio, respectively.

6.1.2 Buoyancy Elements

Buoyancy elements should be designed very carefully since they ensure that the cable systems would be operating in the desired configuration. Net buoyancy and other mechanical properties of the buoyancy elements are listed in Table 6.1.2.

Total Length of buoyancy section	86.67 m
Structure Radius	0.0015 m
Wall thickness	0.0015 m
Outer Diameter	0.5 m
Density	500 kg/m ³
Dry Mass	60 kg
Submerged Mass	60 kg
Axial Stiffness	10 ⁷ N
Bending Stiffness (in both y and z directions)	0 Nm ²
Torsion Stiffness	0 N
Young Modulus	2×10 ¹¹ MPa
Shear Modulus	8×10 ¹⁰ MPa

Table 6.1.2: Buoyancy Elements' Characteristics

The relation between the dry mass m_d and the submerged mass m_s is given as:

$$m_d - B = m_s \quad (6.1.1)$$

where the buoyancy B can be calculated by Equation

$$B = \frac{\pi}{4} (D_o^2 - D_i^2) (\rho_w - \rho_b) \quad (6.1.2)$$

where the inner diameter, the outer diameter, the density of the water and the density of the buoyancy element are respectively denoted as D_o , D_i , ρ_w , ρ_b . Moreover, 260 buoyancy elements is applied with uniform spacing between them and lumped into the same node system. Spacing is set equal to one element length in the global model. It should be noted that buoyancy elements

has zero bending and torsion stiffness. It means they do not contribute to the bending and torsion stiffness of the power cable.

6.2 Environmental Data

The structure will be operating under various environmental conditions. Environmental data which possess the information about these conditions are based on the Lifes50+ project. The Lifes50+ project aims to obtain an optimized design for a wind turbine of 10 MW with different floater approaches. Design process is handled for water depths deeper than 50 m (Lifes50+, 2015).

Although three different location is considered for this project, the environmental data for West of Barra is preferred to be used as severe environmental conditions present there. Thus, it can help to specify upper bound limit for the design parameters.

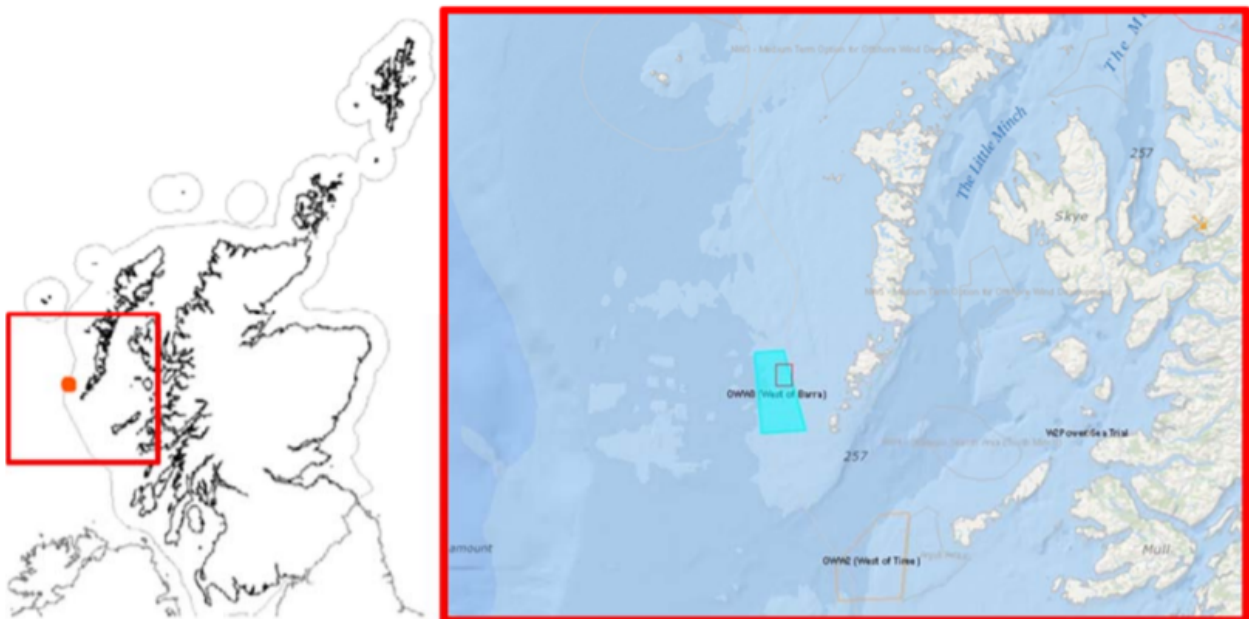


Figure 6.2.1: West of Barra Site Location (Lifes50+, 2015)

6.2.1 Wind Climate

Lifes50+ (2015) provides wind speed profiles for operational and extreme conditions by using DNV class rules. DNV (DNV, 2014) proposes a logarithmic and power low wind speed profiles for operational and extreme conditions, respectively.

$$A(z) = A(H) \frac{\ln(z/z_0)}{\ln(H/z_0)} \quad (6.2.1)$$

Where $A(z)$ refers to the logarithmic wind speed profile. On the other hand, z , z_0 and H are the height of the wind profile above the free surface, roughness parameter and height of the wind turbine hub. Then, a relation between scale parameters $A(z)$ and $A(H)$ is reached. In Table 6.2.1 the wind speed profile for operational conditions at the West of Barra location is listed.

Height [m]	Speed [m/s]
10	9.5
20	10.16
50	10.97
100	11.58
119	11.74

Table 6.2.1: Wind Speed Profile for Operational Conditions (Lifes50+, 2015)

Furthermore, the power law is applied to find wind speed profile for extreme weather conditions.

$$u(z) = U_{10}(H) \left(\frac{z}{H} \right)^\alpha \quad (6.2.2)$$

Where $U_{10}(H)$ is the mean wind speed during 10 minutes period at the wind turbine hub height. In addition α is taken as 0.12. The wind speed profile for extreme conditions is given in Table 6.2.2

Height [m]	Speed [m/s]
10	26.47
20	35.63
50	44.13
100	48.97
119	50

Table 6.2.2: Wind Speed Profile for Extreme Conditions (Lifes50+, 2015)

6.2.2 Wave Climate

The wave climate can be defined in terms of significant wave height H_s and peak period T_p . These two parameters with the wind speed at the hub height to represent the sea state are given in Table 6.2.2. Note that each sea state on the Table 6.2.2 represents a different case.

Case #	H_s [m]	T_p [s]	U_{hub} [m/s]	Occurrence Probability[%]
1	1.38	7	5	13.79
2	1.67	8	7.1	23.96
3	2.2	8	10.3	25.65
4	3.04	9.50	13.9	20.48
5	4.29	10	17.9	11.61
6	6.2	12.5	22.1	3.76
7	8.31	14	25	0.75

Table 6.2.3: Sea State (Lifes50+, 2015)

In further analysis, the sea state will be represented by a three parameter JONSWAP spectrum which can be given as (Sævik et al., 2019):

$$S(\omega) = \frac{\alpha g^2}{\omega^5} e^{\beta(\frac{\omega_p}{\omega})^4} \gamma^r \quad (6.2.3)$$

where

$$\begin{aligned} \omega_p &= \frac{2\pi}{T_p} \\ r &= e^{-\frac{(\omega-\omega_p)^2}{2\sigma^2\omega_p^2}} \\ \gamma &= e^{5.75-1.15\frac{T_p}{\sqrt{H_s}}} \\ \beta &= 1.205 \\ \alpha &= 1.2905 \frac{H_s^2}{T_z^2} \\ \sigma &= \begin{cases} 0.07 & \text{for } \omega \leq \omega_p \\ 0.09 & \text{for } \omega \geq \omega_p \end{cases} \\ T_z &= \frac{T_p}{1.407(1 - 0.287 \ln \gamma)^{0.25}} \end{aligned} \quad (6.2.4)$$

Figure 6.2.2 illustrates the JONSWAP spectra of the sea state in Table 6.2.3.

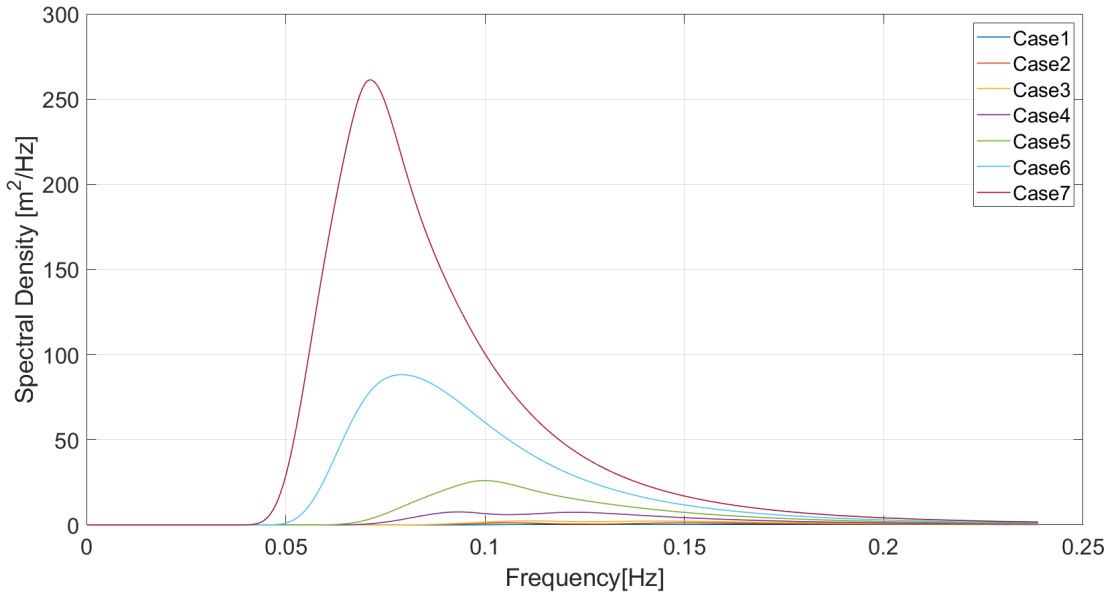


Figure 6.2.2: JONSWAP Spectrum of the sea state

6.2.3 Current

DNV (DNV, 2014) defines the total current speed profile as a combination of tidal and wind induced currents.

$$v(z) = v_{tide}(z) + v_{wind}(z) \quad (6.2.5)$$

where for $z \leq 0$

$$v_{tide} = v_{tide0} \left(\frac{h+z}{h} \right)^{1/7} \quad (6.2.6)$$

and for $-h_0 \leq z \leq 0$

$$v_{wind}(z) = v_{wind0} \left(\frac{h_0+z}{h_0} \right) \quad (6.2.7)$$

Where, h and h_0 represent water depth which is taken to be positive and reference depth of 50 m, respectively. In addition, current profiles at still water level are given as v_{wind0} for wind induced current and as v_{tide0} for tidal current. For the z parameter refer to Equation 6.2.1. Following formula by DNV (DNV, 2014) is given for the estimation of v_{wind0}

$$v_{wind0} = cU_0 \quad (6.2.8)$$

Here c is a constant between 0.015 and 0.03. Meanwhile, U_0 refers to mean wind speed during 1 hour period at 10 m height. In Lifes50+ project (Lifes50+, 2015), v_{wind0} is found as 0.881 m/s for 1 year of return period. Then, this value can be substituted into Equation 6.2.7 to calculate wind induced current for different z coordinates. In Table 6.2.4, combined current-wind profile for 1 year of return period can be seen.

Depth [m]	Wind Induced Current	Tidal-Surge Current	Total Current
	$V_c[m/s]$	$V_c[m/s]$	$V_c[m/s]$
0	0.881	1.023	1.570
-10	0.705	1.008	1.421
-20	0.528	0.992	1.279
-30	0.352	0.973	1.147
-40	0.176	0.952	1.029
-50	0.000	1.051	0.928
-60	0.000	1.018	0.900
-70	0.000	0.978	0.864
-80	0.000	0.924	0.817
-90	0.000	0.839	0.741
-100	0.000	0.000	0.000

Table 6.2.4: Current profile for 1 year of return period (Lifes50+, 2015)

Furthermore, in order to create the current profiles for each cases described in Table 6.2.2, a two parameter Weibull distribution is used to calculate the probability density function from the total current speed profile (v) for 1 years of return period, see Table 6.2.4.

$$f(v) = \frac{k}{\lambda} \left(\frac{v}{\lambda}\right)^{k-1} \exp\left(-\frac{v}{\lambda}\right)^k \quad (6.2.9)$$

The selection for the shape parameter k and the scale parameter λ for the distribution can be seen in Table 6.2.5. The Weibull distribution and the corresponding distribution of the current speeds' occurrence probability is shown in Figure 6.2.3. Probability distribution of the current speeds are found simply by multiplying each current speed with its probability density.

λ	k
0.45	1.90

Table 6.2.5: Parameters for Weibull's Distribution

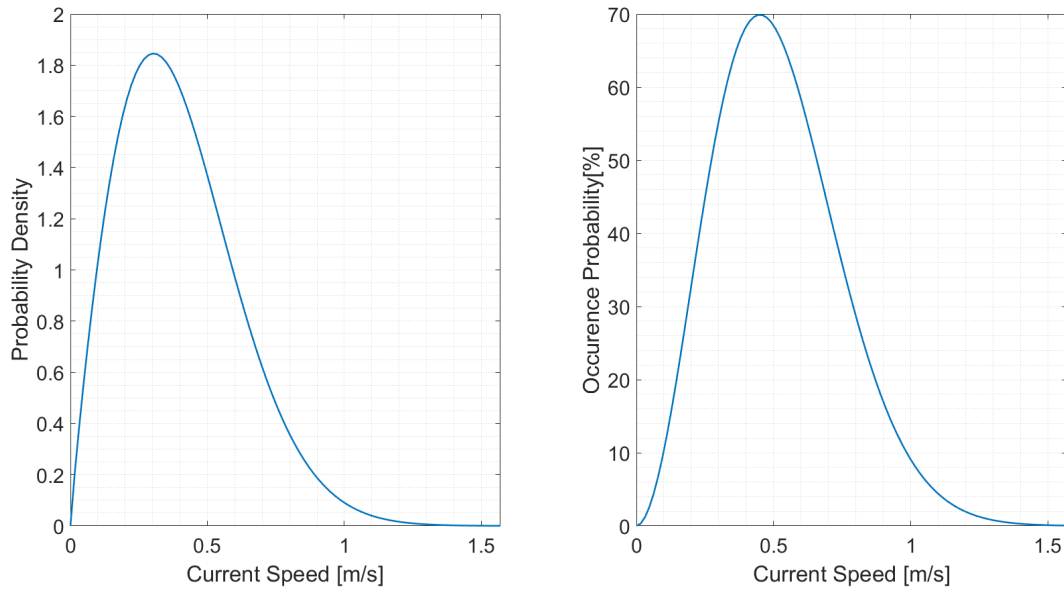


Figure 6.2.3: Probability densities and occurrence probabilities for current speeds

Moreover, for the occurrence probability for each sea state in Table 6.2.2, corresponding maximum current speed is found in the Weibull distribution. This value is considered as the current speed at the mean water level and used to form a current profile for each case. Also, it should be noted that the current and the wave loading are always acting on the structure in the direction of 0° , see Figure 6.0.1. The current data for each case is tabulated in Table 6.2.6.

Case # Depth [m]	Current Speed[m/s]						
	1	2	3	4	5	6	7
0	0.9515	0.8405	0.8088	0.8722	0.9614	1.1418	1.2687
-10	0.8564	0.7565	0.7279	0.7850	0.8653	1.0276	1.1418
-20	0.7612	0.6724	0.6470	0.6978	0.7691	0.9134	1.0150
-30	0.6661	0.5883	0.5662	0.6105	0.6730	0.7993	0.8881
-40	0.5709	0.5043	0.4853	0.5233	0.5768	0.6851	0.7612
-50	0.4758	0.4203	0.4044	0.4361	0.4807	0.5709	0.6344
-60	0.3806	0.3362	0.3235	0.3489	0.3846	0.4567	0.5075
-70	0.2855	0.2522	0.2426	0.2617	0.2884	0.3425	0.3806
-80	0.1903	0.1681	0.1618	0.1744	0.1923	0.2284	0.2537
-90	0.0952	0.0841	0.0809	0.0872	0.0961	0.1142	0.1269
-100	0.000	0.000	0.000	0.000	0.000	0.000	0.000

Table 6.2.6: Current Profiles for each cases

6.3 Floater Motions

Floater motions are based on 10MW wind turbine OO-Star from Lifes50+ project (2015). For each case only surge, sway and heave motions or in other words translation motions are considered. The reason for that is the hang off point is modelled as a hinged connection, see Section 7.2. Thus, no moment will be created since the structure rotates in the hang off point freely. The variation of floater motions as a function of time can be seen in Appendix A.

6.4 Fatigue Data

In this study the fatigue life of the copper conductor of the power cable will be evaluated based on the S-N curves proposed by Nasution et al. (2014), see Figure 6.4.1. Black curve which is used for further fatigue analysis is formed by scatter bands (red curves) plus/minus two standard deviations (Nasution et al., 2014). Recalling Equation 5.2.2 the fatigue parameters for the black curve became $m = 6.238$ and $A = 6.098 \times 10^{19}$.

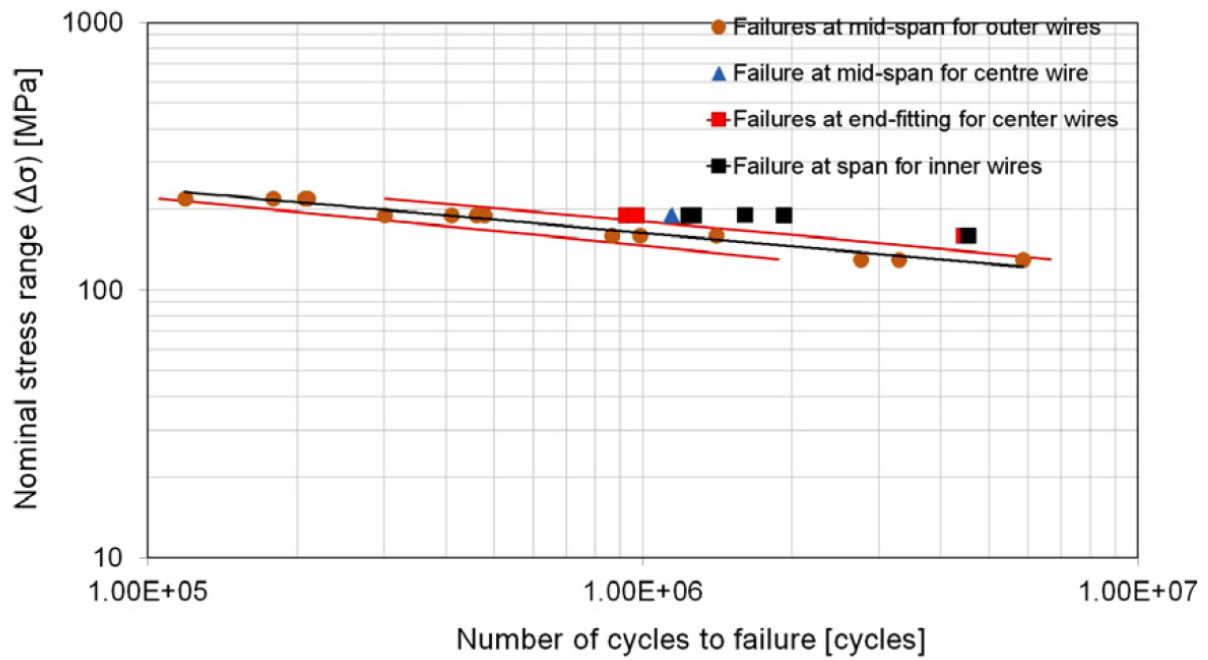


Figure 6.4.1: S-N curves to be used in the fatigue calculations (Nasution et al., 2014)

On the other hand, the fatigue life of the steel armour layers will be calculated based on the SN data of the offshore steel structures proposed by DNVGL(2014). Thus, for further steps in the determination of the steel armours' fatigue life, $A = 10^{15.177}$ and $m = 4$ are chosen.

Chapter 7

MODELLING PROCEDURE

7.1 Local Model

A local FE model needs to be introduced for calculating the axial, bending and the torsion stiffness of the cable to be used in the global FE model. In addition, the fatigue life of the power cable will be calculated by performing rainflow counting of the stress time series resulted by applying dynamic loading that is computed by the global model. Thus, a convenient local FE model is indispensable to reach an accurate result of the fatigue life. The local model that is implemented for this thesis work is built by assuming periodic boundary conditions with constant curvature in space. Besides, the contact pressure and the friction effects due to the interaction of the cable components are also included in order to achieve a realistic model (Leroy et al., 2017).

7.1.1 Cable Cross Section

Cross-section properties that is implemented for the local model is explained in detail in the Section 6.1.1.

7.1.2 Element Properties for FE Model in BFLEX

Local FE model is formed of 2 main parts; structural layers and contact layers. Three types of elements from Bflex catalogue are used to model these layers namely HSHEAR353, HSHEAR363 and HCONT463. While HSHEAR363 is used to model external sheath, PA separator and centre body which includes copper conductors, XLPE insulation, PE core sheath, PVC fillers

and PE binder tapes, HSHEAR353 is used to model the armour layers. On the other hand, the contact surfaces between the structural layers are modelled with HCONT463. Figure 7.1.1 shows a simple representation of how these elements are connected to each other.

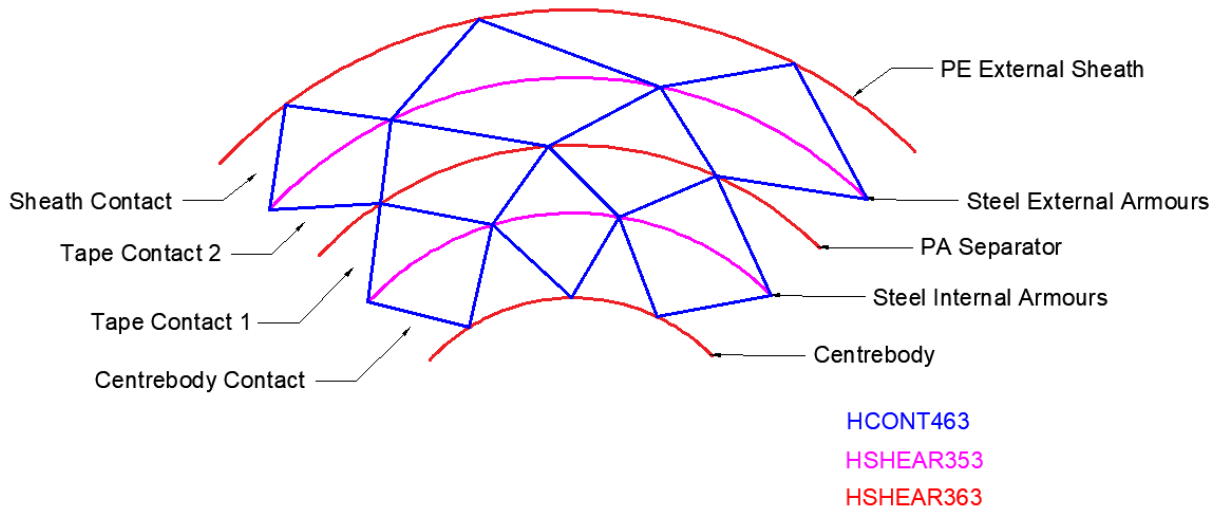


Figure 7.1.1: Organisation of Local Model in Bflex

Therefore, some theory should be given about these elements in order to understand how the local model works.

- **HSHEAR 353**

Unlike an ordinary beam element, HSHEAR353 possess 4 nodes. The mission of the additional 2 nodes is to neglect shear deformations across the section by defining the motion by standard beam quantities. The element has 26 degrees of freedom (Dofs) in total 12 being related to global strain quantities and the other 14 representing the local displacement of the wire relative to the core (Sævik, 2019b), see Figure 7.1.2.

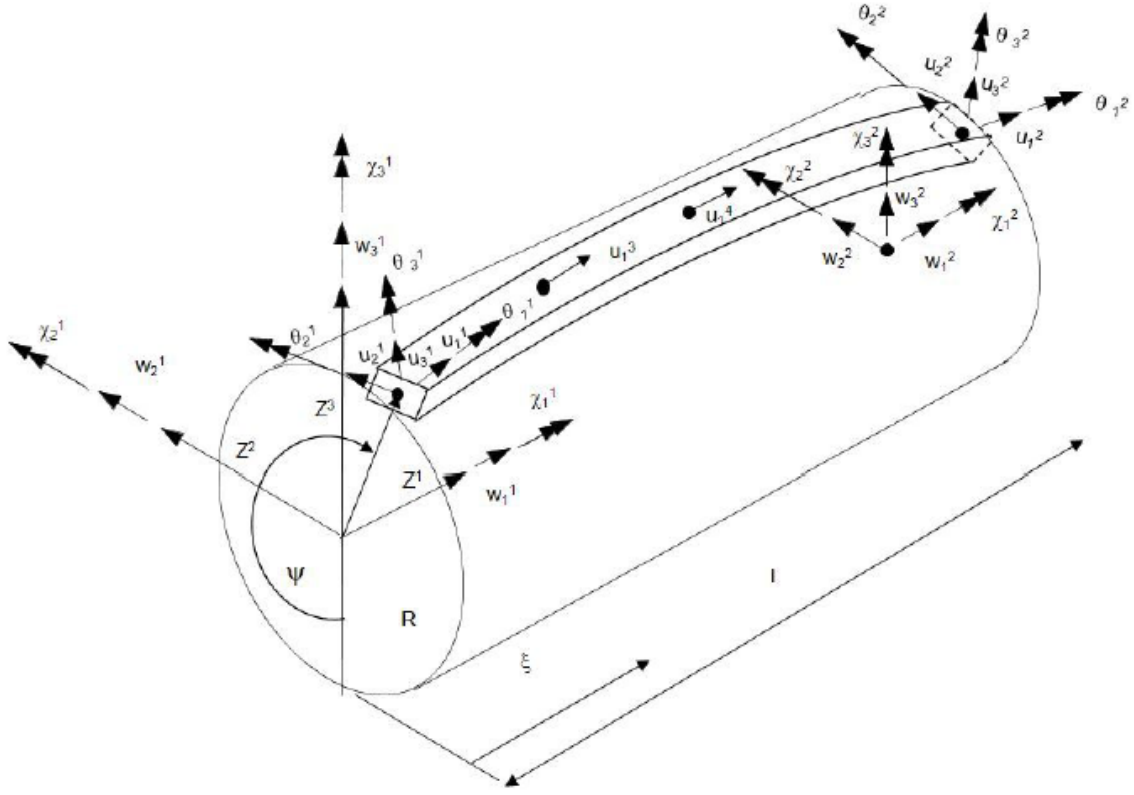


Figure 7.1.2: Representation of Hshear353 Dofs (Sævik, 2019b)

The structure of HSHEAR353 makes it possible to perform cubic interpolation in all directions and prevents membrane locking resulted by the curvature coupling term. It should be also noted that the kinematic constraints are applied to the torsion Dof. Therefore, it is not active and must be suppressed. Moreover, the strains and the rotations could be written as follows

$$\epsilon_1 = u_{1,1} - \kappa_3 u_2 + \kappa_2 u_3 \quad (7.1.1)$$

$$\epsilon_2 = u_{2,1} + \kappa_3 u_1 - \kappa_1 u_3 \quad (7.1.2)$$

$$\epsilon_3 = u_{3,1} - \kappa_2 u_1 + \kappa_1 u_2 \quad (7.1.3)$$

$$\omega_1 = \kappa_1 u_{1,1} - \kappa_t u_{2,1} + \kappa_3 (u_{3,1} + \kappa_1 u_2) + \kappa_2 (u_{2,1} - \kappa_1 u_3) + \omega_{1p} \quad (7.1.4)$$

$$\omega_2 = -u_{3,11} + \kappa_2 u_{1,1} - 2\kappa_1 u_{2,1} - \kappa_3 \kappa_t u_2 + \kappa_1 \kappa_1 u_3 + \omega_{2p} \quad (7.1.5)$$

$$\omega_3 = u_{2,11} + \kappa_3 u_{1,1} - 2\kappa_1 u_{3,1} + \kappa_2 \kappa_t u_2 - \kappa_1 \kappa_1 u_2 + \omega_{3p} \quad (7.1.6)$$

Where the transverse curvature κ_t can be calculated as:

$$\kappa_t = \frac{\cos^2 \alpha}{R} + \sin^2 \alpha \left(\frac{-\omega_{2,11} \sin \psi}{1 - R\omega_{2,11} \sin \psi} + \frac{\omega_{3,11} \cos \psi}{1 + R\omega_{3,11} \cos \psi} \right) \quad (7.1.7)$$

Here, $u_{i,j}$ stands for the differentiation of the displacement components u_i along the X^i axis with respect to curve linear coordinate X^j . Moreover, the axial strain, the center line rotation about the X^3 axis, the center line rotation about the X^2 axis, the center line torsion, the curvature about the X^2 axis, the curvature about the X^3 axis are described by ϵ_1 , ϵ_2 , ϵ_3 , ω_i , ω_2 and ω_3 , respectively. Lastly, while the bending caused torsion and curvature is represented by ω_{ip} , κ_i refers to the initial torsion and curvature (Sævik, 2019b).

- **HSHEAR363**

While a normal beam element has 2 nodes, HSHEAR363 element possess 3 nodes. That additional node allows to consider the thin shell theory for the analysis of the plastic layers and also take into account the axisymmetric behaviour of the buckling tapes by defining the radial motion. This additional node contains 3 Dofs, however only one of them, the radial Dof, is active, see Figure 7.1.3. Thus, the others must be suppressed. HSHEAR363 element is useful to model plastic layers, pressure arms and tapes. Longitudinal strain for plastic layers, pressure arms and tapes are formulated in Equations 7.1.9, 7.1.8, 7.1.8, respectively.

$$\epsilon_{11} = \cos^2 \alpha \omega_{1,1} + \frac{\sin^2 \alpha}{R} u_3 + R \sin \alpha \cos \alpha \chi_{1,1} \quad (7.1.8)$$

$$\begin{aligned}
 \epsilon_{11} &= \omega_{11} \\
 \epsilon_{22} &= \frac{u_3}{R} \\
 \epsilon_{12} &= R\chi_{1,1}
 \end{aligned}
 \tag{7.1.9}$$

here index 1 stands for Z^1 and index 2 represents the hoop axis X^2 .

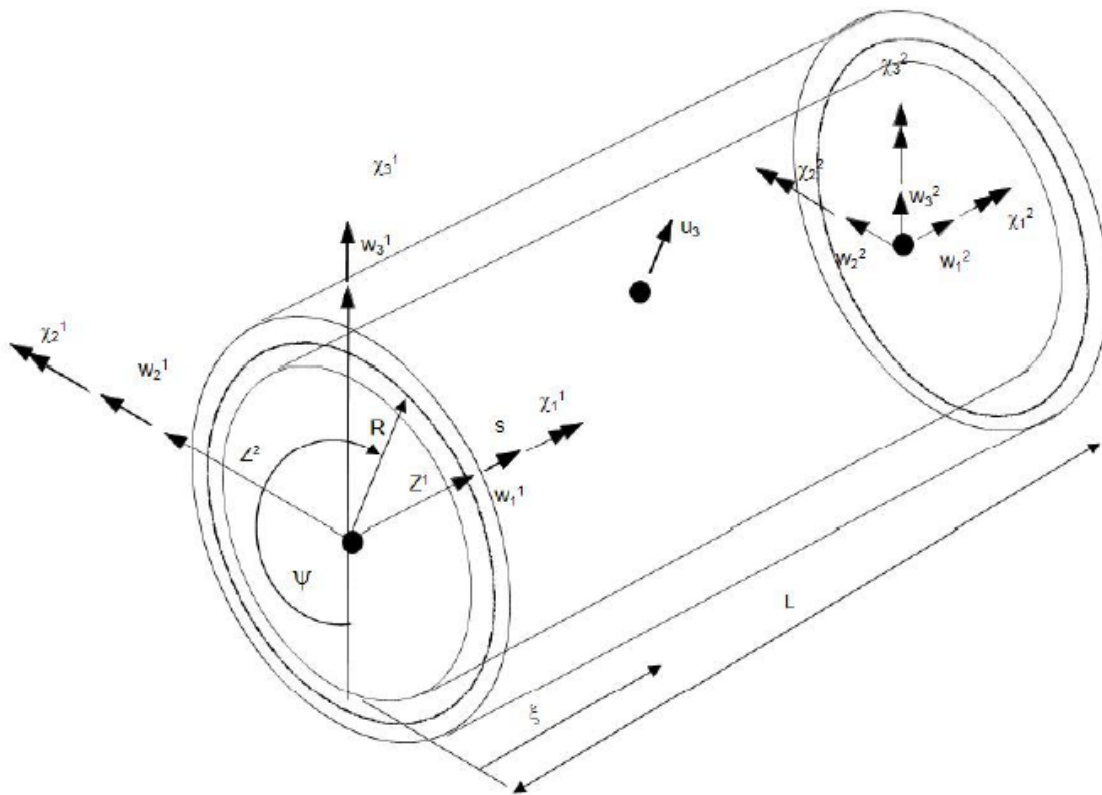


Figure 7.1.3: Representation of Hshear353 dofs (Sævik, 2019b)

- **HCONT 463**

HCONT463 is used to connect HSHEAR353 and HSHEAR363 elements. Since these two elements have different numbers of Dofs, when they are into contact, there might be some problems. HSHEAR353 element contains axial, transverse and radial displacements whereas HSHEAR363 has only radial displacement. Thus, HSHEAR353 has 10 Dofs and HSHEAR363 has 3 Dofs, see Figure 7.1.4. The total number of 13 Dofs is updated to 15

Dofs with the dummy torsion Dofs to get the standard 6 Dofs per node.

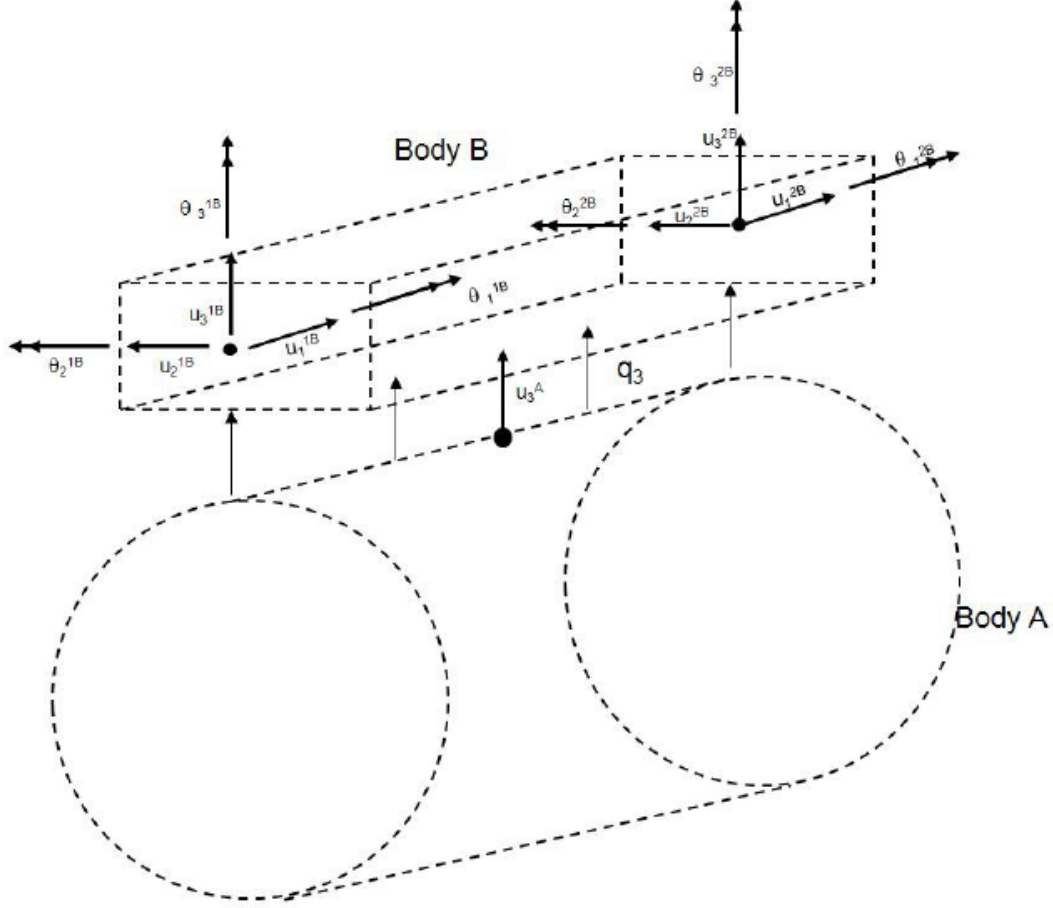


Figure 7.1.4: Representation of 13 Dofs HCONT463 Contact Element (Sævik, 2019b)

Considering two bodies A and B, the energy functional $\Delta\pi$ will be representing the terms related to these bodies and also the contact conditions.

$$\Delta\pi = \sum_{l=A}^B \Delta\bar{\pi}^l - \int_{S_c} (\lambda_n + \Delta\lambda_n) \cdot g ds - \frac{1}{2\alpha} \int_{S_c} \Delta\lambda_n^2 ds - \int_{S_c} \lambda_t \cdot \Delta\gamma ds - \frac{1}{2} \int_{S_c} \Delta\lambda_t \Delta\gamma ds \quad (7.1.10)$$

where $\Delta\bar{\pi}^l$ symbolises A and B's incremental potential. On the other hand, λ_n , λ_t and γ are respectively the contact pressure, shear stress and shear strain. The surface scaling

factor α is associated to the surface stiffness which is assumed to act elastically. Furthermore, equilibrium condition for the bodies A and B has to be fulfilled at any time instant.

$$\delta\Delta\pi = 0 \quad (7.1.11)$$

Then, by elaborating Equation 7.1.11, a weak form of contact condition is reached, see Equation 7.1.12. In order to achieve the exact contact condition scaling factor α should be $\alpha \rightarrow \infty$.

$$(\Delta\mathbf{u}_B - \Delta\mathbf{u}_A) \cdot \mathbf{n} + g_0 = \frac{\Delta\lambda_n}{\alpha} \quad (7.1.12)$$

7.1.3 Applying Periodicity Conditions for FE Model in BFLEX

Reducing the length of the FE model is very desirable for saving from the computational time. To do so, the cable geometry and all the loading acting on it are assumed to be repeating themselves over one pitch of the armour layers (Leroy et al., 2017). That way length of the model becomes dependent on the pitch of the armour layers by a relation of $2p/n$ where p and n stand for the pitch of the armour layer and the number of wires in the corresponding armour layer.

Furthermore, specifying the suitable periodic conditions is necessary. By considering the inner armour layer, nodes A_i, B_i, C_i and O can be defined, see Figure 7.1.5. It can be seen in Figure 7.1.5 that nodes A_i and B_i are located on the same line and A_i is at the symmetry plane. C_i is at the same section with B_i and also it is on the model axis. Lastly, point O is the origin of the model.

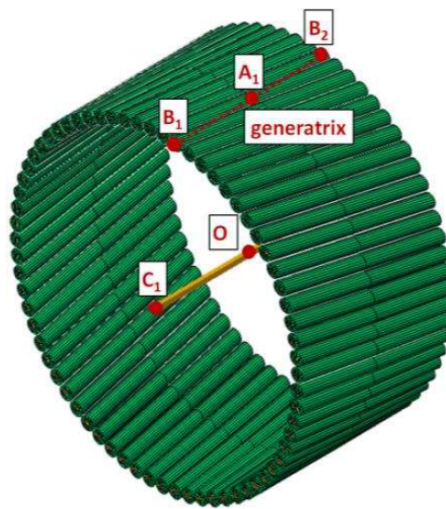


Figure 7.1.5: Nodes for periodicity conditions (Leroy et al., 2017)

If the location of these nodes after the deformation are denoted as A'_i , B'_i and C'_i , periodicity conditions for their degrees of freedom can be written as (Leroy et al., 2017):

$$\vec{x}_{B'_i} - \vec{x}_{C'_i} = \mathbf{R}(\phi_{C_i})(\vec{x}_{B_i} - \vec{x}_{C_i} + \vec{x}_{A'_i} - \vec{x}_{A_i}) \quad (7.1.13)$$

$$\vec{\phi}_{B_i} = \vec{\phi}_{C_i} \cdot \vec{\phi}_{A_i} \quad (7.1.14)$$

Here, Equation 7.1.13 and Equation 7.1.14 are respectively the periodicity conditions for translational and rotational degrees of freedom with the rotation vector $\vec{\phi}$, the position vector \vec{x} and the rotation matrix $\mathbf{R}(\phi_{C_i})$ of node C_i . Then, by the linearization of Equations 7.1.14 and 7.1.13, nodes B_i become slave dofs of the nodes A_i and C_i . That means model is simplified by removing all the nodes except the ones in the symmetry plane.

In the simplified model, the curvature value is the same for every node in the system. In addition, the axial displacement in one of the master dofs is linearly distributed among the slave nodes. Finally, it is important to set proper boundary conditions to achieve accurate results. The node at the origin is restricted in order to avoid rigid body motions. Also, layers are only allowed to slip in the longitudinal (x) direction of the global axis of the local model, see Figure 7.1.6.

7.1.4 Extracting Material Properties From The Local Model

A local analysis is required to calculate important material properties for the global model. Axial stiffness (EA), torsion stiffness (GI_t) and bending stiffness (EI) are the essential material properties to build the global model and perform a global analysis. The procedure to compute these parameters is as follows:

1. Axial tension is applied in both negative and positive x direction to calculate EA , see Figure 7.1.6 for local axis. No initial strain (ϵ) is applied.
2. A torsion moment about the x axis (MI_t) is applied to find GI_t . No initial strain is applied.
3. A bending moment about the y axis (M_y) is used to calculate EI . No initial strain is applied.
4. A bending moment about the y axis (M_y) is used to calculate EI . Initial strain is applied.

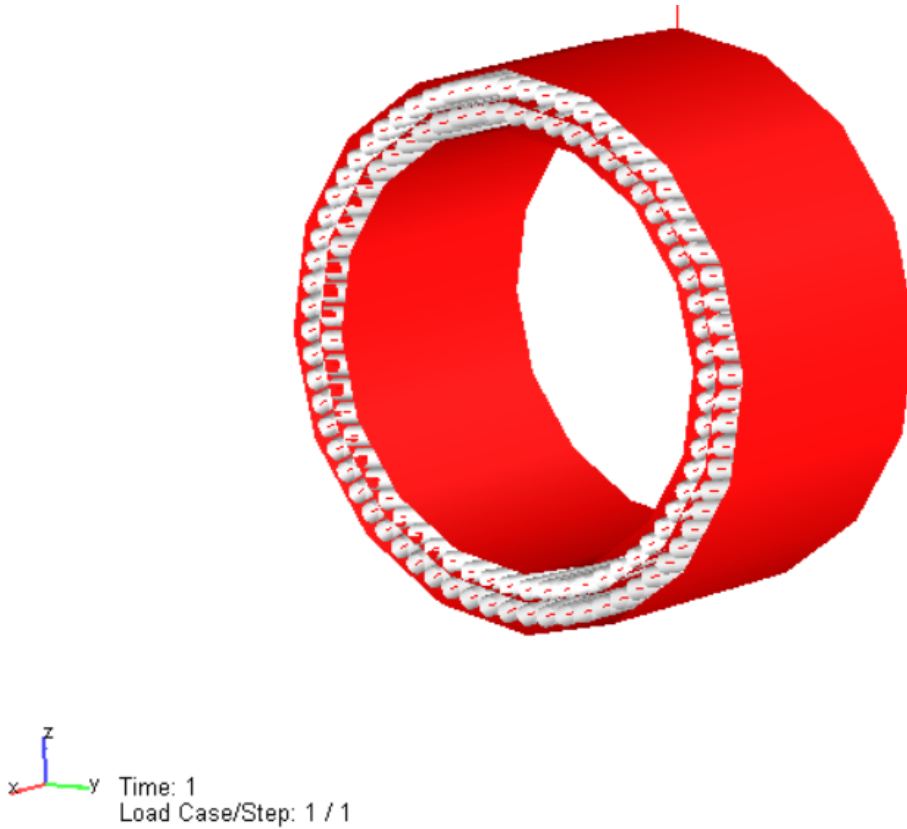


Figure 7.1.6: Local Model in Bflex

For each of these four steps, a separate simulation is performed. Besides, mentioned forces and moments are applied to the both ends of the local model in opposite directions. The force, the moment and the strain values that are used in this analysis are tabulated in Table 7.1.1 .

T_x [N]	10000
M_y [Nm]	100
M_t [Nm]	10
ϵ [-]	0.106

Table 7.1.1: Force, moment and strain values for local analysis

The nodal reactions and displacements are extracted for the inner armour layer. Then, the nodal displacements are divided by L/N to get the strain values where L is the model length equals to 1.6 m and N is the number of armour wires, see Table 6.1.1. Since, the torsion moment, the tension and the corresponding strains are known, $T_x - \epsilon$ and $MI_t - \epsilon$ curves can be drawn.

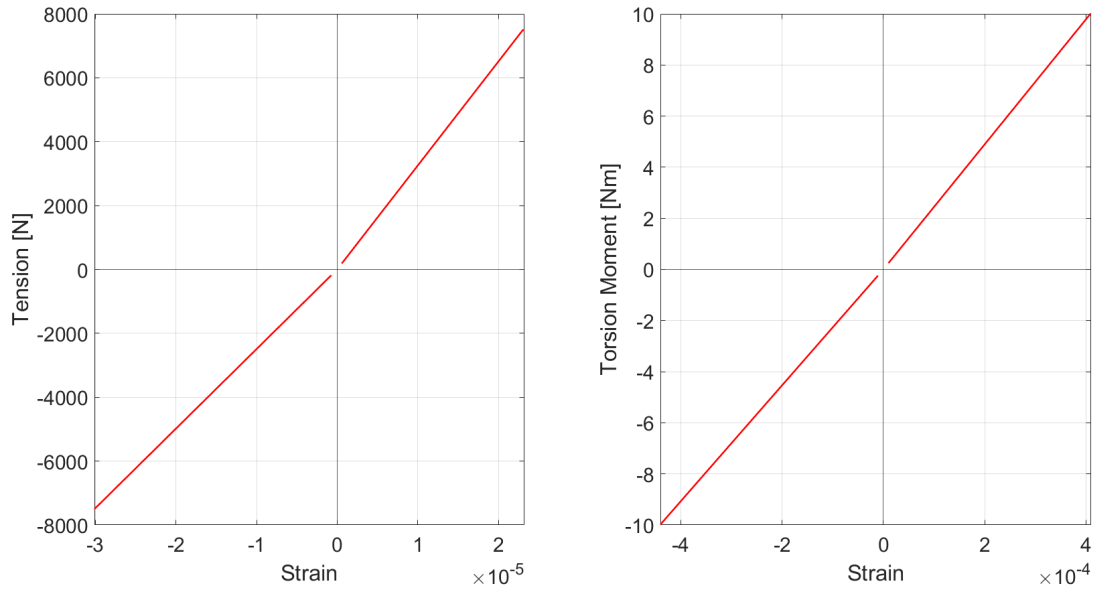


Figure 7.1.7: Variations of tension and torsion moment in the armour layer as a function of strain

Furthermore, EA and GI_t are equal to the slopes of the tension-strain and the torsion moment-strain curves in Figure 7.1.7, respectively. On the other hand, the bending moment variation in the armour layer as a function of the curvature should be established in order to find EI , see Figure 7.1.8.

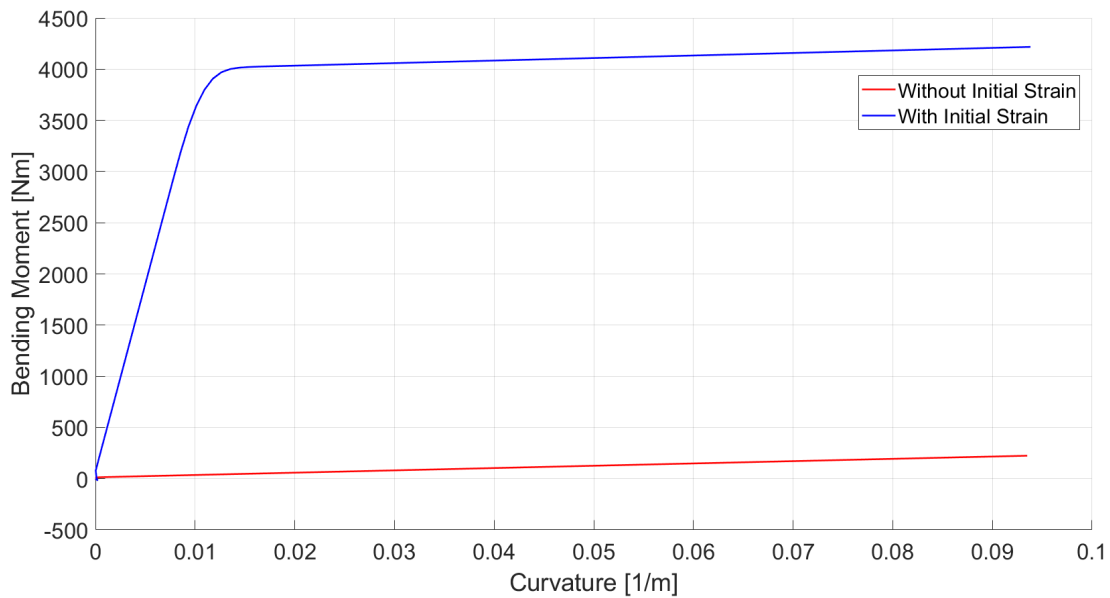


Figure 7.1.8: Variation of bending moment in the armour layer as a function of strain

As it can be seen in Figure 7.1.8, the initial strain is the governing factor for bending stiffness. Thus, recalling the Figure 5.4.1 in the Section 5.4, the elastic bending stiffness from the curve with initial strain is considered to achieve more conservative results in further analysis. Final values of the axial, bending and the torsion stiffness are tabulated in Table 7.1.2.

EI [Nm^2]	GI_t [Nm^2]	EA [N]
2481	1.7050×10^4	2.6060×10^8

Table 7.1.2: Material Properties to be used in the Global Analysis

7.2 Global Model

A global model representing the dynamic behavior of the power cable is necessary. In this thesis work, SIMLA software is used to build the global model. The aim is to extract the accumulated fatigue damage due to VIV in the hogging (buoyancy section) and sagging parts of the cable, see 7.2.1. Locations close to the hang-off point are also critical for the fatigue damage but they are not considered in this work. The reason for that is no bend stiffener is implemented to the hang-off point, hence calculated fatigue life for this section would be neither realistic nor accurate.

7.2.1 Cable Configuration

The dynamic power cable is represented by 3 parts in the global model in a lazy wave configuration, see 7.2.1. The first part (s_1) connects sea bed to the second part (s_2) which is the buoyancy section. Lastly, third part of the cable (s_3) starts from the end of the buoyancy section and attaches the whole cable system to the offshore wind turbine on the hang-off point, see Figure 7.2.1.

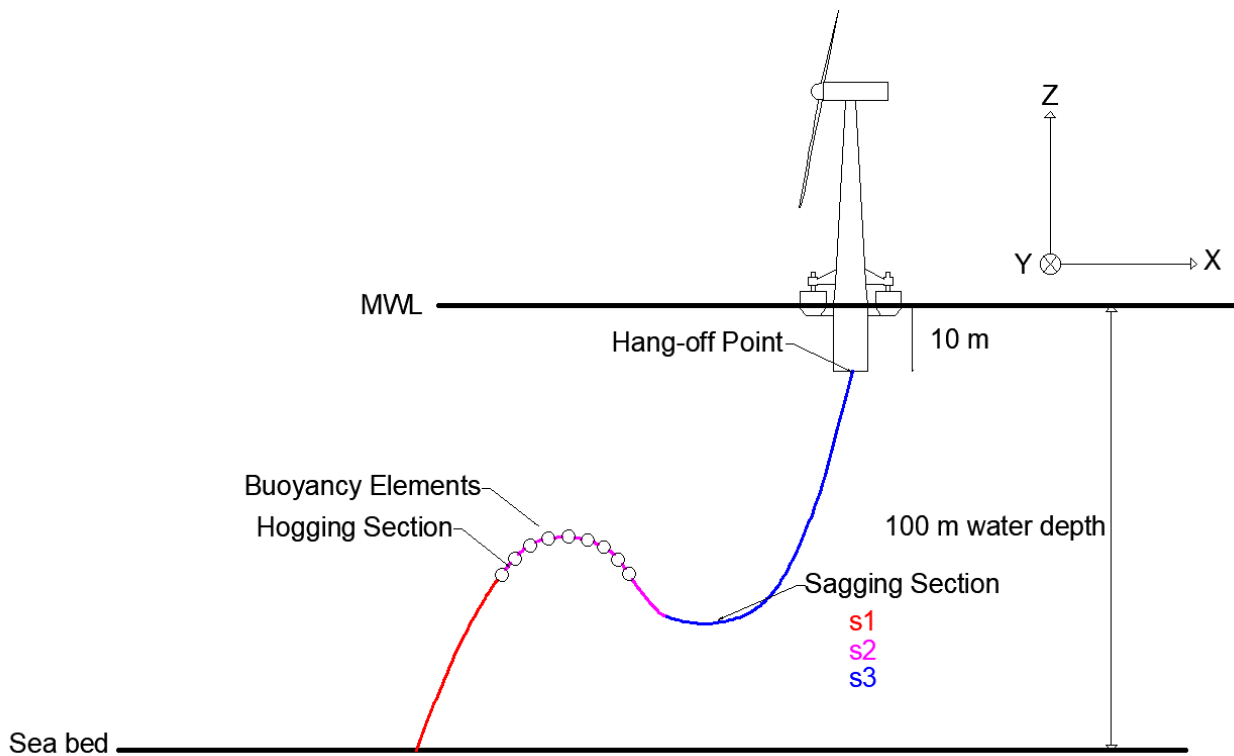


Figure 7.2.1: Parts of the Global Model

Material properties for all of these 3 sections are identical and used as tabulated in Table 7.1.2 except those for buoyancy elements which are listed in Table 6.1.2. On the other hand, the power cable has constant external area over its length, except the buoyancy section which has a larger external area due to the buoyancy elements. All other relevant parameters for the global model are listed in Table 7.2.1.

Number of elements	600
Cable Height [m]	90
Outer Diameter, s_1 [m]	0.1100
Outer Diameter, s_2 [m]	0.5000
Outer Diameter, s_3 [m]	0.1100
Length of buoyancy section, s_2 [m]	86.67
Total cable length [m]	200
Submerged mass [kg/m]	15

Table 7.2.1: Power Cable Parameters for global model

7.2.2 Boundary Conditions

Boundary conditions for the global model are applied to the last and the first node of the power cable model. In other words locations where the power cable connects the sea bed and the OWT. While for the sea bed connection only rotations about y and z axis are allowed, only translational motions are permitted in the hang-off point.

7.2.3 Validation of The Global Model

A test simulation should be performed to confirm that the global model is working. Most extreme loading case which is the case 7 shown in Table 6.2.3 with the corresponding current data in Table 6.2.6 is applied to conduct a conservative analysis. In order to validate the model certain conditions have to be met. To begin with, the maximum curvature can not exceed the value specified by API (American Petroleum Institute, 2008). API suggested a formulation to calculate minimum bend radius(MBR) which is going to be reversed afterwards to obtain the maximum allowable curvature along the cable.

$$MBR = R_{storage}\gamma \quad (7.2.1)$$

where $R_{storage}$ is ten times of the radius of the cable cross-section, see Table 5.1.1. The safety factor γ is taken as 1.5 as API recommendations stated.

Another condition to be checked is if the maximum tension in the cable is within the limits. To do so, the maximum allowable tension should be evaluated. Equation 7.2.2 was proposed by Professor Svein Sævik for that purpose:

$$T_{al} = A_s n \cos \alpha \sigma_y \quad (7.2.2)$$

where, A_s , n , α and σ_y are the cross-section area of a single armour wire, the total number of armour wires in the cable, lay angle and the yield strength of the steel, respectively. Table 7.2.2 shows the comparison of maximum curvature and tension values with limit values.

T_{al} [kN]	T_{max} [kN]	1/MBR[1/m]	κ_{max} [1/m]
399	320	0.6061	0.3360

Table 7.2.2: Comparison of maximum curvature and tension values with the limit values

Furthermore, special care should be given the buoyancy section during the test. It is not

supposed be completely straight in the far configuration and also it should not be too close to the free surface to avoid any compression.

7.2.4 Pipe Elements

Global model for the dynamic power cable consists of pipe elements. Each segment of the cable and also the buoyancy elements are formed by pipe elements. In SIMLA beam elements correspond to pipe elements considering same radius and thickness within the elements' cross sections. Since both pure inline and cross-flow VIVs present in the case scenario, PIPE31 element in SIMLA which is a linear 3D beam element is used to create global model. Along the element axial strain and torsion remain the same. This element has 2 nodes with 6 dof in each node. Motion of the nodes are defined in global coordinates with the base vector \mathbf{I}_i . Whereas, deformations are to be evaluated in local level j_i . In order to get accurate results for deformations, rigid body motions need to be removed by applying ghost reference formulation as indicated in Figure 7.2.2 (Sævik, 2017).

In case of large displacements exist in a system, translational displacement components are to be considered. Because of that rigid body modes are eliminated by defining rotational motion in each node with an orthonormal base vector triad \mathbf{i}_i^n . Where n shows which configuration is it and the triad is referred to the global system triad by the relation (Sævik, 2017):

$$\mathbf{i}_i = \mathbf{T}_{ij}^n \mathbf{I}_j \quad (7.2.3)$$

During the deformation, nodal system \mathbf{i}_i and element system \mathbf{j}_i displace together with the nodes and they are parallel to base vectors \mathbf{I}_i in the initial configuration (Sævik, 2017).

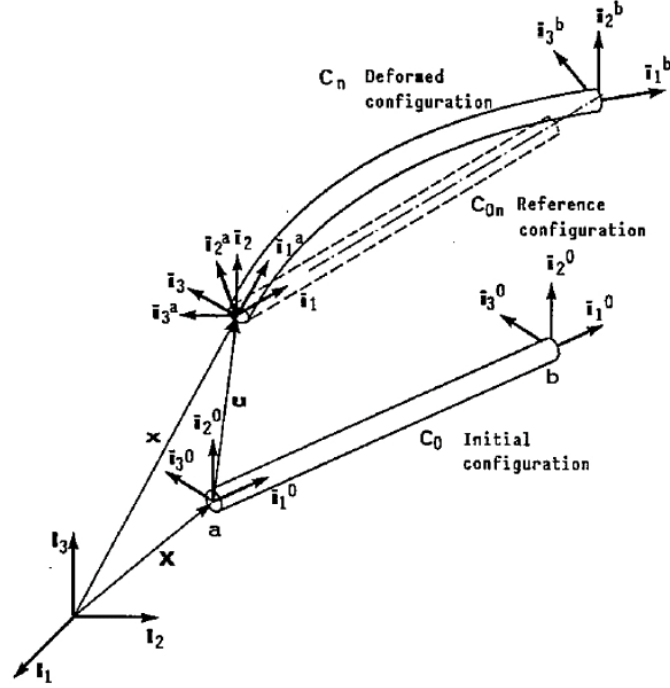


Figure 7.2.2: Ghost reference formulation by Mathisen(1990) for motion of the nodes (Sævik, 2017)

7.2.5 Global Load Model in SIMLA

In the global model, considered loading are generally caused by structure's own weight and the inertia. A global mass matrix should be established to represent the loading due to weight of each element by using interpolation functions. Having calculated the mass of each element, a diagonal global mass matrix can be defined with the weight of each element on the diagonals. For the external loads caused by waves, Morison equation should be applied to find hydrodynamic loading on each element. Then, total hydrodynamic loading on the global model can be reached. Sævik (Sævik, 2017) explains how SIMLA computes hydrodynamic loads by given tangential added mass coefficient ($C_{m,t}$), normal added mass coefficient ($C_{m,n}$), tangential drag coefficient ($C_{d,t}$), normal drag coefficient ($C_{d,n}$), body displacements (u) and hydrodynamic particle displacements (ω):

$$\rho \frac{\pi}{4} D^2 C_{m,t} \ddot{u}_y = \frac{1}{2} \rho C_{d,t} \sqrt{(\dot{\omega}_x - \dot{u}_x)^2} (\dot{\omega}_x - \dot{u}_x) \quad (7.2.4)$$

$$\rho \frac{\pi}{4} D^2 (C_{m,n} - 1) \ddot{u}_y = \rho \frac{\pi}{4} D^2 \ddot{\omega}_y + \frac{1}{2} \rho C_{d,n} \sqrt{(\dot{\omega}_y - \dot{u}_y)^2 + (\dot{\omega}_z - \dot{u}_z)^2} (\dot{\omega}_y - \dot{u}_y) \quad (7.2.5)$$

$$\rho \frac{\pi}{4} D^2 (C_{m,n} - 1) \ddot{u}_z = \rho \frac{\pi}{4} D^2 \ddot{w}_z + \frac{1}{2} \rho C_{d,n} \sqrt{(\dot{w}_y - \dot{u}_y)^2 + (\dot{w}_z - \dot{u}_z)^2} (\dot{w}_z - \dot{u}_z) \quad (7.2.6)$$

It should be noted that, other than wave loads, external load vector for the global model also includes buoyancy, external pressure and current loads. In terms of the damping loads, global damping matrix is a combination of a diagonal lumped matrix C_0 and Rayleigh damping matrix as follows

$$C = C_0 + M\alpha_1 + K\alpha_2 \quad (7.2.7)$$

Where α_1 and α_2 are constants.

Chapter 8

ANALYSIS METHODOLOGY

In this chapter, the procedure that is followed to estimate the fatigue life will be elaborated. As mentioned before, the hogging and the sagging sections of the power cable will be subjected to this analysis procedure which is summarized in Figure 8.0.1.

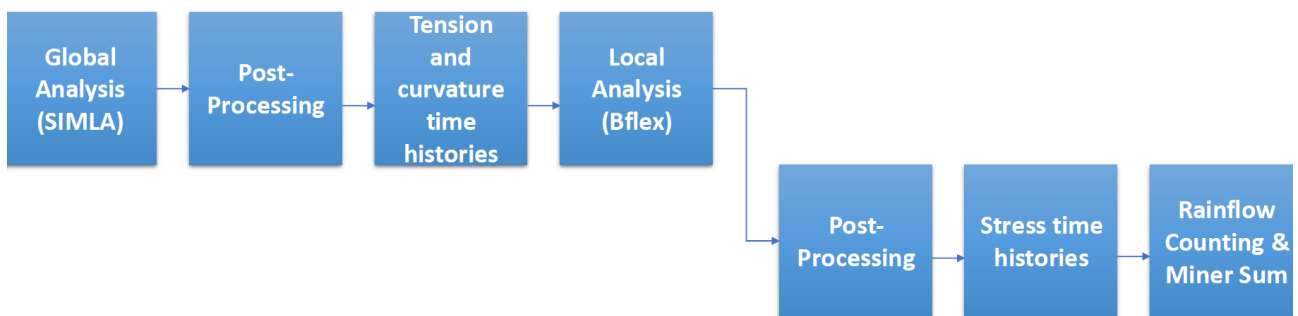


Figure 8.0.1: Analysis methodology to estimate the fatigue life

Once again, the part which is close to the hang-off point will not be considered in this analysis since results achieved by such analysis would not be representing the actual behavior of that specific part in the absence of a bend stiffener.

The fatigue life will be estimated for 4 different conditions by using the environmental loading shown in Table 6.2.3 and 6.2.6 and floater motions in Appendix A:

1. In the presence of VIV, environmental loads and floater motions
2. With environmental loads and floater motions, without VIV
3. In the presence of VIV, environmental loads and floater motions, but the friction between the layers of the cable is deactivated in the local model

4. In the presence of VIV, environmental loads (excluding wave kinematics) and floater motions

8.1 Global Analysis

Global analysis was performed by SIMLA software to obtain the tension and curvature time series based on the global model explained in Section 7.2. Since hogging and sagging sections are subjected to fatigue life calculations, one element from each of them were chosen to be analysed. The selection process is made by considering the curvature values which were computed during the model validation for each elements to identify the maximum curvature along the cable length. Elements with the largest curvatures which are the element 206 for hogging and the element 360 for sagging sections were selected since the fatigue damage in these elements were expected to be the most significant.

Special care must also be given to the selection of the simulation duration. The simulation should be reaching to the steady state within the given time to obtain reliable results. In that purpose, the simulation was run for half an hour by considering the extreme case (case 7). Having confirmed that the steady state was reached at about 140 seconds the computation time was reduced by comparing the standard deviation of the whole tension signal to the standard deviation of its smaller intervals. It turned out that there was less than 1% difference between the standard deviations of the whole signal and the first 11 minutes of it. Thus, 11 minutes was set as the simulation duration, 10 minutes being the dynamic analysis and 1 minute being the static analysis spent on the cable configuration. Besides, time step of 0.01 seconds was used in the analysis.

In order to observe the effect of VIV on the fatigue life, the global analysis was also performed by deactivating the VIV option in SIMLA software. In addition, to cancel the effect of the wave kinematics on the analysis and consider VIV only, a post-processing procedure was followed, see Section 8.1.1 for further details.

8.1.1 Post-Processing

SIMLA gives the axial force and bending moments about y- and z- axis of the selected elements' ends for the sagging and the hogging section in each time step of the analysis.

Since axial forces will be applied to both ends of the local model in opposite directions to create the tension, they were halved before using them as input in the local analysis. When

it comes to bending moments M_y and M_z , they were divided by the bending stiffness EI to be transformed into curvatures κ_y and κ_z , respectively. Then, curvatures were converted into rotation angles θ_y and θ_z . The relation between curvatures and rotation angles are given as:

$$\theta_{y,z} = \frac{L\kappa_{y,z}}{2} \quad (8.1.1)$$

The resulting rotation angles were also halved since the rotation should be applied to both ends of the element equally.

Another required operation is to remove certain frequencies from the curvature and the tension signal. The purpose is to examine only the VIV effect, without considering the wave kinematics. To do so, the time series obtained from global analysis needed to be represented in the frequency domain. This transition was made by using MATLAB's Fast Fourier Transformation (FFT) algorithm. Then, a high pass filter was applied to cancel out all the frequencies between 0.05 Hz and 0.25 Hz because this is the range where wave kinematics are active, see Figure 6.2.2. Having applied the high pass filter, data was converted back into the time domain to be used in the local analysis. MATLAB's Inverse Fast Fourier Transformation (IFFT) algorithm was used to do the transition from the frequency domain to time domain. Original and filtered signals in the frequency domain are shown in Appendix B.

8.2 Local Analysis

Performing local analysis by Bflex software with the output data from the global analysis is required to evaluate stress histories in the steel armour layer and the copper conductor. Then, the fatigue life assessment can be done. Axial stresses are of interest for the analysis since they are critical for fatigue life due to the contact between the metal components (Sævik, 2019a). Same time step and simulation time were implemented in the local analysis as the global analysis. In order to observe the effect of the friction between the structural layers, the output data including the effect of VIV and wave kinematics were used in the local analysis also by neglecting the friction in addition to the regular analysis with the friction.

Different methods were implemented for computing the stress histories of the copper conductor and the steel armour. For the steel armour integration point (IP) results were used. Total of 16 IP were used around the cable to compute stress histories. IP1, IP3 and IP5 of the steel internal armour were chosen to extract stress values, see Figure 8.2.1. The reason for that is these points are a good indication of how much the cross-flow VIV and the pure in-line VIV

contribute to the fatigue life. The fatigue damage due to the CF VIV and the IL VIV will be expected to be maximum at IP 1 and 5, respectively. Because IP1 and IP5 are respectively the locations with maximum out-of-plane (M_z) and in-plane bending (M_y). IP3 is a neutral point which is beneficial to observe the changes between two other points.

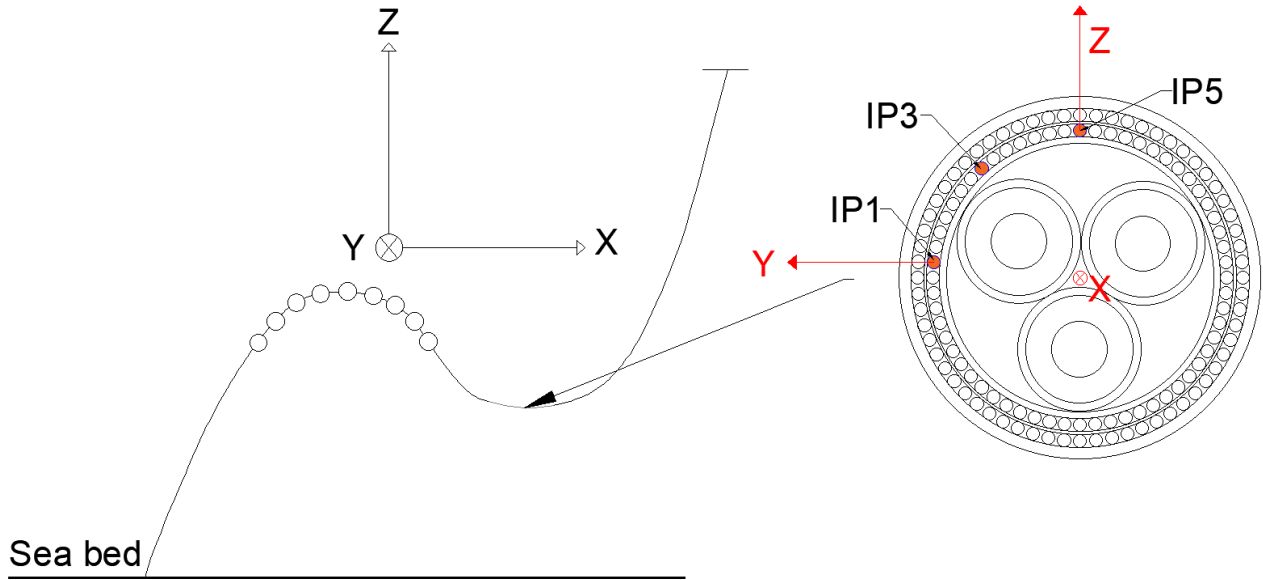


Figure 8.2.1: Integration points to extract stress signals in the steel internal armour layer

When it comes to the copper conductor, a different approach was preferred. Instead evaluating the stress signal in different copper wires of the conductor like the process followed for the steel armour layer, whole centre body was considered as a copper clamp. Besides, plane surfaces were assumed to remain plane after the deformation. To obtain the stress signal in the centre body, the axial force and the bending moments in y - and z - directions were computed. An analytical post-processing procedure was performed to convert the combined effect of the axial force (F_x) and the bending moments (M_y, M_z) into the stress signal. Following Equation 8.2.1 was used in that purpose:

$$\sigma_x = E_c \left(-\frac{F_x}{EA} - \frac{M_y}{EI_y} R_c \sin \theta + \frac{M_z}{EI_z} R_c \cos \theta \right) \quad (8.2.1)$$

Here θ angle takes values of $0, \pi/4, \pi/2$. When it is equal to 0 and $\pi/2$, fatigue damages by CF VIV and IL VIV respectively, are expected to be maximum. The radius of the copper conductor R_c and the elastic modulus E_c is shown in Table 6.1.1. Other parameters are listed in Table 8.2.1 .

$EA[N]$	$EI_y[N/m^2]$	$EI_z[N/m^2]$
1.39×10^7	586	586

Table 8.2.1: Material properties of the center body

8.3 Fatigue Analysis

Turning points in other words peaks and valleys of the stress signals need to be determined prior to the fatigue analysis. Because MATLAB's Rainflow algorithm which requires turning points of the signal as the input, was used to separate stress signals to stress ranges and to compute how many cycles are spent for any of these stress ranges. Figure 8.3.1 shows an example of turning points which belong to the stress signal of the copper conductor in the hogging section for Case 7 when $\theta = 0$.

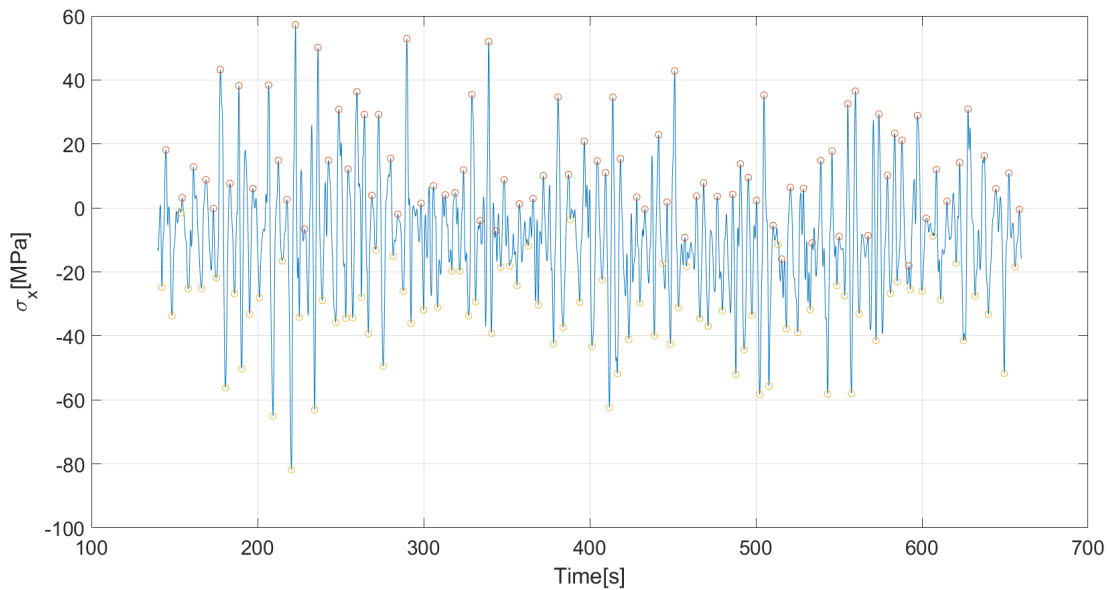


Figure 8.3.1: Turning points of copper conductor's stress signal for Case 7 in Hogging Section ($\theta = 0$)

Having evaluated stress ranges ($\Delta\sigma$) and corresponding cycles (n_i) by Rainflow algorithm of MATLAB, one can estimate the fatigue life for both hogging and sagging sections in any of the three specified points in the steel armour or in the centre body. In that purpose following procedure was applied:

1. SN data given in Section 6.4 was used to find the maximum cycles (N_i) in a specific stress range

$$N_i = \frac{A}{\Delta\sigma} \quad (8.3.1)$$

2. Miner Sum was calculated for each of the 7 loading cases (Table 6.2.3).

$$d_i = \frac{n_i}{N_i} \quad (8.3.2)$$

3. Miner Sum for each case were added together to find the total Miner Sum. However, each loading case has to be multiplied with its probability of occurrence (PO) prior to the summation, see Table 6.2.3.

$$D = \sum_{i=1}^7 d_i PO_i \quad (8.3.3)$$

4. Lastly, calculated Miner Sum needed to be scaled to one year and then reversed to get the fatigue life of the chosen spot in the cable.

$$\text{fatigue life} = \frac{1}{D} \frac{t_s}{24 \times 60 \times 60 \times 365} \quad (8.3.4)$$

where t_s is the simulation duration after the steady state is reached.

Chapter 9

RESULTS & DISCUSSION

In this chapter, results from analyses which have been mentioned in previous sections will be exhibited. Results and necessary discussion will be given for all of the analysis condition listed in Chapter 8.

9.1 Global Analysis Results

Curvature and tension time histories for both hogging and sagging sections resulted from the global analysis were plotted:

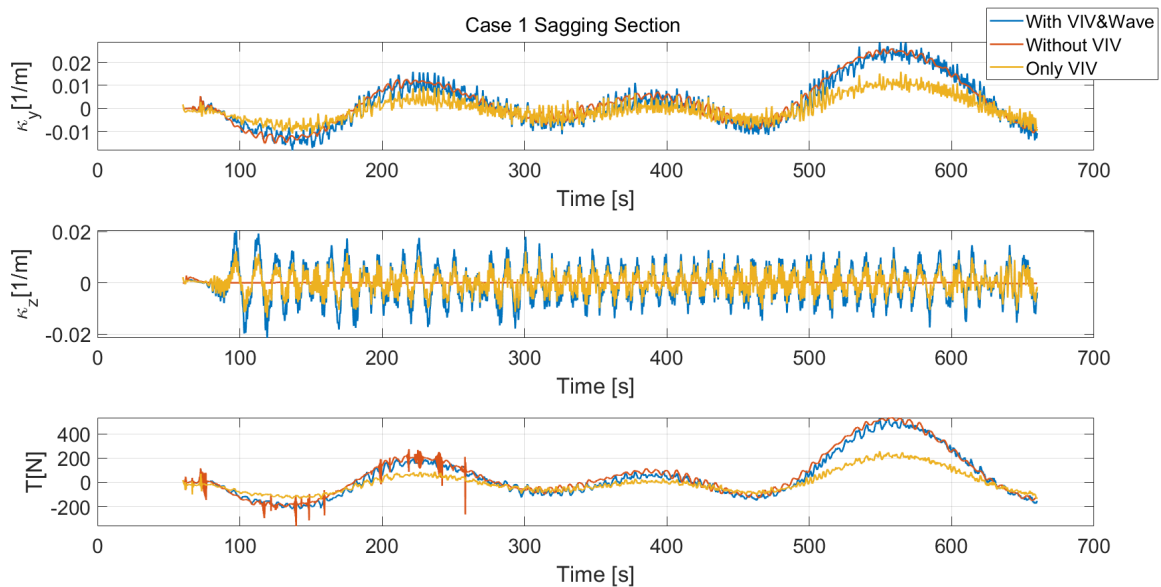


Figure 9.1.1: Global Analysis Results for Case 1 Sagging Section

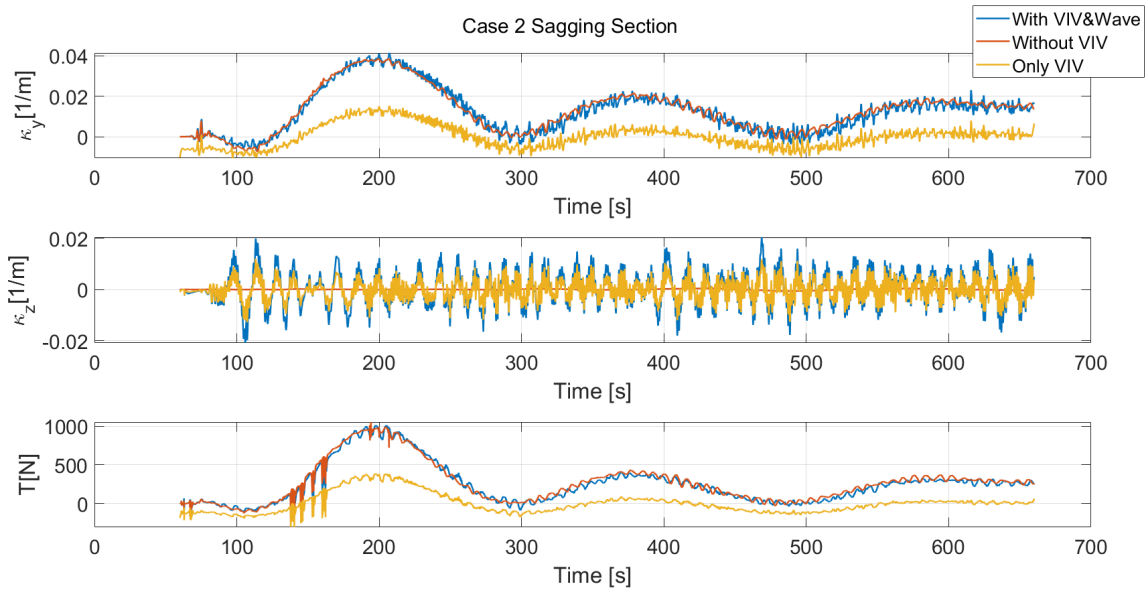


Figure 9.1.2: Global Analysis Results for Case 2 Sagging Section

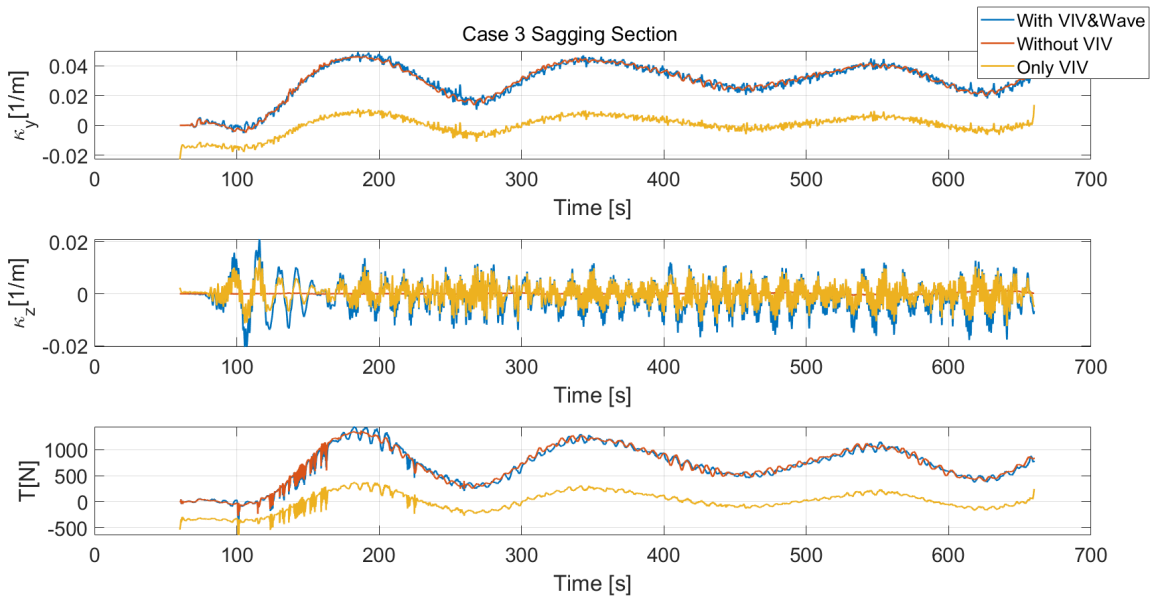


Figure 9.1.3: Global Analysis Results for Case 3 Sagging Section

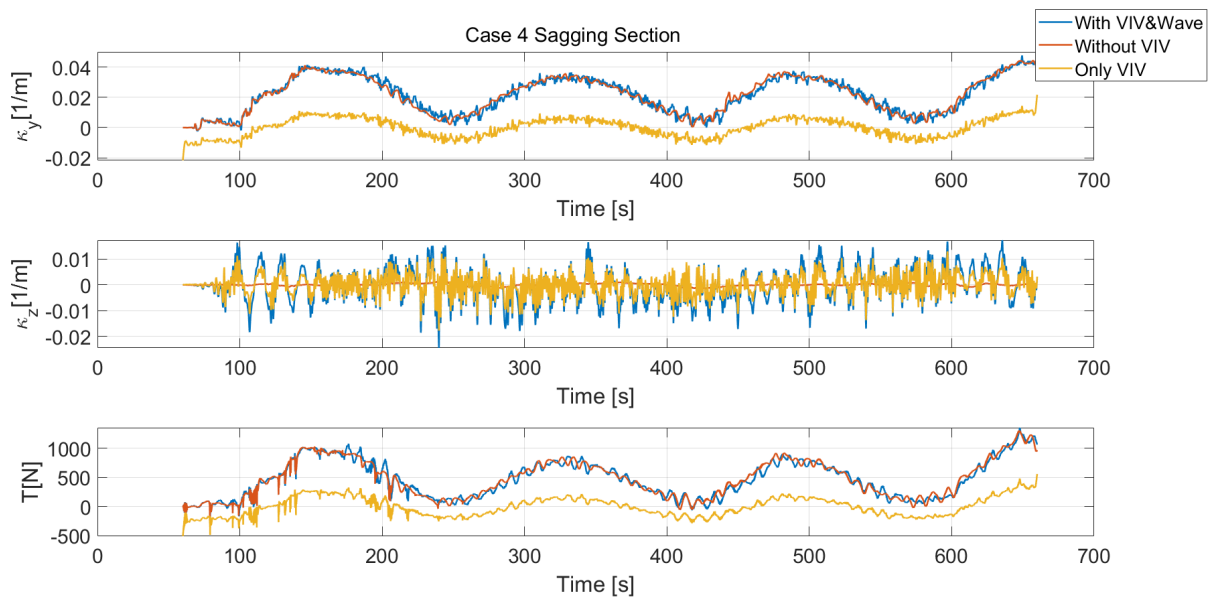


Figure 9.1.4: Global Analysis Results for Case 4 Sagging Section

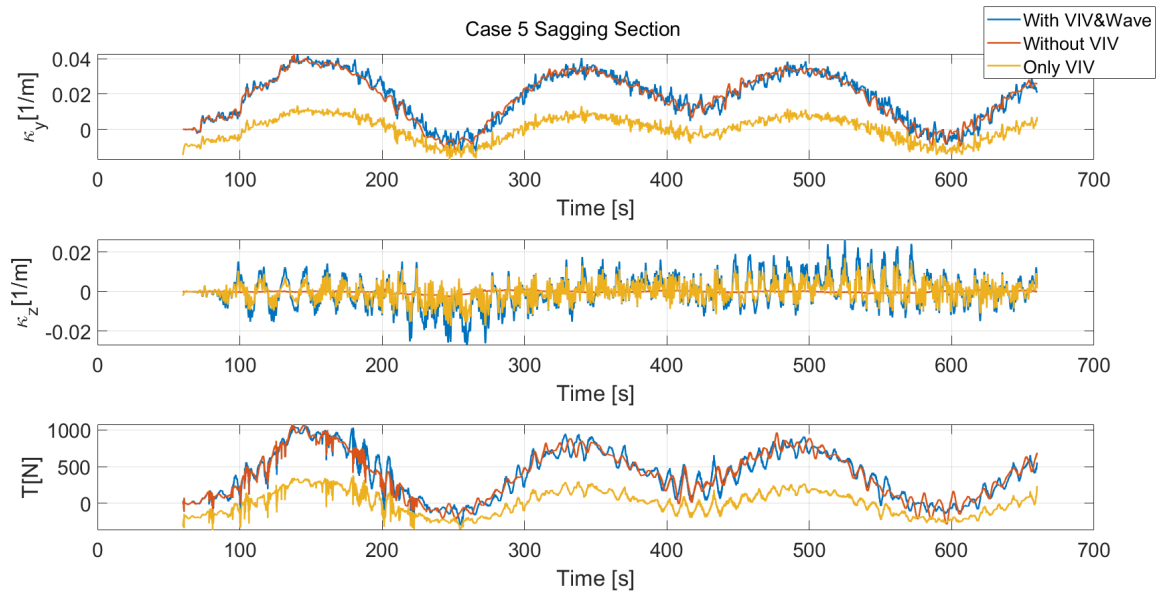


Figure 9.1.5: Global Analysis Results for Case 5 Sagging Section

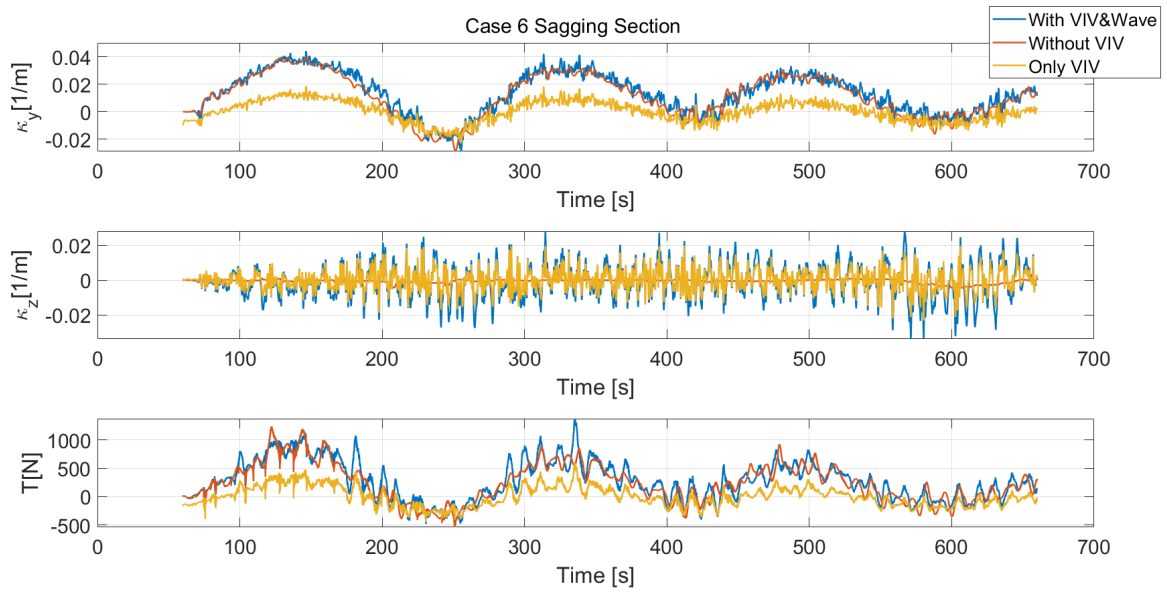


Figure 9.1.6: Global Analysis Results for Case 6 Sagging Section

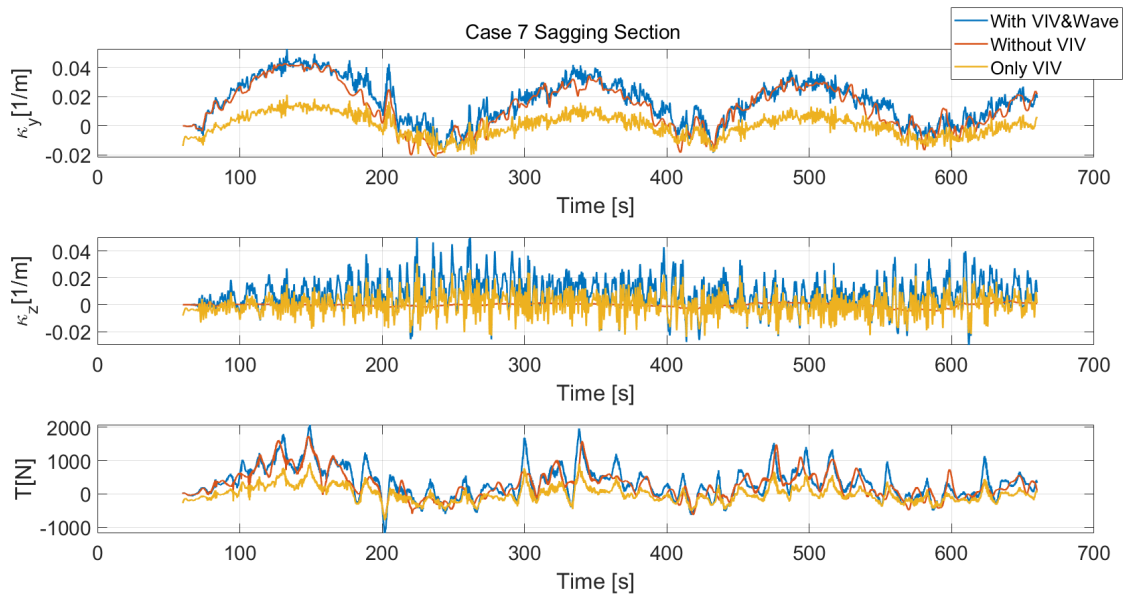


Figure 9.1.7: Global Analysis Results for Case 7 Sagging Section



Figure 9.1.8: Global Analysis Results for Case 1 Hogging Section

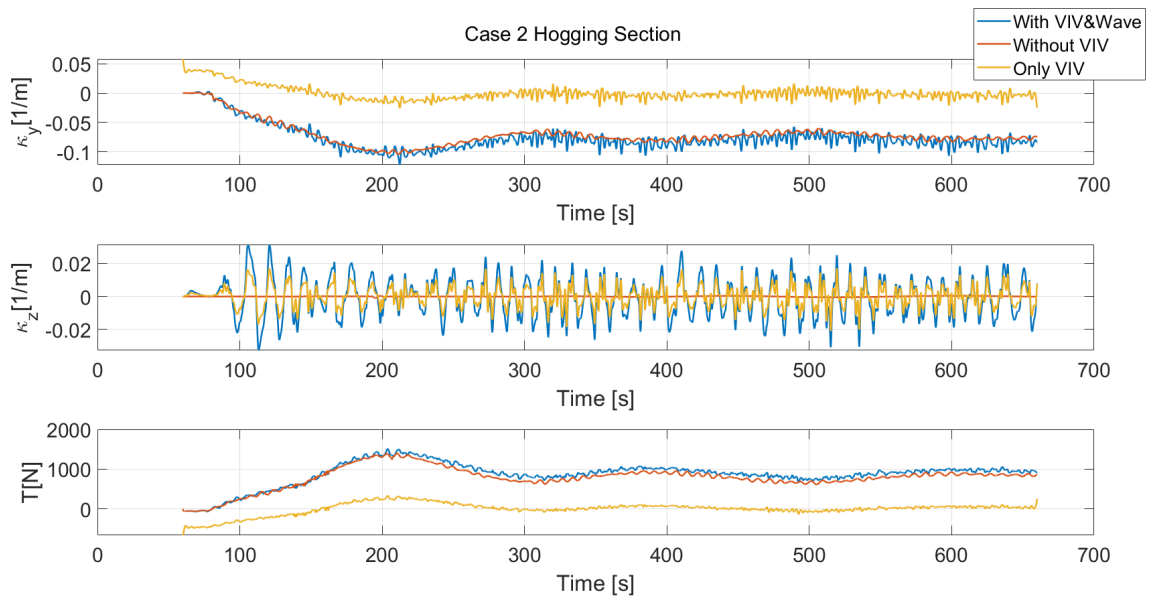


Figure 9.1.9: Global Analysis Results for Case 2 Hogging Section

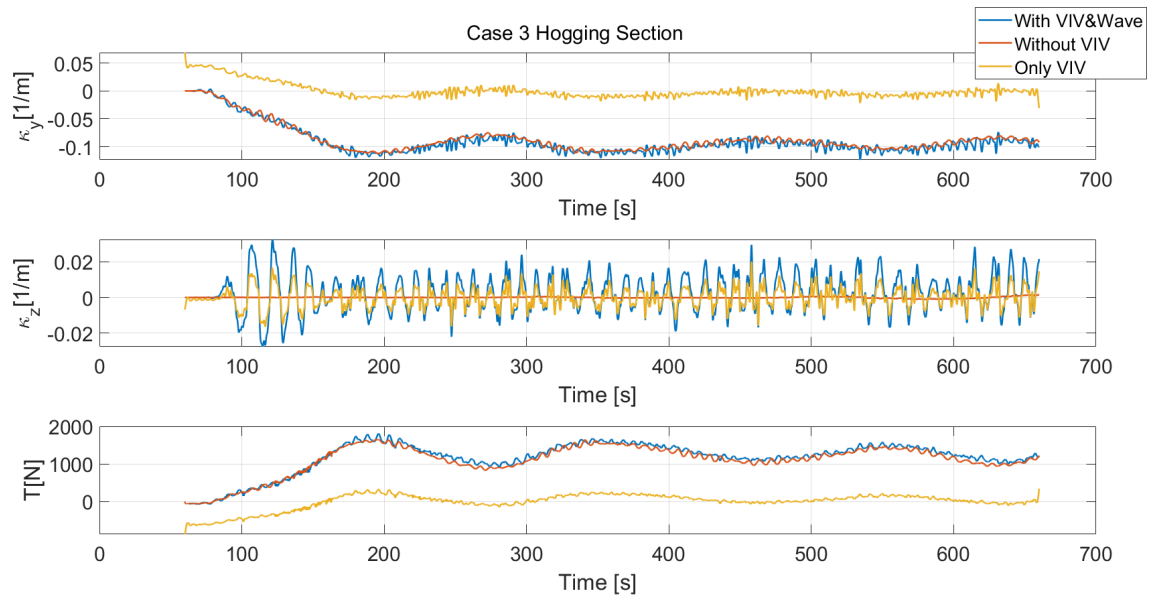


Figure 9.1.10: Global Analysis Results for Case 3 Hogging Section

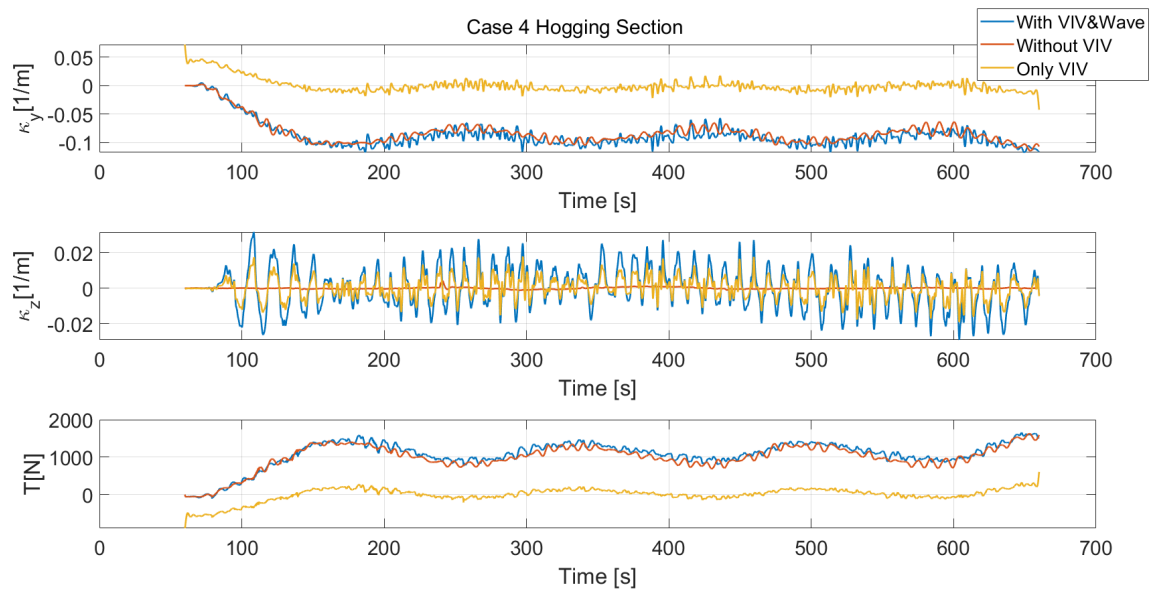


Figure 9.1.11: Global Analysis Results for Case 4 Hogging Section

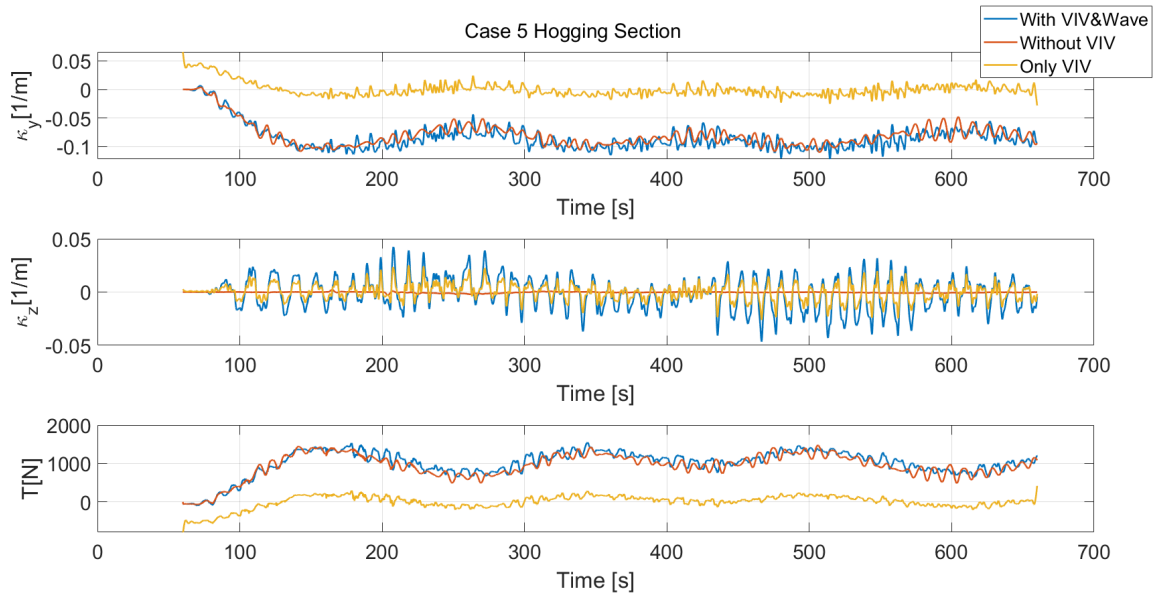


Figure 9.1.12: Global Analysis Results for Case 5 Hogging Section

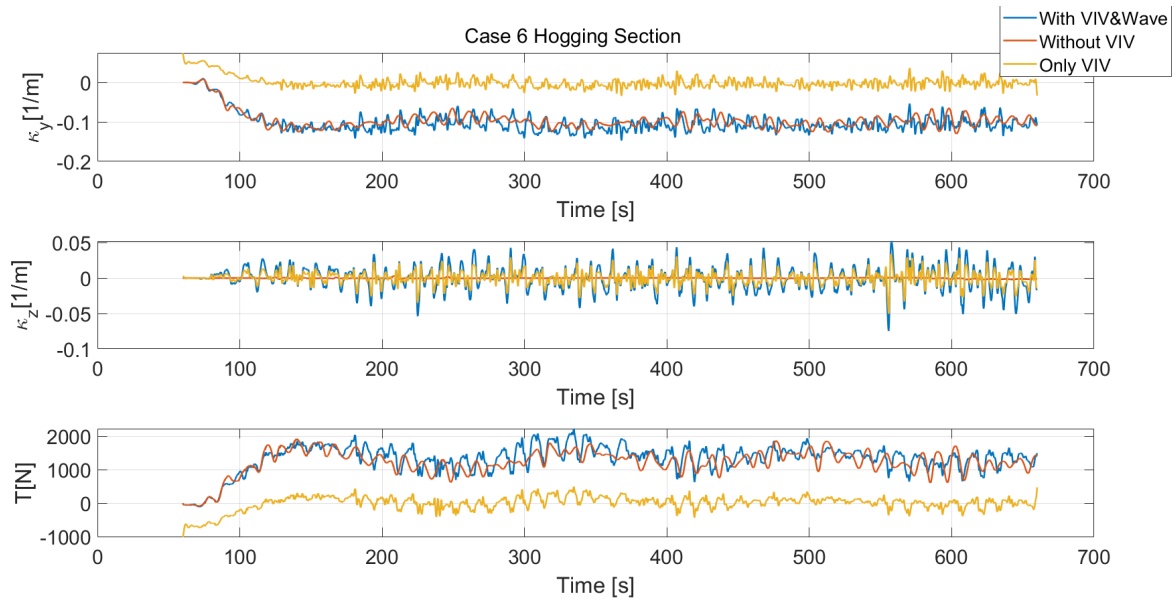


Figure 9.1.13: Global Analysis Results for Case 6 Hogging Section

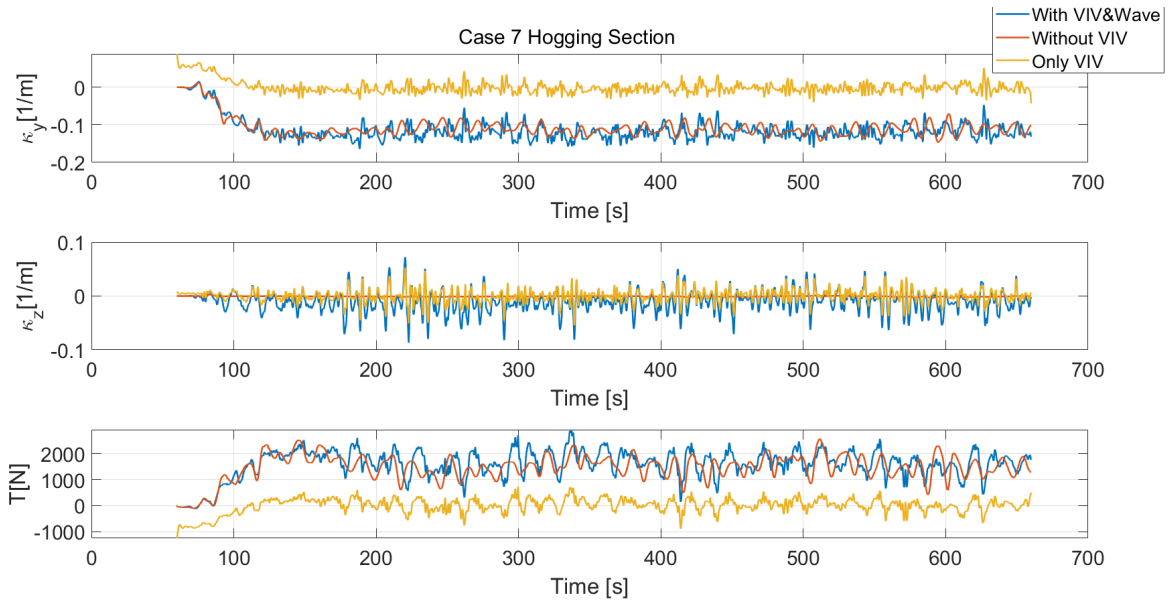


Figure 9.1.14: Global Analysis Results for Case 7 Hogging Section

First of all, results for only VIV condition give valuable insight into the global response of the power cable. Although the current acts on the structure in IL direction, CF response amplitude is higher. It is a sign indicating that CF vibrations are the governing factor for the fatigue. Besides, CF vibrations being critical for the fatigue life means that the power cable is a bending dominated slender structure (Ulveseter et al., 2018). Thus, it would be ideal to discuss the results with respect to in-plane and out-of-plane bendings M_y and M_z , respectively. When observing the results the difference between the values of κ_z in the presence and absence of VIV stands out. When VIV is not present, κ_z takes values that are almost zero. If VIV is activated, a dramatic increase in κ_z occurs due to the increased out-of-plane bending. Thus, a significant decrease of fatigue life should be observed at the location where CF response due to VIV is maximum, when VIV comes into play.

It can be also seen that wave kinematics does not have a significant effect on κ_z . Whereas the influence of wave kinematics on κ_y is massive. That tells us the in-plane-bending is highly dependent on wave kinematics. However, there are small discrepancies between κ_y values for the cases with VIV and without VIV. It means wave kinematics are more critical than the in-line VIV when it comes to the in-plane-bending.

On the other hand, tension time series are also similar in amplitude both in the presence and in the absence of VIV. However, signals recorded by considering VIV have smaller oscillating periods in other words, higher frequencies than signals recorded by neglecting VIV. Since high

frequent loads are harmful for the fatigue life of the structure, the tension caused by combined wave-VIV will be more detrimental than the one created by only wave kinematics. Besides, when the frequency range where wave kinematics are active is cancelled out, the decline in the tension amplitude is considerable. This effect is more significant for the hogging section. Because, the sagging section is located at a deeper water depth than the hogging section. The effect of the wave loading attenuates as the water depth is increasing. It can be said that the tension variation in the hogging section is governed by the wave kinematics. That is why the change in tension amplitude is bigger for the hogging section than the one for the sagging section when wave kinematics are not taken into account.

9.2 Local Analysis Results

Curvature and tension time series are given as input to the local analysis to obtain stress signals for the specified locations for the specific condition. Results for the most extreme case are as follows:

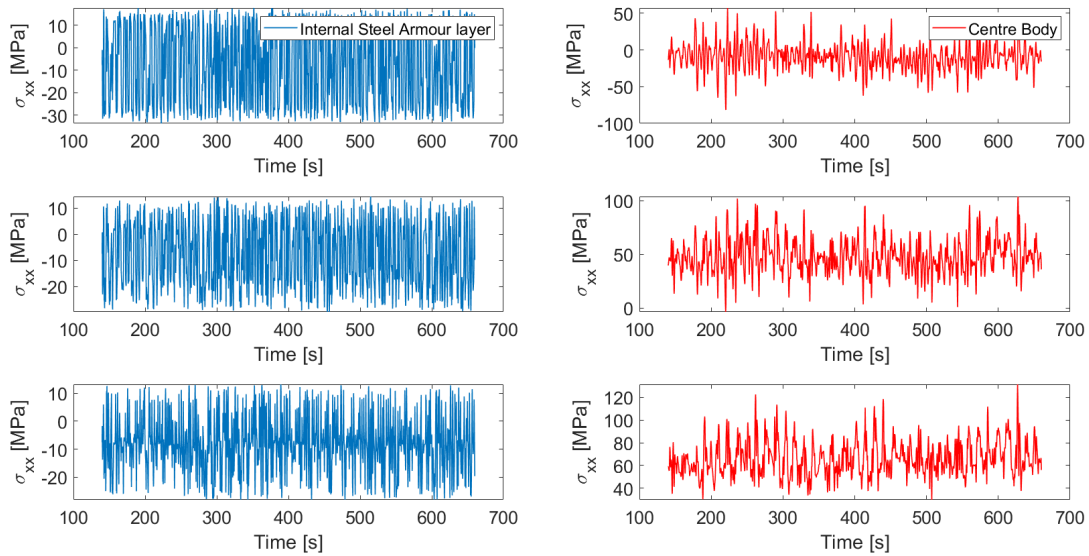


Figure 9.2.1: Stress signals for the hogging section for the most extreme loading case in the presence of both wave loads and VIV

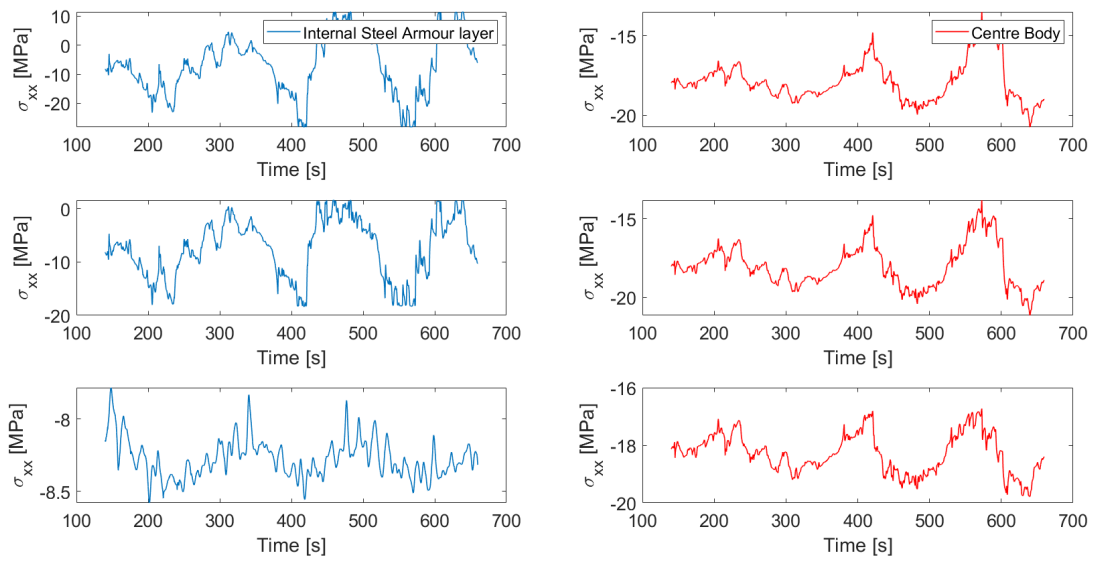


Figure 9.2.2: Stress signals for the hogging section for the most extreme loading case without VIV

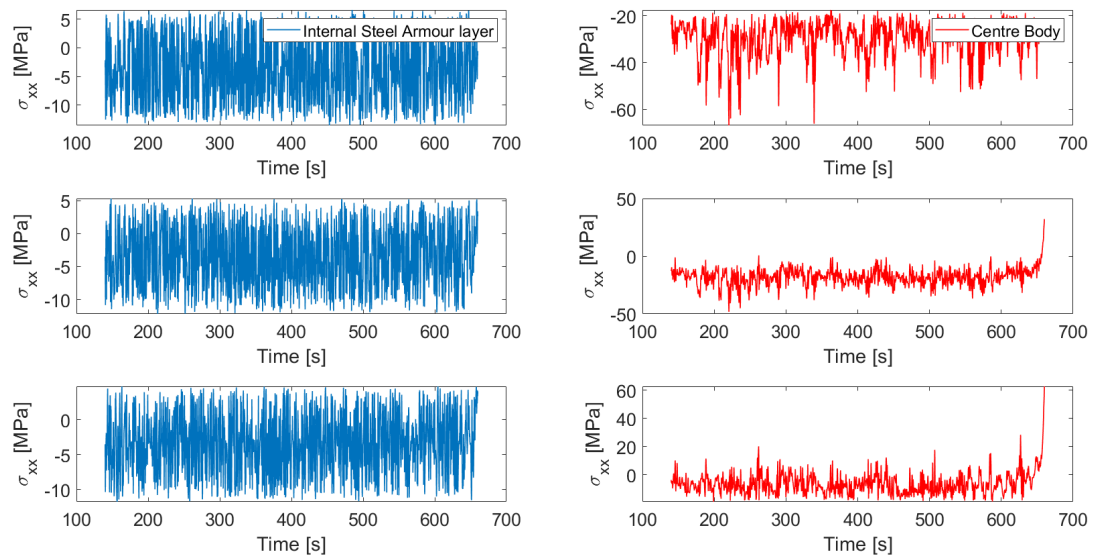


Figure 9.2.3: Stress signals for the hogging section for the most extreme loading case without wave kinematics

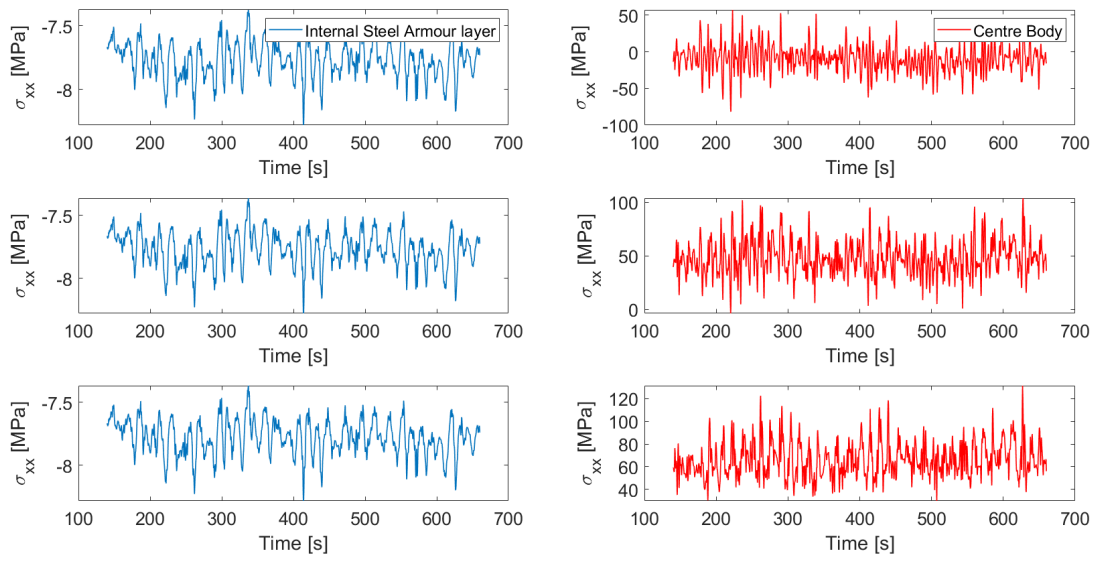


Figure 9.2.4: Stress signals for the hogging section for the most extreme loading case without the friction between the contact surfaces

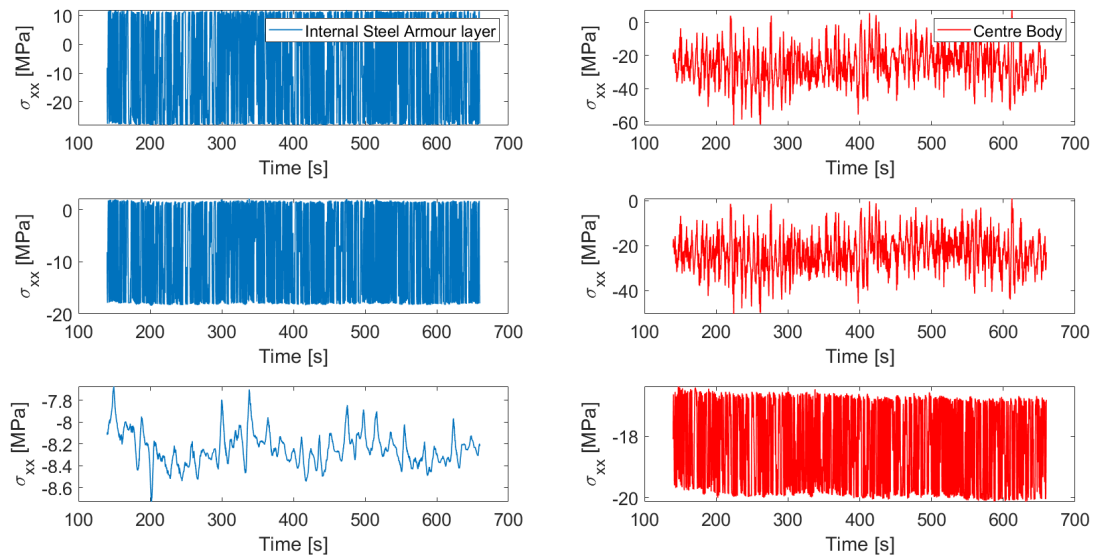


Figure 9.2.5: Stress signals for the sagging section for the most extreme loading case in the presence of both wave loads and VIV

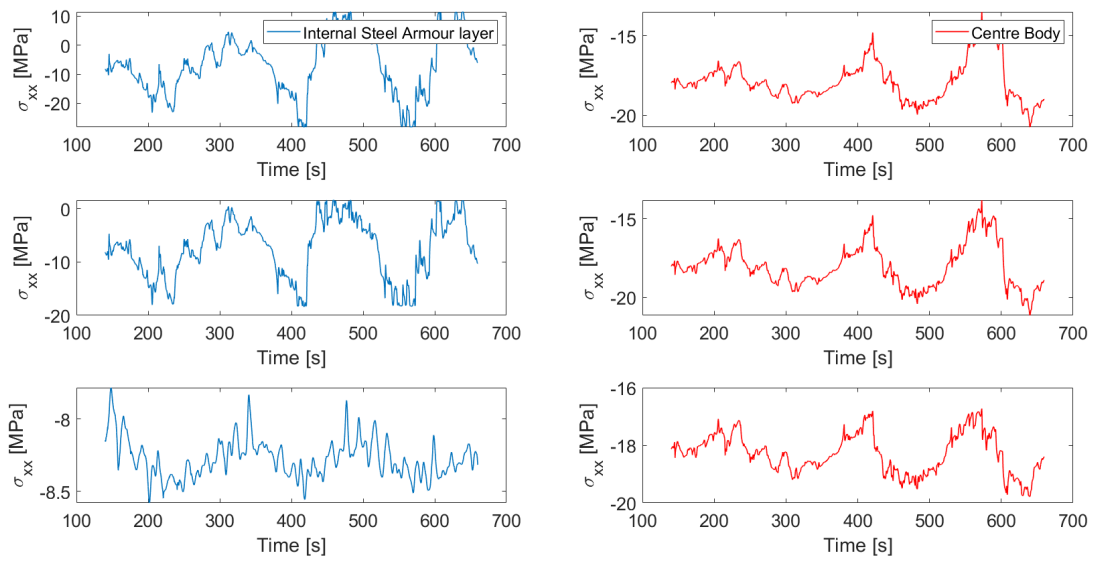


Figure 9.2.6: Stress signals for the sagging section for the most extreme loading case without VIV

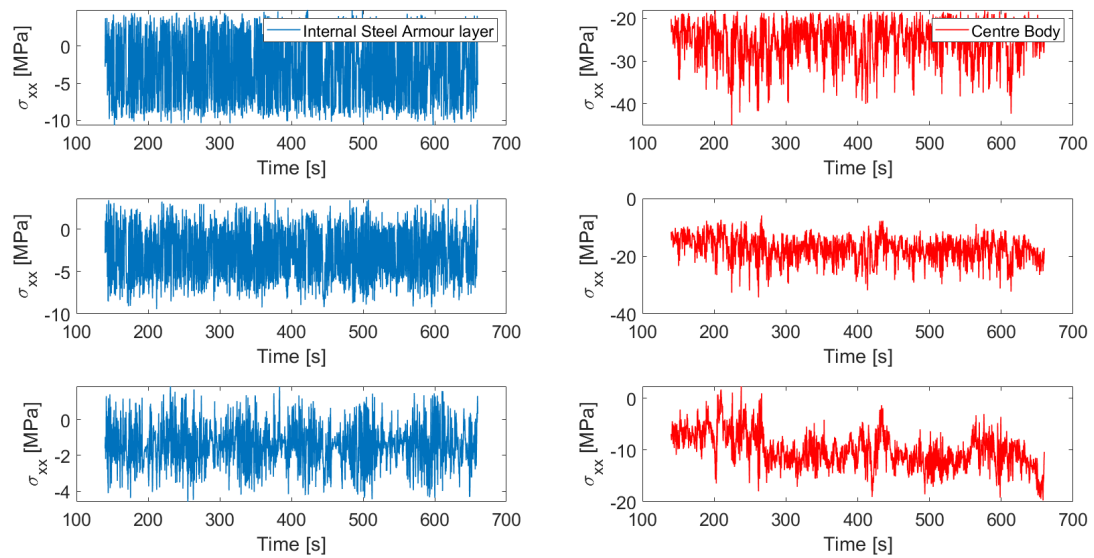


Figure 9.2.7: Stress signals for the sagging section for the most extreme loading case without wave kinematics

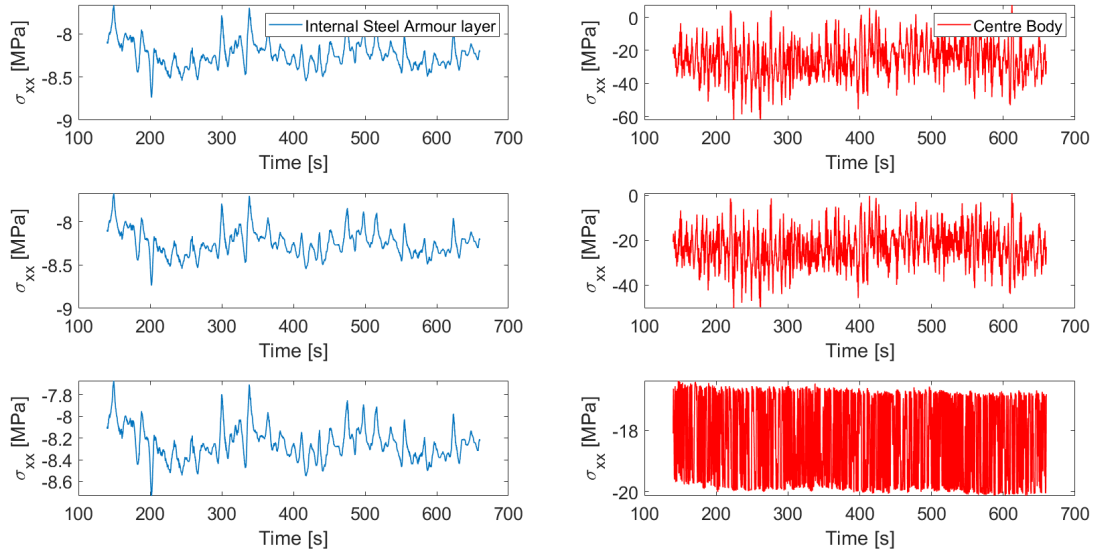


Figure 9.2.8: Stress signals for the sagging section for the most extreme loading case without the friction between the contact surfaces

One of the important thing to be noticed is that the huge decrease in stress values when VIV is removed from the system. This decline is way smaller when wave kinematics are neglected. Another thing is that, results for the centre body with and without the friction are identical. Because stress histories for centre body were obtained analytically and in the calculation process frictions between the contact surfaces were not involved.

9.3 Fatigue Analysis Results

Fatigue life results for both the internal steel armor layer and centre body which includes copper conductors are calculated by following the procedure described in Section 8.3. Results are given in Tables 9.3.1 and 9.3.2. It should be noted that a safety factor of 10 is applied to the results.

Location	VIV+Wave	Without VIV	Only VIV	Without Friction
Sagging Section $\theta = 0$	5.57E+06	3.60E+13	7.23E+06	5.57E+06
Sagging Section $\theta = \pi/4$	2.82E+07	2.07E+13	4.62E+08	2.82E+07
Sagging Section $\theta = \pi/2$	8.41E+11	1.24E+13	2.71E+15	8.41E+11
Hogging Section $\theta = 0$	1.61E+05	3.88E+12	8.43E+05	1.61E+05
Hogging Section $\theta = \pi/4$	3.42E+05	7.67E+07	6.74E+07	3.42E+05
Hogging Section $\theta = \pi/2$	6.43E+05	7.09E+06	8.96E+11	6.43E+05

Table 9.3.1: Fatigue life results in years for the centre body

Location	VIV+Wave	Without VIV	Only VIV	Without Friction
Sagging Section IP=1	46.85	2.84E+04	49.25	4.62E+11
Sagging Section IP=3	6.12E+02	2.49E+05	3.28E+03	4.69E+11
Sagging Section IP=5	4.78E+11	7.21E+12	6.31E+15	4.77E+14
Hogging Section IP=1	82.74	1.70E+05	95.84	8.55E+02
Hogging Section IP=3	1.58E+02	1.69E+03	9.72E+03	6.94E+11
Hogging Section IP=5	2.07E+02	2.17E+02	5.43E+08	7.01E+11

Table 9.3.2: Fatigue life results in years for the internal steel armor layer

It can be seen that shortest fatigue lives occur in the steel armor layer when both VIV and wave kinematics are present. Most critical location regarding to the fatigue damage appears to be the IP 1 in the internal steel armor layer, see Figure 8.2.1. Large out-of-plane bending M_z due to the CF VIV has a detrimental effect on the fatigue life of the armor layer at IP 1 because it is the location where CF response due to VIV is maximum. Same situation can be observed for the centre body. Fatigue damages are larger where the effect of CF VIV is maximum ($\theta = 0$). However, overall fatigue resistance of the centre body is much better than the steel armor. This might be due to the fact that the steel armor carries the tension loads and protects copper conductors to be excessively loaded.

For the case which considers both VIV and wave kinematics, when the influence of the CF VIV decreases fatigue lives go up significantly. For instance, neutral points which are IP 3 and $\theta = \pi/4$ for the steel armor and the centre body, respectively, are less critical than the IP1 and $\theta = 0$ concerning the fatigue damage. For the same case locations where vibrations due to in-line VIV is maximum (IP 5 and $\theta = \pi/2$), longer fatigue lives are observed compared to other locations of the cross-section. That means the in-plane bending M_y gives less damage

to the power cable than M_z does. The hogging section takes much more fatigue damage than the sagging section at points where IL VIV contribute the fatigue damage the most (IP 5 and $\theta = \pi/2$). The reason for that is the wave and current loads acting on the element taken from the hogging section are larger compared to ones acting on the sagging section. Because, wave and current loads become smaller as going deeper in the water.

The destructive effect of VIV on the fatigue life can be seen by observing analysis results without including VIV. A dramatic increase in fatigue lives occurs in locations with the maximum M_z . That is caused by the reduction in M_z amplitude in the absence of CF VIV. Lowest increase rate in the fatigue life is seen at locations with the maximum M_y (IP 5 and $\theta = \pi/2$). Especially for the hogging section difference between the fatigue life with and without VIV, is really small. That might mean that wave kinematics and current loads which cause magnified drag forces, are the governing factor for fatigue life in the hogging section. It can be understood by comparing results for VIV+Wave and only VIV cases. When wave kinematics are excluded, a huge jump is observed in fatigue lives of locations which are affected from IL VIV the most. The increase rate for the hogging section is way larger than the one for the sagging section indicating wave kinematics are the main contributor for the in-plane bending M_y in the hogging section. It can be also seen by comparing the results for the cases with and without wave kinematics in locations where IP = 1 and $\theta = 0$ that the fatigue life due to CF vibrations does not experience a noticeable change when the effect of waves are removed. Thus, wave kinematics are not an important factor for CF response.

Lastly, the axial friction between the layers seems to be a crucial factor for the fatigue life since fatigue lives experience a dramatic increase when it is deactivated. The reason why no change occurs for the centre body is because stress histories for it are calculated by bending moments M_z , M_y and tension force T , see Equation 8.2.1 which are not depend on the friction between layers.

Chapter 10

CONCLUSION & FURTHER WORK

10.1 Conclusion and Summary

This thesis work aims to demonstrate how dangerous VIV are for the structural integrity of dynamic power cables applied in OWT. A global model was created to represent the general behavior of the dynamic power cable. Material properties of the cable was extracted from the local model.

Global analyses were performed in SIMLA software based on the created global model for 7 different loading cases. Analyses were repeated also by deactivating VIV to detect its significance on the fatigue life. Analyses gave the results for tensions, in-plane and out-of-plane curvature variations as a function of time for elements with the maximum curvature from both the sagging and the hogging sections. To investigate the contribution of wave kinematics to the fatigue damage, global analyses results with VIV were cleared from the frequency range in which wave kinematics are active by a filtering process, see Section 8.1.1. Time series for these 3 conditions were used as input to local analyses in BFLEX. Local analyses for combined VIV-wave kinematics were performed also by neglecting the friction between the layers and cable components.

Stress signals in the axial direction are used to conduct the fatigue assessment of the structure. Rainflow algorithm and then the Miner Sum were applied for estimating the fatigue life for selected locations in the cross-section for each condition explained previously.

Locations critical with respect to fatigue damage were evaluated. Analyses have exhibited valuable findings showing why VIV have large importance for the design of subsea power cables. Also, it became clear that other aspects such as wave loads and frictions between contact surfaces should be taken into account for the fatigue design process. Hydrodynamic loads

which were represented by Morison's equation combined with excitation forces due to VIV were implemented successfully to the global model. Besides, the local model very well displayed the value of local effects, especially the interaction between the layers. Above all, time domain analyses had great success to capture the non-linear nature of the dynamic power cable under the effect of VIV and environmental loads. Thanks to the time domain model, variations in tension and bending loads along the cable were obtained with a good resolution which makes it possible to conduct a detailed fatigue assessment.

10.2 Recommendations for Further Work

Following recommendations are assumed to be suitable for the further work:

- A bending stiffener must be implemented to the hang-off point to study the fatigue damage in the presence of excessive bending at that location. In this thesis hang-off point was assumed to be a hinged connection. Thus, rotational motions can not be included and the fatigue damage of the element joining cable to the floater could not be studied.
- As the most critical location regarding to fatigue damage is the internal steel armor layer in the CF direction, special care must be given to that point. Bending stiffness of the cable might be increased by the usage of a material with larger elastic modulus to prevent the excessive fatigue damage to be accumulated. A similar operation should be performed for the IL direction. Then the effect of increased bending stiffness on the fatigue strength can be observed.
- A more detailed model for the cable-sea bed interaction might be useful to investigate the influence of non-linearities caused by this connection. Especially, it should be well recognized how the global response of the cable varies with respect to the soil-damping.
- All analyses should be performed considering several directions for the environmental loading (wind, current, waves) to see if it is an important factor for the analysis.
- Local model can be updated to include contact surfaces for copper conductors. That way the effect of the friction on the fatigue strength of copper wires can be examined.

References

- Achenbach, E., & Heinecke, E. (1981). *On vortex shedding from smooth and rough cylinders in the range of Reynolds numbers 6×10^3 to 5×10^6* . *Journal of fluid mechanics*, 109(12), 239–251.
- American Petroleum Institute. (2008). *Recommended Practice for Flexible Pipe* (4th ed.). American Petroleum Institute.
- Aronsen, K. H. (2007). *An experimental investigation of in-line and combined in-line and cross-flow vortex induced vibrations*.
- As, S., & Berge, S. (2017). *Fatigue and Fracture Design of Marine Structures* (3rd revised edition ed.). Trondheim, Norway: Norwegian University of Science and Technology.
- Bakken, K. (2019). *Fatigue of dynamic power cables applied in offshore wind farms*. NTNU. Retrieved from <http://hdl.handle.net/11250/2622927>
- Bingham, H. B. (2019). *Supplemental Lecture Note for: “Wave Loads on Ships and Offshore Structures”*.
- Blevins, R. D. (1977). *Flow-induced vibration*. New York.
- DNV. (2012). *Electrical Power Cables in Subsea Applications, DNV-RP-F401*. Det Norske Veritas.
- DNV. (2014). *Design of Offshore Wind Turbine Structures, DNV-OS-J101*. Det Norske Veritas.
- DNV. (2016). *Subsea Power Cables for Wind Power Plants, DNV GL-ST-0359*. Det Norske Veritas.
- DNVGL. (2014). *Fatigue design of offshore steel structures, DNV-RP-C203*. DNVGL.
- Faltinsen, O. M. (2000). *Sea loads on high-speed marine vehicles*. Trondheim: Marinteknisk senter, Institutt for marin hydrodynamikk.
- Gopalkrishnan, R. (1993). *Vortex-induced forces on oscillating bluff cylinders* (Tech. Rep.). Woods Hole Oceanographic Institution MA.
- Larsen, C. M. (2020). *Lecture notes Vortex Induced Vibrations*.
- Larsen, C. M., Koushan, K., & Passano, E. (2002). *Frequency and time domain analysis of vortex induced vibrations for free span pipelines*. In *International Conference on Offshore Mechanics and Arctic Engineering* (Vol. 36118, pp. 103–111).
- Larsen, C. M., Vikestad, K., Yttervik, R., Passano, E., & Baarholm, G. S. (2008). *VIVANA-Theory Manual Version 3.6*. Norwegian Marine Technology Research Institute, Trondheim, Norway.
- Leroy, J.-M., Poirette, Y., Brusselle Dupend, N., & Caleyron, F. (2017). *Assessing mechanical stresses in dynamic power cables for floating offshore wind farms*. In *International Con-*

- ference on Offshore Mechanics and Arctic Engineering (Vol. 57786, p. V010T09A050).
- Lifes50+. (2015). *Qualification of innovative floating substructures for 10MW wind turbines and water depths greater than 50m* (Tech. Rep.). Retrieved from https://lifes50plus.eu/wp-content/uploads/2015/11/D72_Design_Basis_Retyped-v1.1.pdf
- Mathisen, K. M. (1992). *Large displacement analysis of flexible and rigid systems considering displacement-dependent loads and nonlinear constraints*.
- Nasution, F. P., Sævik, S., & Berge, S. (2014). *Experimental and finite element analysis of fatigue strength for 300 mm² copper power conductor*. *Marine Structures*, 39, 225–254.
- Passano, E., Larsen, C. M., Lie, H., & Wu, J. (2014). *VIVANA-Theory Manual Version 4.2*. Norwegian Marine Technology Research Institute, Trondheim, Norway.
- Patrick, D., Fardo, S. W., & Fardo, S. (1999). *Understanding dc circuits*. Newnes.
- Sarpkaya, T. (1978). *Fluid forces on oscillating cylinders*. *Journal of the Waterway, Port, Coastal and Ocean Division*, 104(3), 275–290.
- Sævik, S. (2017). *Simla Theory Manual*.
- Sævik, S. (2019a). *Offshore Pipelines and Flexibles lecture notes*.
- Sævik, S. (2019b). *BFLEX Theory Manual*.
- Sævik, S., Økland, O. D., Baarholm, G. S., & Gjøsteen, J. K. (2019). *Simla-User Manual Version 3.16.0*. Norwegian Marine Technology Research Institute, Trondheim, Norway.
- Thorsen, M. J., & Norges teknisk-naturvitenskapelige universitet Institutt for marin teknikk. (2016). *Time domain analysis of vortex-induced vibrations (Vols. 13–2016)*.
- Thorsen, M. J., Sævik, S., & Larsen, C. M. (2014). *A simplified method for time domain simulation of cross-flow vortex-induced vibrations*. *Journal of Fluids and Structures*, 49, 135–148.
- Ulveseter, J. V. (2015). *Non-linear time domain analysis of vortex induced vibrations* (Unpublished master's thesis). NTNU.
- Ulveseter, J. V., Sævik, S., & Larsen, C. M. (2017). *Time domain model for calculation of pure in-line vortex-induced vibrations*. *Journal of Fluids and Structures*, 68, 158–173.
- Ulveseter, J. V., Thorsen, M. J., Sævik, S., & Larsen, C. M. (2018). *Time domain simulation of riser VIV in current and irregular waves*. *Marine Structures*, 60, 241–260.
- Vandiver, J. K., & Li, L. (2005). *Shear7 V4. 4 program theoretical manual*. Massachusetts Institute of Technology.
- Venugopal, M., & Vandiver, J. K. (2004). *Cross flow and in-line damping measurements from forced excitations of a flexible cylinder in a uniform flow*. In International Conference on Offshore Mechanics and Arctic Engineering (Vol. 37459, pp. 773–786).
- Vikestad, K., Vandiver, J., & Larsen, C. (2000). *Added mass and oscillation frequency for a*

circular cylinder subjected to vortex-induced vibrations and external disturbance. Journal of Fluids and Structures, 14(7), 1071–1088.

Appendix A

Floater Motions

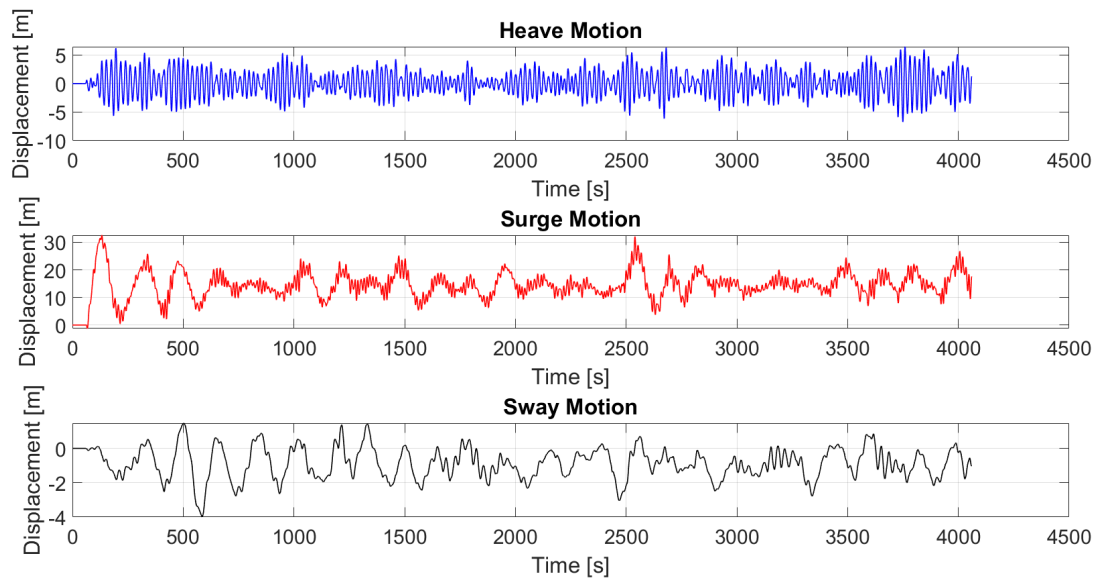


Figure A.0.1: Floater Motions for Case 7

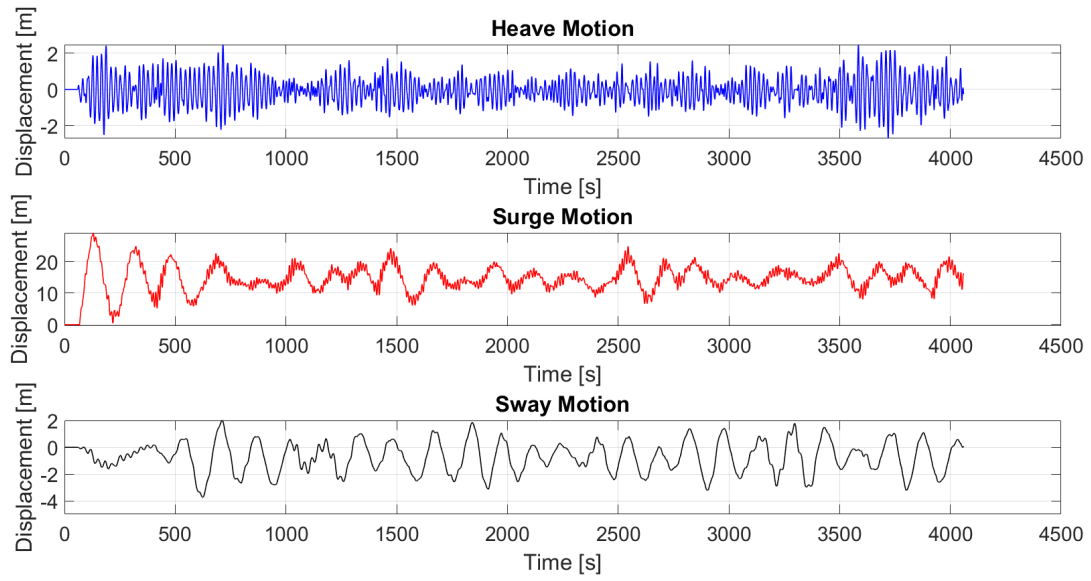


Figure A.0.2: Floater Motions for Case 6

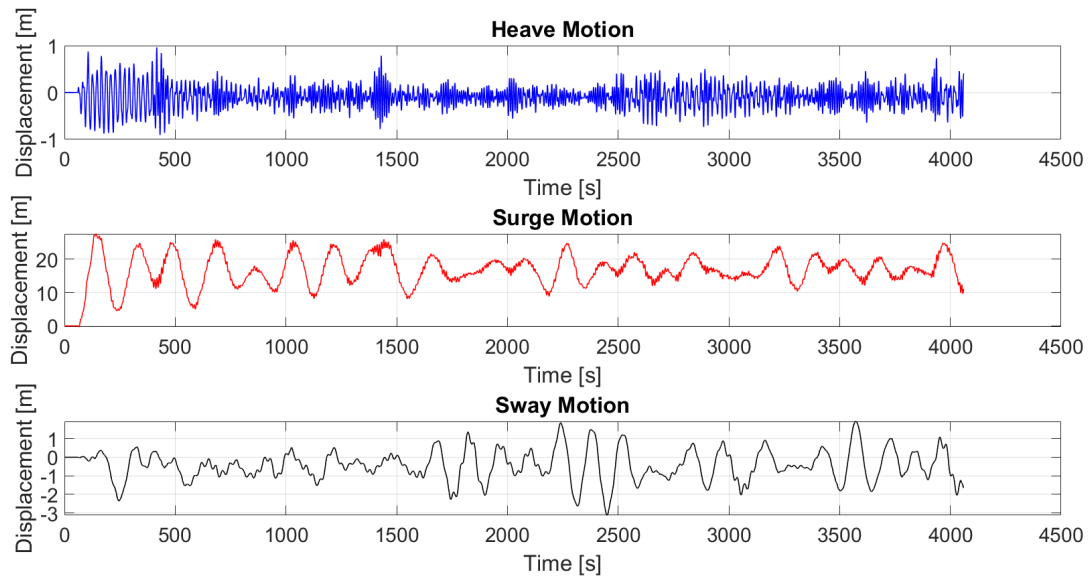


Figure A.0.3: Floater Motions for Case 5

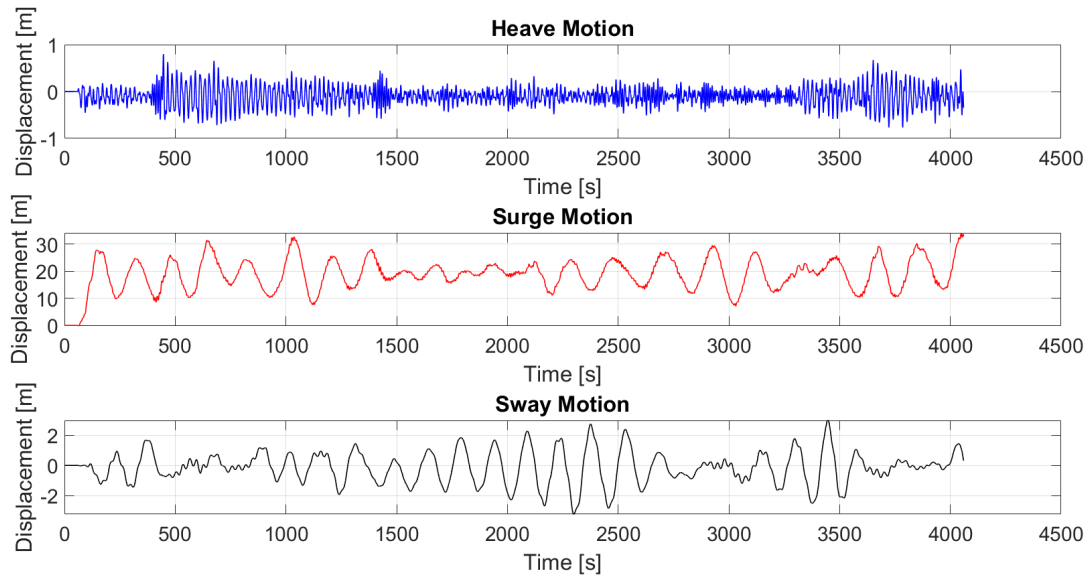


Figure A.0.4: Floater Motions for Case 4

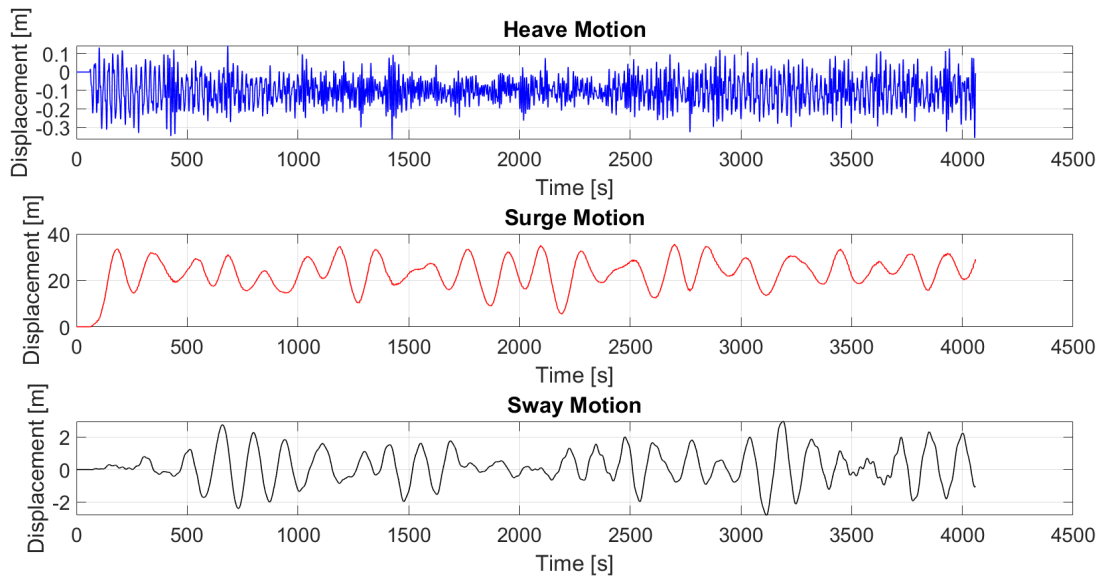


Figure A.0.5: Floater Motions for Case 3

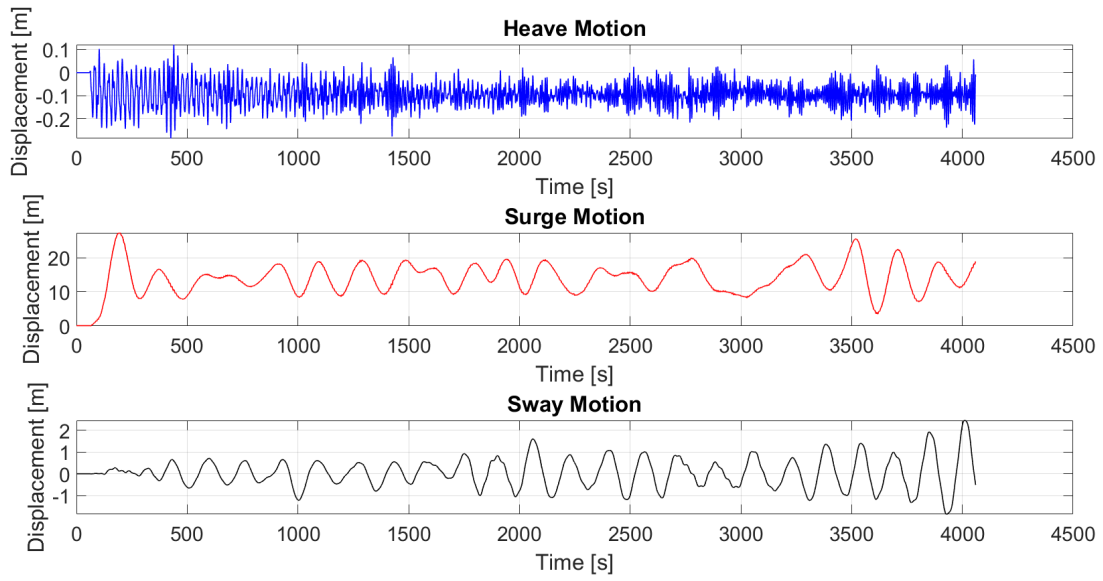


Figure A.0.6: Floater Motions for Case 2

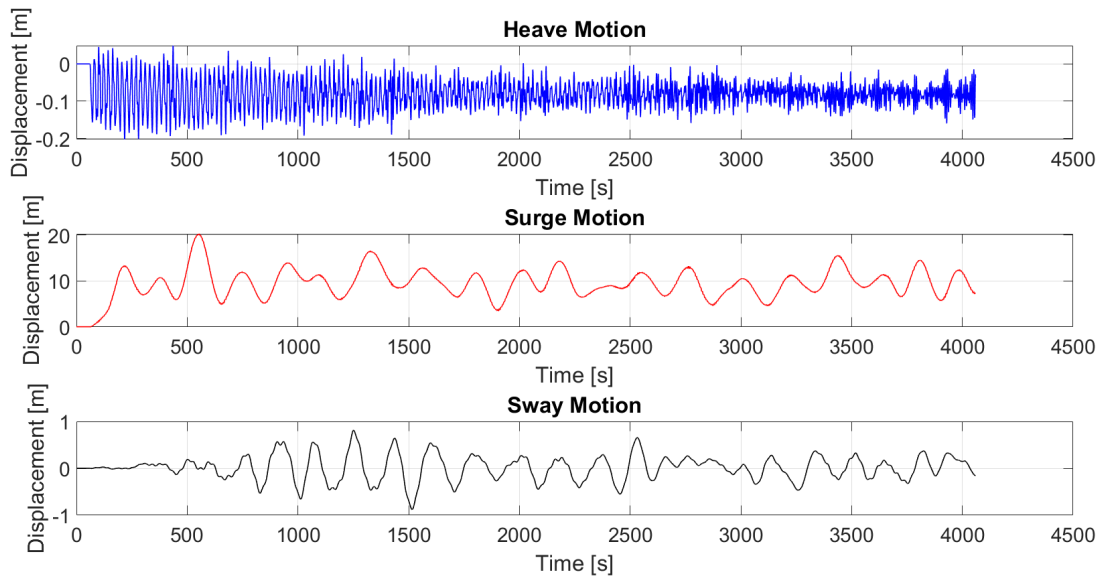


Figure A.0.7: Floater Motions for Case 1

Appendix B

Global Analysis Results in Frequency Domain

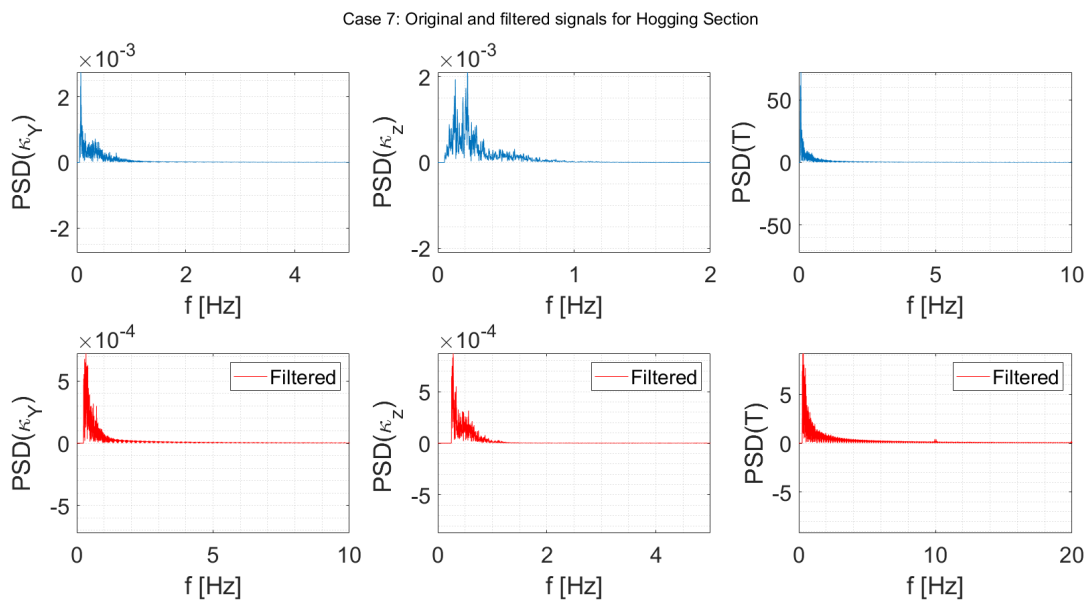


Figure B.0.1: Global Analysis Results in the Frequency Domain for Case 7 Hogging Section

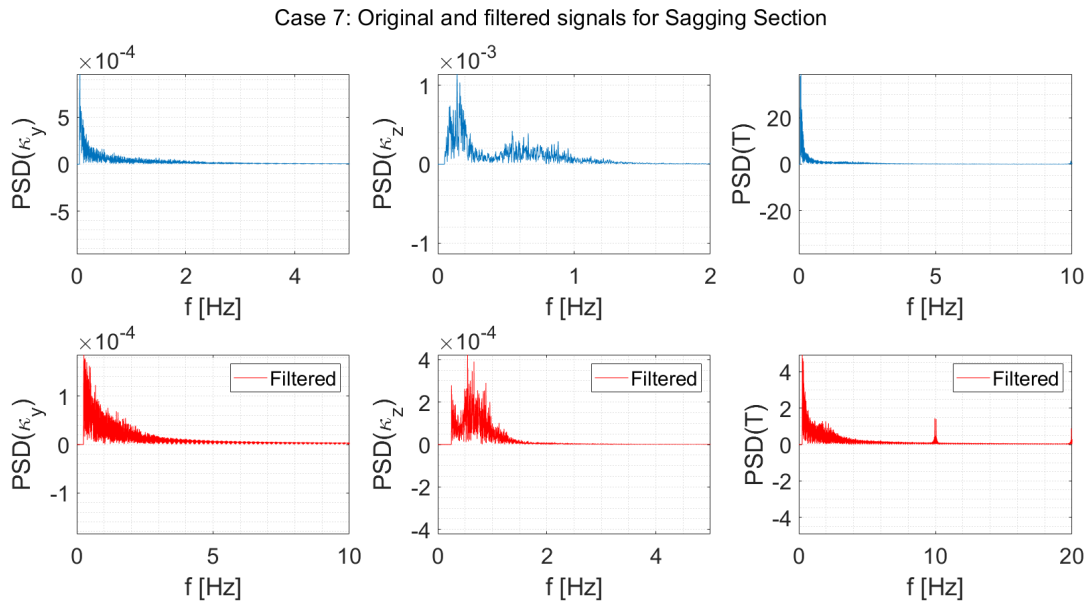


Figure B.0.2: Global Analysis Results in the Frequency Domain for Case 7 Sagging Section

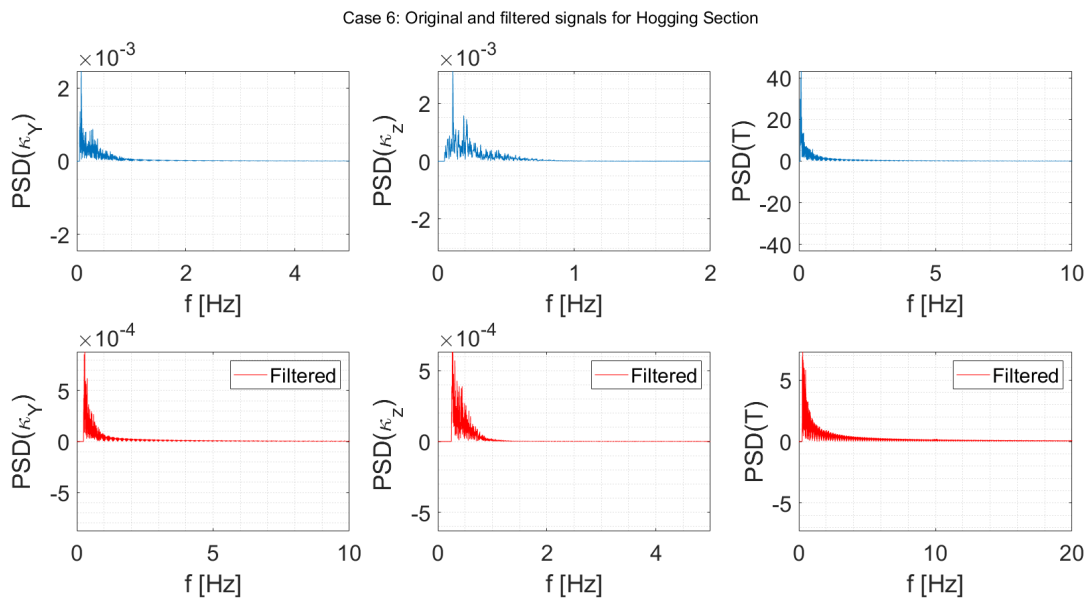


Figure B.0.3: Global Analysis Results in the Frequency Domain for Case 6 Hogging Section

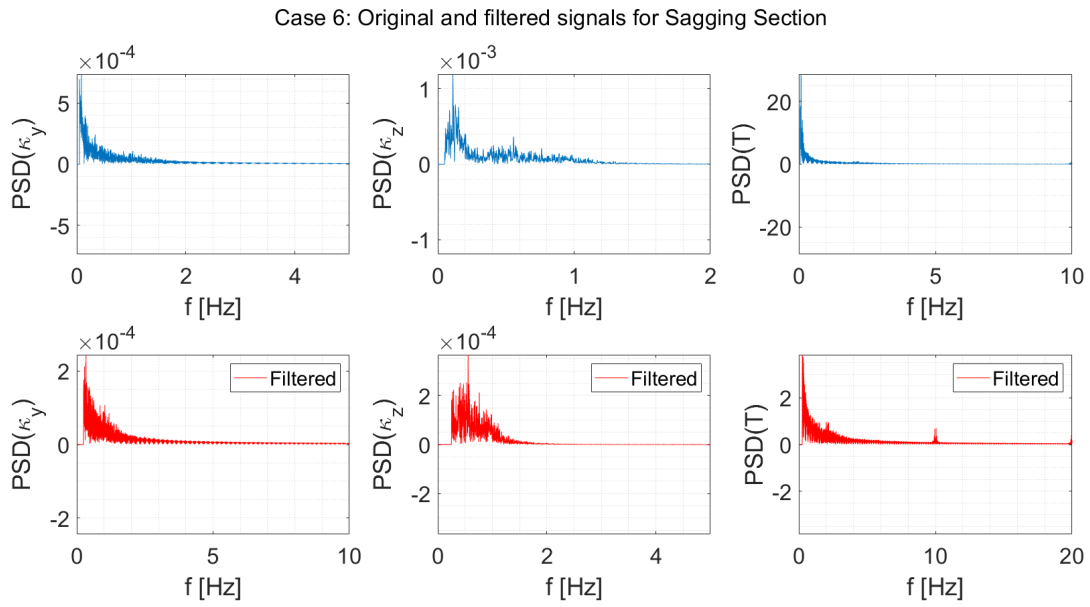


Figure B.0.4: Global Analysis Results in the Frequency Domain for Case 6 Sagging Section

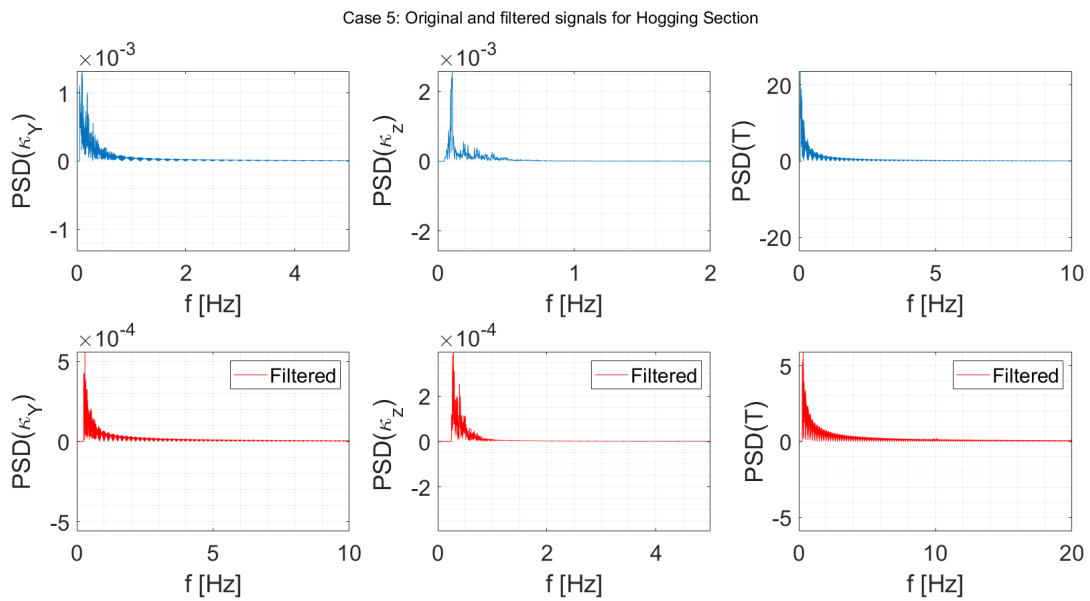


Figure B.0.5: Global Analysis Results in the Frequency Domain for Case 5 Hogging Section

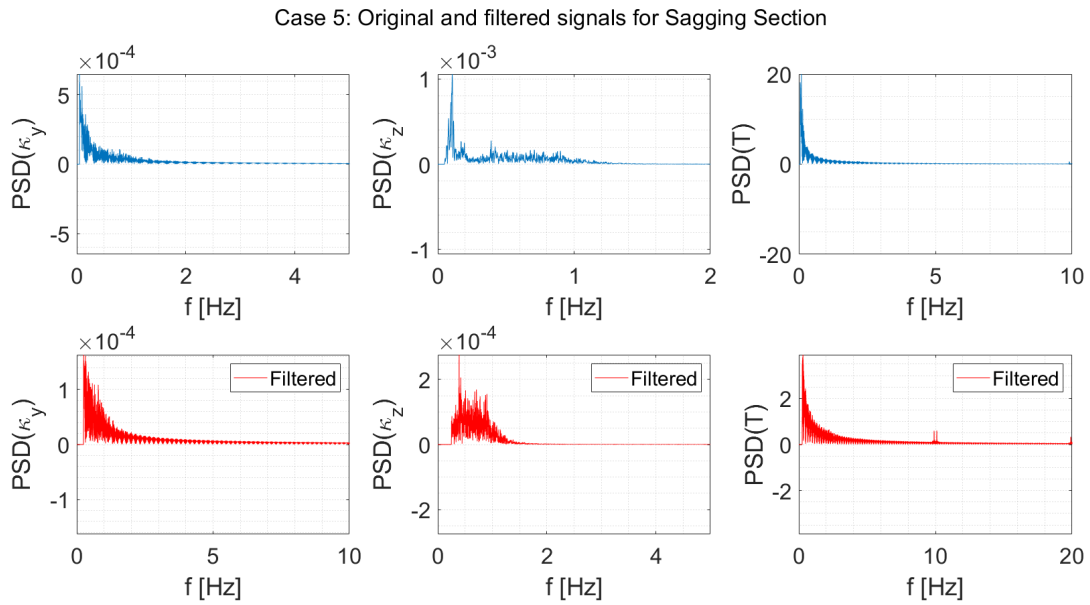


Figure B.0.6: Global Analysis Results in the Frequency Domain for Case 5 Sagging Section

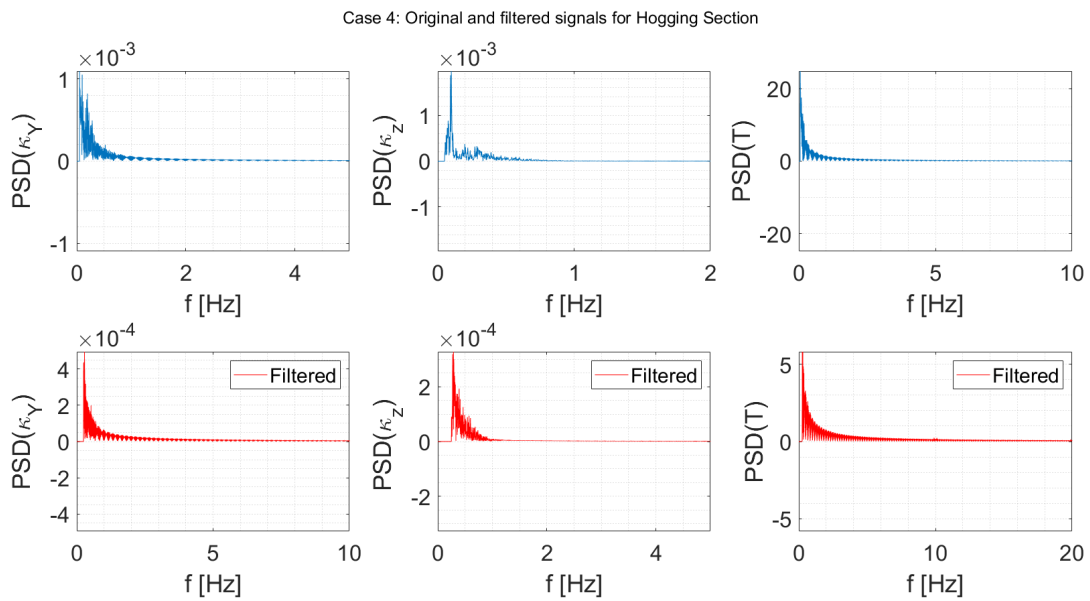


Figure B.0.7: Global Analysis Results in the Frequency Domain for Case 4 Hogging Section

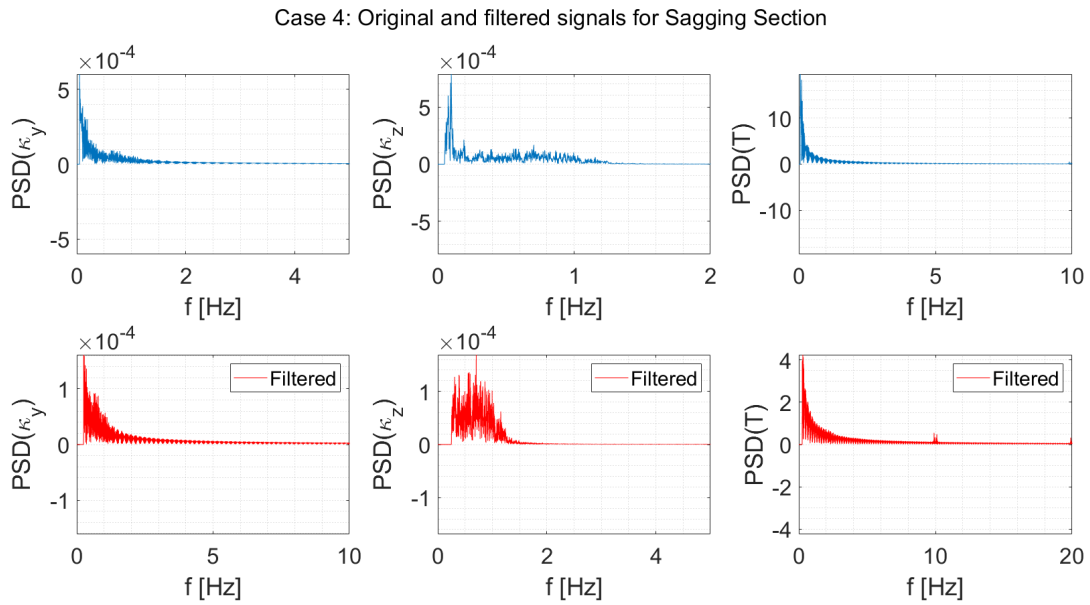


Figure B.0.8: Global Analysis Results in the Frequency Domain for Case 4 Sagging Section

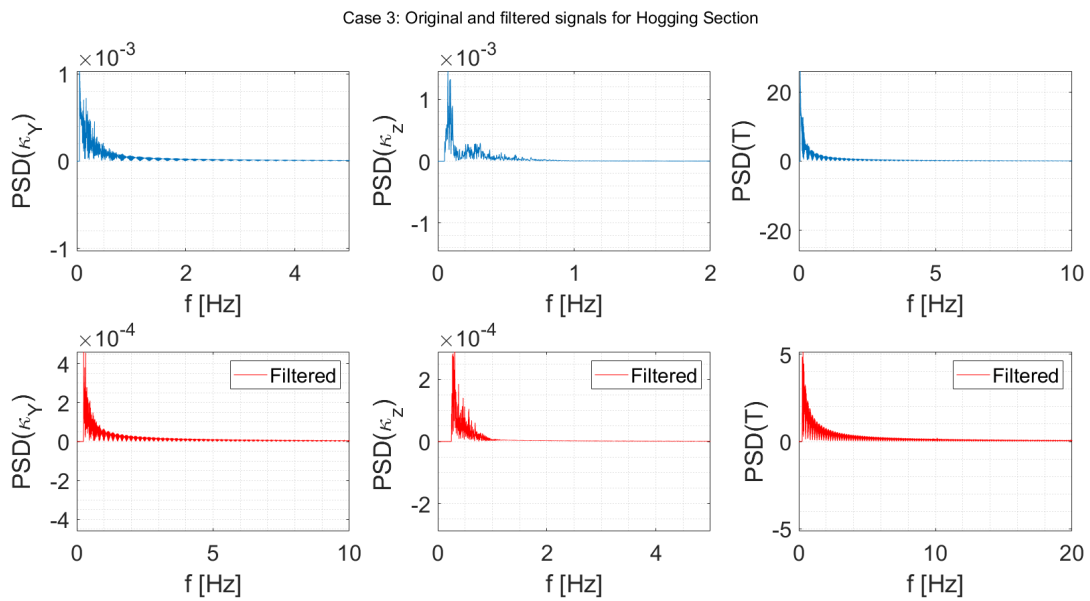


Figure B.0.9: Global Analysis Results in the Frequency Domain for Case 3 Hogging Section

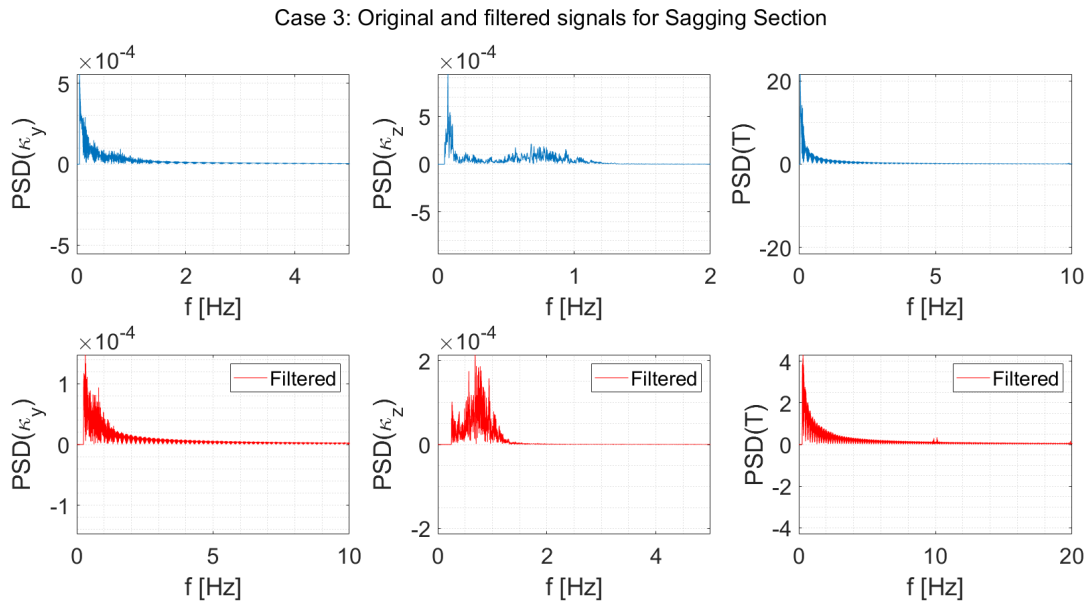


Figure B.0.10: Global Analysis Results in the Frequency Domain for Case 3 Sagging Section

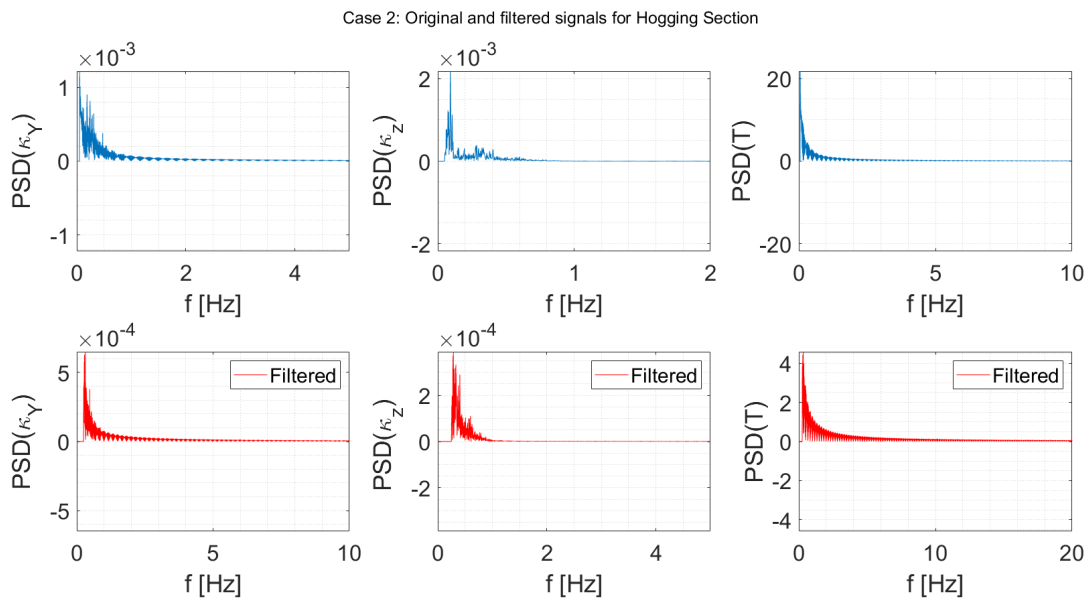


Figure B.0.11: Global Analysis Results in the Frequency Domain for Case 2 Hogging Section

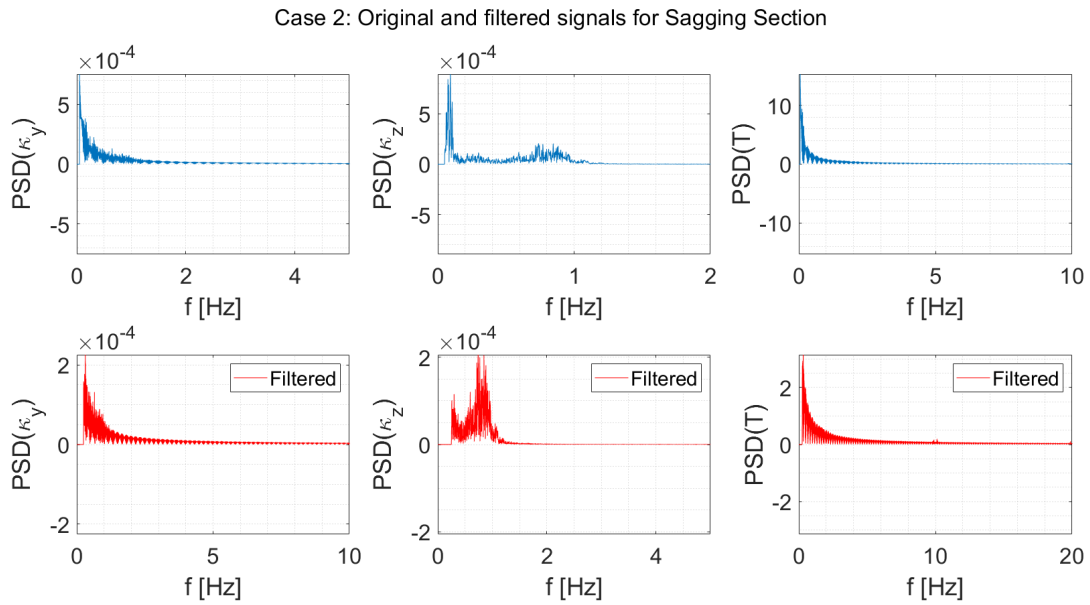


Figure B.0.12: Global Analysis Results in the Frequency Domain for Case 2 Sagging Section

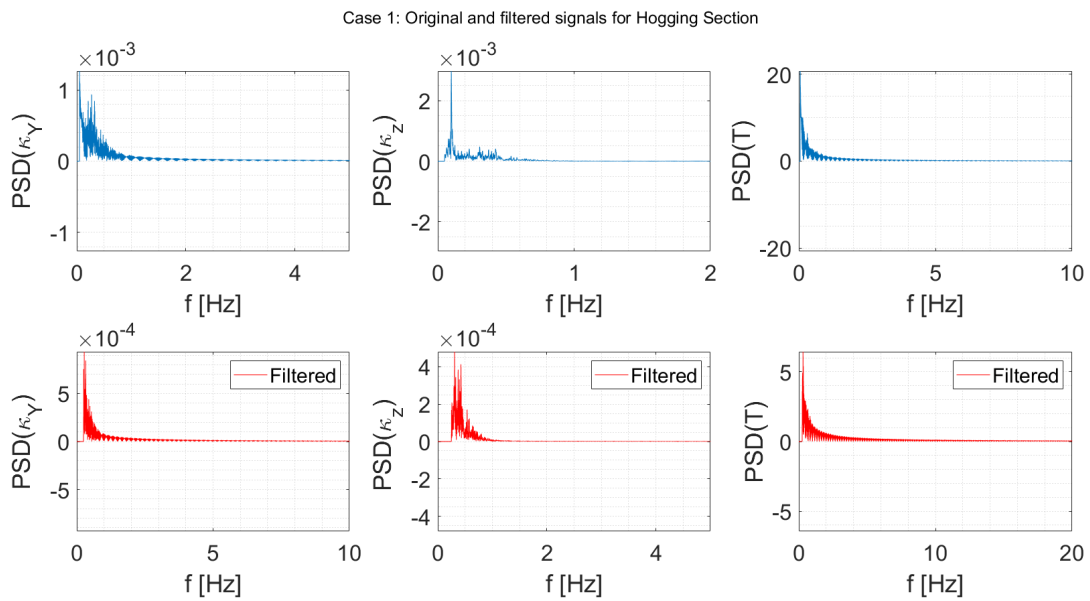


Figure B.0.13: Global Analysis Results in the Frequency Domain for Case 1 Hogging Section

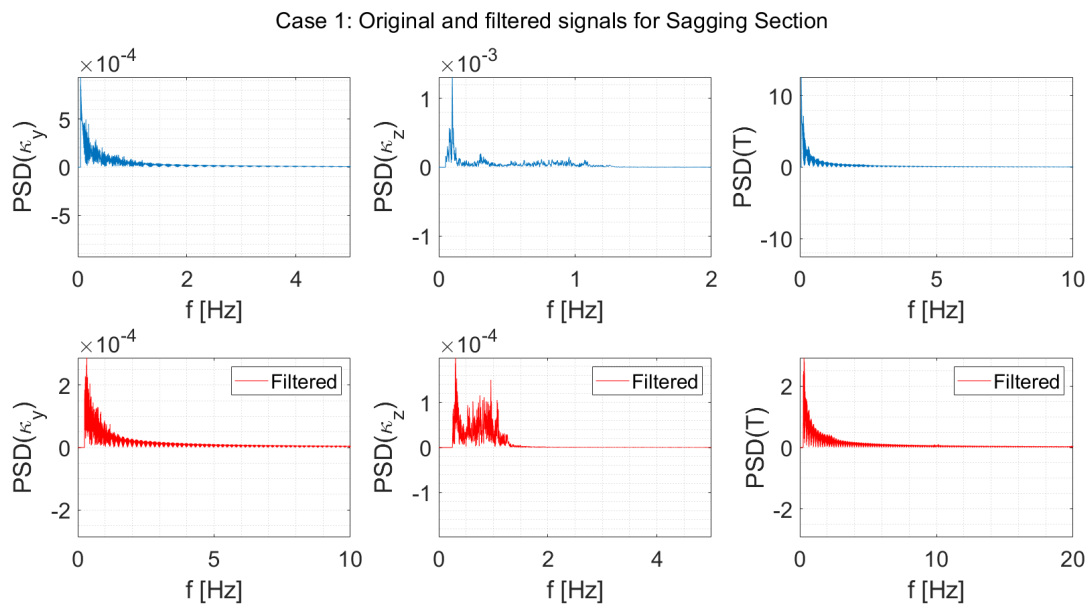


Figure B.0.14: Global Analysis Results in the Frequency Domain for Case 1 Sagging Section

